BIOINSPIRED HYDRAULIC MCKIBBEN ACTUATION FOR EFFICIENT ROBOTIC MOTION: ENERGETICS, VARIABLE RECRUITMENT, AND CONTROL

A Dissertation

Presented to the Faculty of the Graduate School

of Cornell University

in Partial Fulfillment of the Requirements for the Degree of

Doctor of Philosophy

by

Michael Adam Meller

January 2017

BIOINSPIRED HYDRAULIC MCKIBBEN ACTUATION FOR EFFICIENT ROBOTIC MOTION: ENERGETICS, VARIABLE RECRUITMENT, AND CONTROL

Michael Adam Meller, Ph.D.

Cornell University 2017

Hydraulic cylinder-driven control systems have become increasingly popular as the means of actuation for human-scale legged robots (such as Boston Dynamics' ATLAS humanoid) and assistive devices (such as Lockheed Martin's HULC exoskeleton) largely due to their high actuator power density. McKibben muscles are also an attractive actuator choice among the robotics community because of their extremely light weight, high force capacity, and low fabrication cost. The vast majority of these actuators are operated pneumatically, enhancing compliance, but resulting in extremely low efficiencies. Powering these actuators hydraulically increases actuator stiffness and allows for roughly double the efficiency. While running the system hydraulically is more efficient than pneumatic operation, efficiency is still one of the largest drawbacks of hydraulic servo-systems, where on average 43% of the input power is lost to valve throttling. Due to these large losses, one of the biggest limitations of these robots is their run time untethered from a power source.

This dissertation aims to improve actuation efficiency in order to enable a greater range for mobile robots. First, the transduction efficiency of McKibben muscle actuators is characterized, and is increased through the use of higher bulk modulus fluids, inelastic bladders, and higher pressures. Through these modifications, the transduction efficiency is increased from 27% for a pneumatic

latex bladder McKibben muscle, to 80% for a hydraulic low density polyethylene bladder McKibben muscle. Next, a real-time variable recruitment actuation scheme is implemented on a bundle of parallel McKibben actuators for the purpose of reducing servovalve throttling losses. This strategy minimizes fluid power consumption by selectively activating the minimum number of McKibben actuators required by the load, and is inspired by multiple motor unit summation in skeletal muscle. Over the range of loads tested on the proof-of-concept bundle, variable recruitment is shown to increase actuation efficiency from 39% to 57% compared to a throttling only approach. Lastly, an improved angular position controller for the hydraulic McKibben actuators is formulated via a cascaded PI(angular feedback)-P(pressure feedback)-controller with feedforward compensation. The feedforward term provides anticipative action through a McKibben flowrate model and valve flow gain. This controller increases system bandwidth and reduces settling times. These control techniques are then discussed within the context of enhanced variable recruitment control, and overall future directions for improving system efficiency are considered.

BIOGRAPHICAL SKETCH

Michael Meller began his graduate studies at Cornell University in 2010, where he majored in Mechanical Engineering, in the concentration of Dynamics and Control. He joined the Laboratory for Intelligent Machine Systems (LIMS), under the direction of the late Professor Ephrahim Garcia – before his untimely passing in 2014. During his graduate studies, Michael was a Laboratory Teaching Assistant for Dynamics, Mechatronics, and Feedback Control Systems. While he was the Head Lab Teaching Assistant for Mechatronics in 2012, Michael was awarded the Sibley Prize for Excellence in Graduate Teaching Assistance. Michael also actively participated in outreach to stimulate interest in STEM among middle and high school students; he has helped co-lead workshops about rocketry in 4H and robotics in EYH.

In 2014, Michael was awarded a Master's of Science degree for his work on hydraulic McKibben artificial muscle actuators. He continued his research on hydraulic McKibben muscles in pursuit of his doctorate, but in a variable recruitment, parallel arrangement for improving actuation efficiency. In June of 2015 he led the trip to Pomona, CA for the DARPA Robotics Challenge, where the LIMS lab demonstrated their artificial muscles on a robotic arm. Michael has published (as a first author) one paper in the *Journal of Intelligent Material Systems and Structures (JIMSS)*, one paper in *Bioinspiration and Biomimetics*, and has one paper in review for *Sensors and Actuators: A Physical*. Additionally, he has several co-authored papers published in *JIMSS* as well as in the *Smart Materials and Structures Journal*.

For Ephrahim.

ACKNOWLEDGEMENTS

I am forever grateful to my advisor, Prof. Ephrahim Garcia, who was taken from us far too soon. My memories of his curiosity, compassion, and grit are a constant source of inspiration for me. I greatly appreciate the advice, insight, and help of my special committee, Prof. Mark Campbell, Prof. Amit Lal, Prof. Rob Shepherd, and Prof. Matthew Bryant.

I would like to thank my parents, Pat and Mitch, and my sister, Julia, for always pushing me to strive for better, get the most out of life, and for always being there for me. I am grateful for the warmth and support from all of my friends and family along the way. I am thankful for my oncologists, and the research and nursing staff at the Wilmot Cancer Center for restoring my health.

I am extremely grateful to the MAE department, specifically Prof. Mark Campbell, Dr. Marcia Sawyer, and Prof. Brian Kirby for their kindness, generosity, and help during my time at Cornell – especially when Prof. Garcia passed away, throughout my lymphoma treatment, and amidst building renovations.

I thank my LIMS lab mates: Prof. Matthew Bryant, Dr. Rashi Tiwari, Mitchell Walters, Dr. Alexander Schlichting, and Dr. Juan Gomez for welcoming me into into the lab and for their advice; Boris Kogan, Alexander Volkov, Jordan Chipka, Joval Mathew, Julian Whitman, and more for helping bring our research to life; and Dr. Malika Grayson, Dr. Erick Ball, Sean Mitchell, and Liz Hasseler for their moral support.

I am grateful for David Hartino and Liran Gazit's wisdom and efforts setting up labs that I TAed. I thank Leon Stoll for his perspective and helping with many lab purchases, and Matt Steel for assisting with our wild laboratory needs.

Lastly, I gratefully acknowledge funding support for my graduate studies from Cornell University, Moog Inc., and the DARPA M3 program.

TABLE OF CONTENTS

LIST OF TABLES

LIST OF FIGURES

LIST OF ABBREVIATIONS

Abbreviation		Definition
EHSV	=	Electrohydraulic servovalve
FAM	=	Fluidic artificial muscle
FF	=	Feedforward
HAM	=	Hydraulic artificial muscle
LDPE	=	Low-density polyethylene
MU	=	Motor unit
PAM	=	Pneumatic artificial muscle
PI	=	Proportional-integral control
PI-P	=	Cascaded proportional-integral, proportional-control
RL	=	Recruitment level

LIST OF SYMBOLS

Symbol		Definition
$a; b$	=	Geometric constants of McKibben muscle initial mesh state
c_v	=	Valve orifice coefficient
E	=	Fluid energy input to McKibben muscle (before or after valve)
Eff	=	McKibben model effectiveness term (function of pressure)
F	=	Tension produced by McKibben muscle
i	=	Current recruitment level of muscle bundle
K_{q0}	=	Flow gain of servovalve
l	=	Length of McKibben muscle
n	=	Total number of recruitment levels in muscle bundle
P	=	Pressure (inside McKibben muscle or elsewhere in system)
Q	=	Volumetric flowrate
R	=	Distance between attachment point of actuators and joint
r	=	Radius of McKibben muscle
$t; t_0; t_f$	=	Instantaneous, initial, and final time respectively
u_v	=	Commanded valve voltage
V	=	Volume of McKibben muscle
ΔV	=	Volume of fluid delivered to McKibben muscle
$W_{mech,out}$	=	Mechanical work output of McKibben muscle
x	=	Stroke of McKibben muscle
α	=	Braid angle of McKibben muscle mesh w.r.t. longitudinal axis
ε	=	Strain of McKibben muscle
$\Delta\varepsilon$	=	Change in strain of McKibben muscle
η	=	Efficiency
θ	=	Robot arm angle w.r.t. horizontal
$\dot{\theta}$	=	Robot arm angular velocity
$\kappa; \kappa_F; \kappa_\varepsilon$	=	Tondu, force, and strain model tuning parameters respectively

Subscripts:

Symbol		Definition
$(\cdot), avg, tot$	=	Average total
$(\cdot), lin$	=	Linearized
$(\cdot), max, i$	=	Maximum of a specific recruitment level
$(\cdot), min, i$	=	Minimum of a specific recruitment level
0	=	Initial geometry of McKibben muscle (at longest length)
A	=	State of McKibben: unpressurized, longest length
atm	=	Atmospheric
B	=	State of McKibben: blocking force
C	=	State of McKibben: free strain
d	=	Desired
FAM	=	Transduction of FAM
FAM, mod	=	Modified model
$fluid, in$	=	Fluid energy input downstream of valve
$fluid, in, S$	=	Fluid energy input upstream of valve (from pump)
m	=	McKibben muscles
max	=	Maximum
$meas$	=	Measured value
$meas, max$	=	Maximum measured value
mod	=	Modified model
op	=	Operating
P	=	Pressurized fluid required to remove slack from mesh
PI;PI,FF;PI-P,FF	=	See list of abbreviations
$pneu$	=	Compressed state of air
$pneu, i$	=	Initial expanded state of air
$real$	=	Real measured output
ref	=	Reference
RL	=	Recruitment level
RL, i	=	Current recruitment level
S	=	Supply (pump)
T	=	Tank (return reservoir)
$theor$	=	Theoretical (ideal model)
v	=	Valve

INTRODUCTION

This dissertation presents research on increasing the efficiency of McKibben artificial muscle actuators, as well as an approach to hydraulically controlling them. This is of interest because the energetics of these actuators has rarely been considered, even though their ability to efficiently produce motion significantly impacts the endurance of the untethered robots in which they are often utilized. Chapter 1 experimentally quantifies the transduction efficiency of traditional pneumatic McKibben muscles as well as our developed hydraulic, inelastic bladder artificial muscles. Chapter 2 further improves the actuation efficiency of hydraulic McKibben muscles by reducing servovalve throttling losses through the implementation of parallel McKibben muscles with a real-time variable recruitment methodology. Chapter 3 betters the angular position controller tracking abilities through the anticipative action of a developed feedforward term and a nested pressure feedback loop.

Despite extensive modeling and characterization efforts, little is known about the energetics of McKibben muscle actuators. Chapter 1, published in the *Journal of Intelligent Material Systems and Structures*, experimentally investigates the effectiveness of traditional McKibben muscles at converting fluid energy delivered to the actuator to mechanical output work over full actuation cycles. Once these efficiency metrics are established, a comparison of the efficiencies of traditional pneumatic fluidic artificial muscles (FAMs) and hydraulic FAMs is presented. Two new hydraulic oil compatible bladder materials are tested – an elastomeric Viton bladder, and an inelastic low-density polyethylene (LDPE) bladder. The performance of these muscle variants is compared by measuring blocked force and free contraction as a function of pressure, hysteresis, and en-

ergy efficiency. The measurement of fluid volume delivered to the FAMs over their actuation ranges is shown to be useful for evaluating the accuracy of existing cylindrical volume models. Models of the energy conversion efficiency are developed and compared to the experimental data. The results show that using an inelastic bladder significantly improves the efficiency, force capacity, and contraction range of McKibben muscles, however, it also increases the actuator's hysteretic behavior. Powering the muscles hydraulically and operating at higher pressures improves the efficiency as well.

Hydraulic control systems have become increasingly popular as the means of actuation for human-scale legged robots and assistive devices. One of the biggest limitations to these systems is their run time untethered from a power source. One way to increase endurance is by improving actuation efficiency. Chapter 2, published in *Bioinspiration and Biomimetics*, investigates reducing servovalve throttling losses by using a selective recruitment artificial muscle bundle comprised of three motor units. Each motor unit is made up of a pair of hydraulic McKibben muscles connected to one servovalve. The pressure and recruitment state of the artificial muscle bundle can be adjusted to match the load in an efficient manner, much like the firing rate and total number of recruited motor units is adjusted in skeletal muscle. A volume-based effective initial braid angle is used in the model of each recruitment level. This semi-empirical model is utilized to predict the efficiency gains of the proposed variable recruitment actuation scheme versus a throttling-only approach. A real-time orderly recruitment controller with pressure-based thresholds is developed. This controller is used to experimentally validate the model-predicted efficiency gains of recruitment on a robot arm. The results show that utilizing variable recruitment allows for much higher efficiencies over a broader operating envelope.

McKibben artificial muscle actuators are predominantly controlled pneumatically. Recently, hydraulic operation has gained interest due to its higher rigidity and efficiency. While there has been extensive control system development for pneumatic artificial muscles, little has been conducted hydraulically. Chapter 3, in review for publication in *Sensors and Actuators A: Physical*, investigates three different controllers developed for a loaded robotic arm actuated with hydraulic McKibben muscles. The goal was to achieve good angular position tracking over a range of frequencies up to 1 Hz. The first scheme, serving as the baseline, is a proportional-integral controller. The second architecture adds a model-based feedforward term including the expected flowrate demands and valve flow gain to the baseline. The last scheme adds an inner pressure feedback loop to the second architecture. All controllers were evaluated with frequency and step response experiments. The results show that a simple proportional-integral controller has significant phase lag and severe attenuation at the higher frequencies tested; adding the feedforward term almost completely eliminates these. The cascaded loop helps improve rise and settling times.

CHAPTER 1

RECONSIDERING THE MCKIBBEN MUSCLE: ENERGETICS, OPERATING FLUID, AND BLADDER MATERIAL

1.1 Introduction

McKibben muscles are an attractive choice of actuation for a number of reasons. Some of these include their light weight, high force capability, low static friction, and compliance. In addition, precise alignment is not a requirement like it is for a fluidic cylinder [78]. Their light weight is due to their construction, which typically contains a helically braided sheath that encapsulates an inner elastomeric bladder. These active parts are energized via a fluid port that is fixed on one end of the actuator. The other end of the actuator is usually a fluid plug, and both ends require the ability to attach mechanically to other structures, like tendons attach muscles to bones. These components are typically held together by tube clamps and barbed hose fittings. Some groups have employed adhesives like epoxy [91] and custom swaging processes [90] to fortify the fitting tensile and sealing properties. These actuators have been proposed for many different applications ranging from humanoid robots [79, 85] to aerospace systems [57, 91]. For actuation of mobile applications such as these, efficiency is an important concern. However, there is almost no information on the energetic efficiencies of these actuators. Hence, this chapter begins by experimentally characterizing how effective a McKibben muscle is at converting the input fluid energy delivered to mechanical output work. To more fully characterize this transduction efficiency, these tests are performed over a range of operating pressures, and observed over the stroke of the actuators as well.

Nearly all fluidic artificial muscles (FAMs) are operated pneumatically, with only a small number of other research groups actuating them hydraulically [27, 51, 73, 77]. Pneumatic actuation offers the convenience of venting exhaust air directly to the atmosphere, and maximizes the soft compliance of the muscles which is valuable when human-robot interaction is involved [81]. Using compressed air as the fluid medium has disadvantages as well; valve-controlled pneumatic systems are rarely over 30% efficient [9], and have slower response time and reduced positional control authority when compared to hydraulics [27]. Maximum efficiencies for valve-controlled hydraulic systems have been cited as approximately 60% [9]. These higher efficiencies, quicker response, and better position control are due to hydraulic fluid's much higher bulk modulus. For these reasons, the energetics of hydraulic artificial muscles (HAMs) are studied and compared to the traditional pneumatic actuation of McKibben muscles.

Before hydraulic artificial muscles can be realized, the muscle construction must be revised. The natural rubber that is used in traditional McKibben construction deteriorates when exposed to hydraulic oil, so a brief study on two different hydraulic fluid compatible bladder materials has been conducted. The first hydraulic fluid compatible material tested was Viton, a fluoroelastomer known for its durability and chemical resistance in harsh environments [23]. The second synthetic hydraulic oil compatible material tested was low density polyethylene (LDPE). This bladder is unique in that it is inelastic. One study has reported using rubber-less artificial muscles, and it utilized an aluminum vapor deposition polyester sheet for the bladder [64]. The efficiency metrics defined in this chapter, in addition to the blocked force, free strain, and hysteresis are used to compare the effectiveness of each bladder material.

It is also desirable to model the characteristics of the actuators to predict the force output and efficiencies beyond the ranges tested. To ensure an accurate model, the volume of fluid delivered to the muscles was measured. Without this information, it is difficult to assess the validity of the constant cylindrical shape many assume in their models [15, 80], and whether including conically shaped or circular-arced end segments is necessary [31, 37, 81]. After this is discussed, a semi-empirical model is developed, and this is used to ultimately model the efficiency of the actuators. This is compared to the experimental data.

1.2 Energetics of McKibben Muscles

It is important to consider the transduction efficiency of actuators, and how to implement them as effectively as possible. While this is the case, few have considered this idea of energy conversion and efficiency regarding artificial muscles. Chou and Hannaford investigate the efficiency of a rubber bladder PAM in a quasi-stationary, constant pressure, maximal shortening theoretical experiment, where their simulation at 5 bar resulted in an efficiency of 29% [15]. Experimental data on this energy conversion for fluidic artificial muscles was conducted at a single operating pressure of 3.4 bar for hydraulic and pneumatic operation by Meller, Bryant, and Garcia [46]. The resulting efficiencies were 19.1% for pneumatic operation, and 53.3% for hydraulic operation. In this chapter, we conduct these experiments over a range of pressures and over the stroke of the actuator. These methods were also developed as metrics for comparing different bladder materials.

1.2.1 Experimental Procedure and Test Apparatus

In order to obtain the efficiencies of the actuators, the net mechanical output work and net fluid input energy are monitored. To do this, the tension produced over the full stroke of the actuator is observed, as is the pressure and volume of fluid delivered to the muscle. The experimental apparatus used to conduct these efficiency tests consisted of mechanical and fluidic sections. An Instron 5566 tensile testing machine was utilized for producing the mechanical motion and measuring the position and force output of the actuators. A compressor, pressure regulator, valve, and accumulator comprised the fluid circuit that produced and controlled the fluid power for the actuator. Fluid energy measurements were performed using a pressure transducer and a pressurizable graduated cylinder for measuring volume. A picture of the Instron machine with a muscle attached is presented in Figure 1.1 (a), and all of the components that make up the test apparatus are diagrammed in Figure 1.1 (b). It is noted that all the efficiency experiments were run hydraulically to track the movement of this water-air interface. Water filled the entire actuator being tested, and the air-water interface remained within the volume of the graduated cylinder. It is assumed that the water compression is negligible due to its high bulk modulus, which is reasonable since it only compresses 0.18% of the total volume when operated at the highest test pressure. Therefore, the measured volume changes are assumed to be purely a result of the muscle's geometry, and the efficiency values reported below are solely the muscle's energy conversion abilities.

The experimental procedure for the quasi-static efficiency characterization begins by fixing the unpressurized actuator at its maximum length in the Instron machine. This corresponds to point A in Figure 1.2. Then, the pressure is slowly

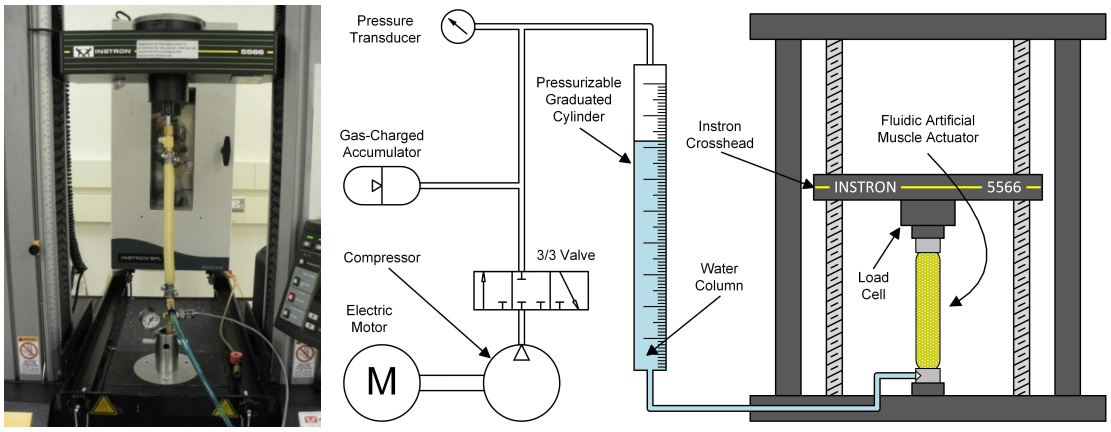

Figure 1.1: (a) Picture of a FAM mounted in the Instron 5566, and (b) a diagram of the full experimental apparatus used for testing.

increased to the full operating pressure for the test. The force generated when full pressure is reached represents the blocked force condition of the actuator, and is seen as point B in Figure 1.2. The operating pressure for the singular case depicted in Figure 1.2 is 4.1 bar. While maintaining this pressure, an isobaric contraction of the actuator is allowed by the Instron machine until the muscle is no longer producing tension. This is known as the free contraction state, and is labeled as point C in Figure 1.2. It is noted that the volume the muscle swells from points A to B in Figure 1.2 (b), and this volume change is not taken into account in current volume models of these actuators, which is discussed more in depth in later sections. The additional fluid volume that is delivered at constant pressure as the muscle shortens from point B to C is a result of the muscle bulging radially due to the pantograph geometry of the mesh.

Curve B to C in Figure 1.2 (a) is the contraction portion of the hysteretic tension-strain plots that are commonly reported in the literature for these actuators. The mechanical output work is calculated from the data in Figure 1.2 (a) as:

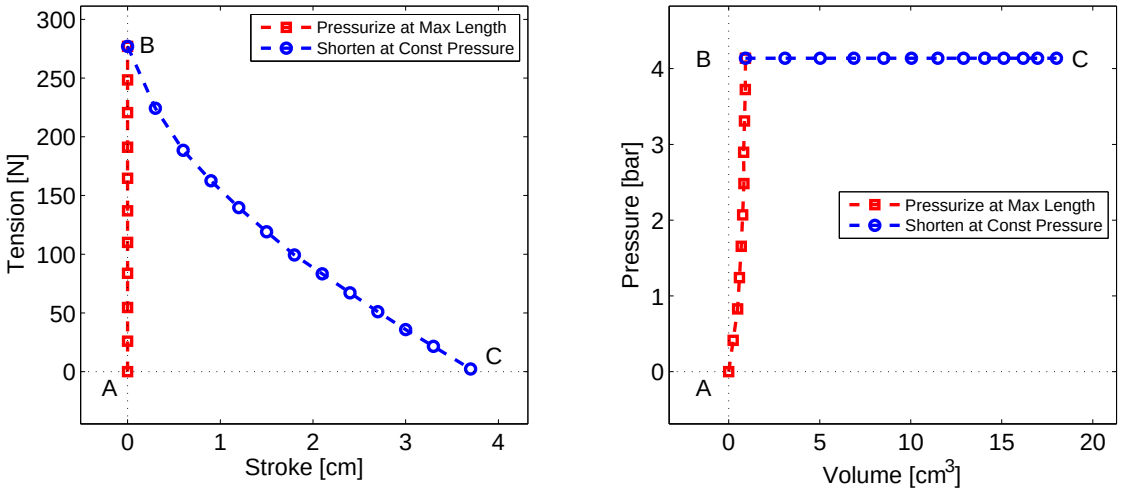

Figure 1.2: (a) Tension-stroke plot that yields mechanical output work; and (b) pressure-volume plot that yields fluid input energy for a traditional latex bladder FAM operating at 4.1 bar.

$$W_{mech,out} = \int_{x_B}^{x_C} F(P,x)dx = l_0 \int_{\varepsilon_B}^{\varepsilon_C} F(P,\varepsilon)d\varepsilon, \tag{1.1}$$

where F is the tension produced by the muscle, P is the operating pressure, l_0 is the muscle's initial length, l is the current length of the muscle, ε is the strain of the muscle, x is the stroke of the muscle: $x = l_0 - l = l_0\varepsilon$, and the subscripts B and C correspond to the labeled points in Figure 1.2 (a).

Figure 1.2 (b) is a plot of the pressure and volume of fluid provided to the muscle over this same actuation cycle. Integrating beneath this curve yields the fluid energy delivered to the muscle throughout the cycle:

$$E_{fluid,in} = \int_{V_A}^{V_B} PdV + P_{max} \int_{V_B}^{V_C} dV, \tag{1.2}$$

where P is the pressure, V is the volume of fluid delivered to the muscle, and the subscript max denotes the operating pressure of the isobaric contraction from B to C in Figure 1.2. The efficiency of the energy conversion is defined in Equation (1.3) as the ratio of the mechanical output work defined in Equation (1.1) to the fluid input energy presented in Equation (1.2):

$$\eta_{FAM} = \frac{W_{mech,out}}{E_{fluid,in}}. \tag{1.3}$$

This procedure is repeated to determine the energetic efficiency of the actuators for various conditions in the following sections.

1.2.2 Experimental Characterization of Efficiency

Using the method described above, the efficiency of a 17.3 cm long muscle with a latex bladder and Kevlar sheath was measured over a range of pressures from approximately 1-5 bar (15-75 psi) in 1 bar (15 psi) increments. The Kevlar mesh has an expansion range of 1.27- 2.22 cm, and the latex bladder used was 0.953 cm in inner diameter (ID) and 1.27 cm in outer diameter (OD), with a hardness of 35 shore A. The plots in Figure 1.3 (a) to (c) display the results as a function of pressure. Figure 1.3 (a) plots the mechanical output work of the muscle, and behind each data point exists an entire tension-stroke plot at that operating pressure, as seen in Figure 1.2 (a). As expected, the mechanical output work increases with increasing pressure. There appears to be nonlinear effects that are amplified at lower pressures which are likely due to the elastic energy storage in the bladder of the FAM; at lower pressures, the bladder hasn't fully inflated

yet. Figure 1.3 (b) displays the fluid input energy for the muscle with increasing pressure. It grows almost linearly as a function of pressure over the full pressure range tested. Each data point in this graph was generated from the integral of a pressure-volume curve at each pressure as was presented in Figure 1.2 (b). The trend seen for the efficiency as a function of pressure in Figure 1.3 (c) shows that efficiency initially increases with pressure, and then begins to plateau. This is consistent with our expectations since the fluid energy input increases linearly with pressure, but the mechanical work output lags initially at lower pressures before reaching its linearly increasing range, presumably due to the energy required to expand the elastomeric bladder into its active range.

It was also desired to determine if there was an optimal stroke range for the muscle in terms of most efficient conversion of fluid energy to mechanical work. This was the inspiration for Figure 1.3 (d) to (h) plotted as a function of stroke. The three most spread pressure ranges were chosen to display in the graphs. Figure 1.3 (d) is the contraction portion of the hysteretic tension-stroke plot, and it shows typical behavior of FAMs, with the force being a nonlinear function of both pressure and contraction state. Figure 1.3 (e) graphs the volume as a function of stroke. Some interesting things to note are that while the total fluid volume delivered does depend on pressure, the curve it follows as a function of contraction does not change; for higher pressures, it just travels further along this volume-contraction trend because the free stroke of the actuator increases with pressure. This will be discussed further in a later section. Figure 1.3 (f) to (h) plots the mechanical output work, fluid input energy, and efficiency as a function of contraction respectively. The efficiency of the actuator begins at zero due to the small amount of fluid energy required to bring the actuator up to operating pressure while zero mechanical output work is performed. This

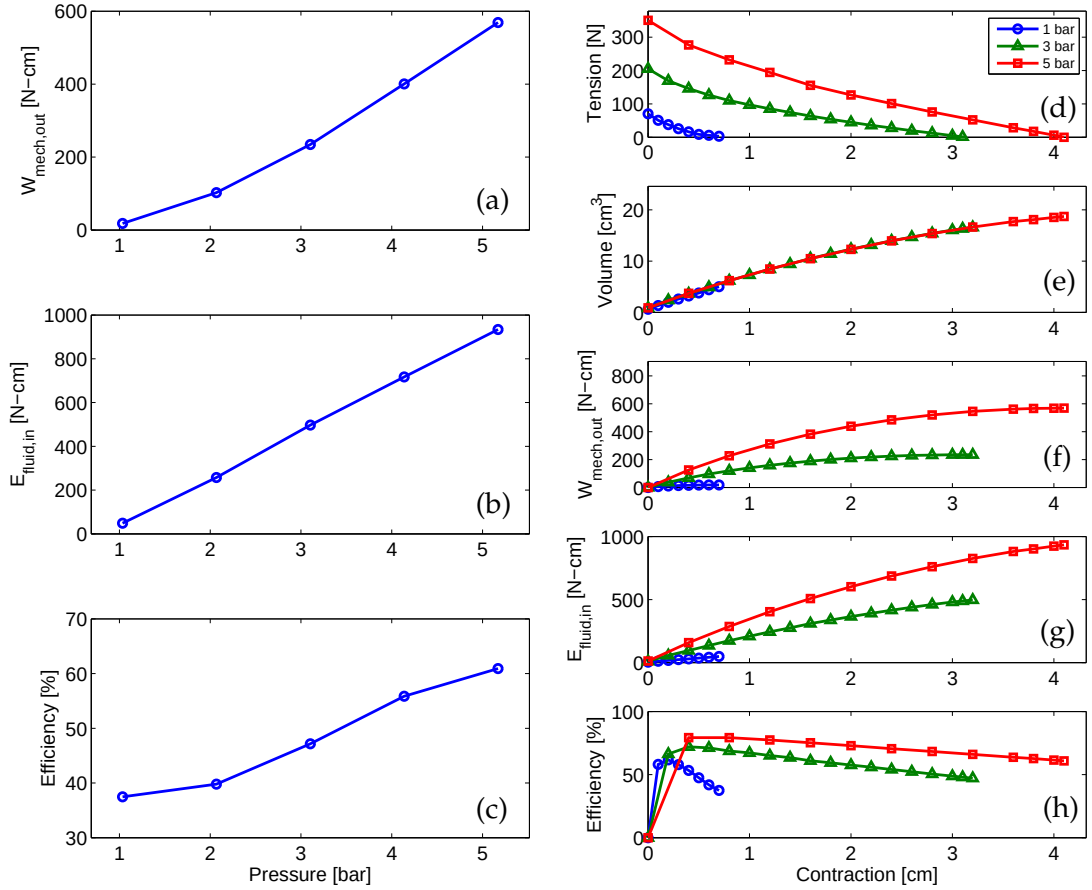

Figure 1.3: (a) Mechanical output work, (b) fluid input energy, (c) and efficiency of the latex muscle all as a function of pressure. (d) Tension, (e) volume, (f) mechanical output work, (g) fluid input energy, (h) and efficiency of the latex muscle all as a function of contraction.

was observed previously in Figure 1.2 when going from point A to point B. The highest efficiency values occur in the smaller stroke, higher force ranges as observed in Figure 1.3 (h). This is likely due to a few phenomena; the amount of work required to overcome friction increases approximately proportionally to the stroke, and more energy is required to expand the elastomeric bladder as the muscle approaches the free contraction state where the largest radial expansion

occurs.

1.3 Operating Fluid Effects on Efficiency

1.3.1 Procedure

As stated previously, all of the efficiency measurements were conducted hydraulically only. The results of these tests are assumed to represent the exact amount of energy conversion the muscle performs because the water is assumed to be incompressible. To determine the total volume necessary for the pneumatic case, the amount the air needs to be compressed to bring the system to full pressure is added to the changing volume of the actuator. We assume because we are considering quasi-static cases, the compression of the gas is slow enough to allow the system to maintain constant temperature. This allows us to employ Boyle's law for the isothermal compression process of an ideal gas:

$$P \propto \frac{1}{V}. \tag{1.4}$$

Using Equation (1.4) we can define the initial volume of air to be the same experimentally determined volume at the free stroke of the muscle at maximum pressure *after* it is expanded to atmospheric pressure:

$$V_{pneu,i} = \left(\frac{P_{max}}{P_{atm}} + 1\right) V_C, \tag{1.5}$$

where P_{max} is the max operating gauge pressure for the case being considered, P_{atm} is atmospheric pressure, and V_C is the free stroke muscle volume for the hydraulic case for the operating pressure at hand. This initial volume of air corresponds to the minimum quantity of air that is required to bring the muscle to its fully contracted state at full operating pressure. The current volume of this quantity of air is defined as:

$$V_{pneu} = \left(\frac{P_{max} + P_{atm}}{P + P_{atm}} \right) V_C, \tag{1.6}$$

where P is the current pressure. Using Equations (1.5) and (1.6), the pneumatic volume delivered to the muscle can be formulated:

$$\Delta V_{pneu} = V_{pneu,i} - V_{pneu} + V_C. \tag{1.7}$$

1.3.2 Results

Figure 1.4 (a) is identical to Figure 1.2 (a) since the same mechanical output work is being performed and compared for hydraulic and pneumatic operation. Figure 1.4 (b) shows the same hydraulic input energy as before as well, but also includes the amount of pneumatic input energy required to produce the same mechanical output at the same operating pressure of 4.1 bar. It is clear that integration of the pneumatic pressure-volume curve yields a much larger input energy than the hydraulic case.

Figure 1.5 (a) to (c) shows the mechanical work out, fluid energy input, and

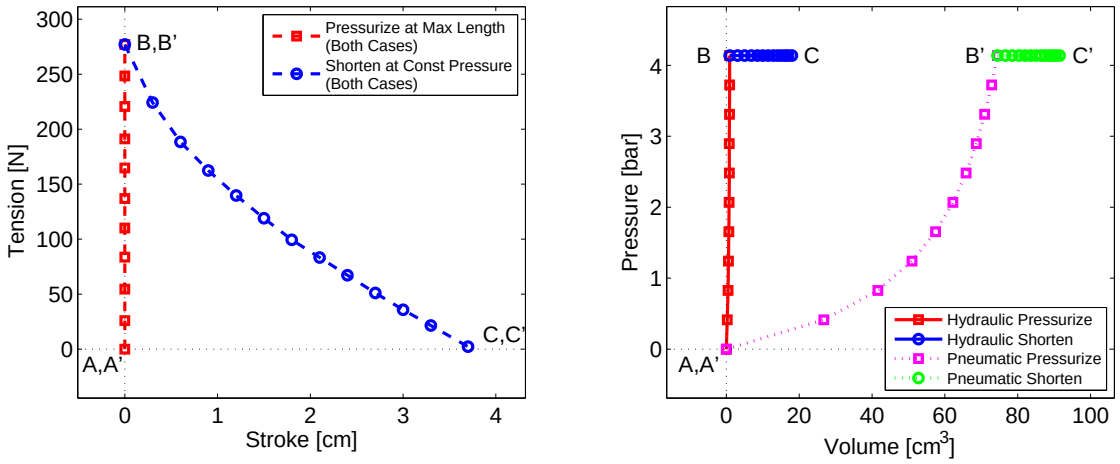

(a) (b)

Figure 1.4: (a) Tension-stroke plot that yields mechanical output work, and (b) pressure-volume plot that yields fluid input energy for a traditional FAM operating at 4.1 bar, comparing both hydraulic and pneumatic operation.

efficiency as a function of pressure respectively, and compares the efficiency of hydraulic vs. pneumatic operation. It is clear that to produce the same mechanical output work, much more fluid energy is required for the pneumatic case due to the compressibility of the working fluid. This compressibility causes hydraulic operation at 5.2 bar to be over twice as efficient. While the hydraulic efficiency increases with pressure, the pneumatic case first drops, then begins to rise again, which is likely due to the nonlinear elastic energy storage effects that are more prevalent at lower pressures.

Figure 1.5 (d) to (f) displays the mechanical work out, fluid energy input, and efficiency all as a function of contraction respectively, for hydraulic and pneumatic operation of the same latex bladder muscle at 4.1 bar. The pneumatic energy delivered is offset from the hydraulic energy input by the amount

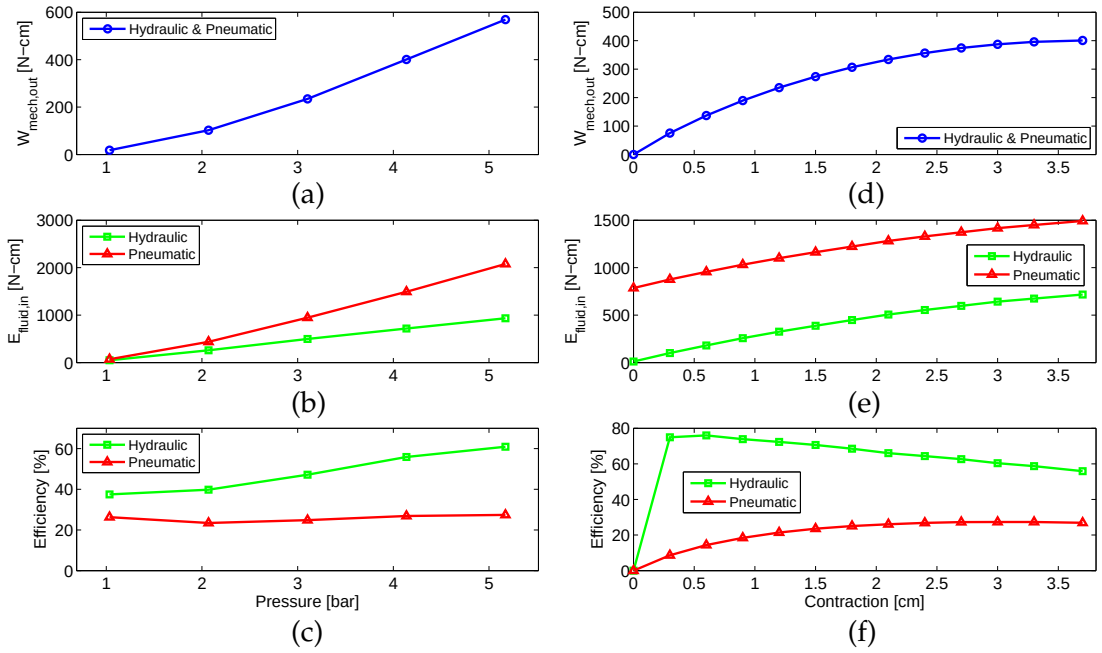

Figure 1.5: (a) Mechanical output work, (b) fluid input energy, (c) and efficiency of the latex muscle all as a function of pressure for pneumatic and hydraulic operation. (d) Mechanical output work, (e) fluid input energy, and (f) efficiency of the latex muscle all as a function of contraction at 4.1 bar for pneumatic and hydraulic operation.

of additional work required for compressing the working fluid, which can be observed in Figure 1.5 (e). This results in the highest efficiencies for the hydraulic case close to the blocked force condition, and the highest efficiencies for the pneumatic case near free contraction state due to the large amount of fluid energy required to bring the system to pressure before mechanical work is performed during the isobaric contraction.

1.4 Bladder Material

1.4.1 Construction

The motivation for investigating different bladder materials for the FAMs originated from the fact that natural rubbers, such as latex, which are most frequently used in PAMs [36] deteriorate when exposed to common hydraulic fluids. The first hydraulic fluid compatible material tested was the fluoroelastomer Viton. It was also desired to test a hydraulic fluid compatible inelastic bladder to determine if the efficiency could be further improved by avoiding elastic energy storage. Hence, the second synthetic hydraulic fluid compatible material tested was a low density polyethylene (LDPE) bag. One group reported using rubber-less artificial muscles, and they utilized an aluminum vapor deposition polyester sheet for the muscle bladder [64]. Additionally, this group did not attach one end of the bladder to the other side of the muscle, and ran them to a maximum pressure of only 1 bar. The muscles presented in this chapter need to be fluidically attached through both end-fittings to allow for air-bleeding when run hydraulically, and for our applications, higher efficiencies are desired therefore much higher pressures are utilized.

To compare the performance of each proposed bladder, all muscles were constructed using the same Kevlar mesh and crimp-on fittings to bind the components together and allow fluid flow. The Kevlar braided mesh utilized has a diameter expansion range from 1.27 cm to 2.22 cm. The end-fittings have 0.953 cm national pipe thread, and are intended for hydraulic hose with a 0.953 cm ID and 1.91 cm OD. A latex bladder muscle is used as the baseline, and the size of latex tubing used was 0.953 cm ID and 1.27 cm OD. For consistency, the Viton

bladder used was of the same dimensions. The latex bladder has a hardness of Shore 35A, while the Viton bladder has a hardness of Shore 60A [84]. The LDPE bag has a 0.051 mm (2 mil) thickness and a cylindrical diameter of 3.23 cm. It was desired to have this diameter larger than the maximum expansion of the Kevlar mesh, ensuring that the mesh, and not the LDPE bladder, bears the radial pressure forces. Since the hydraulic hose fittings are intended for larger, more rigid hosing, Buna-N spacers were included inside the fittings to guarantee that all components were bound together robustly and sealed properly. The lengths of the muscles are between 14.6 cm and 17.3 cm. The fact that they are not identical is not an issue for comparison, since the force produced is not dependent on muscle length, and the contraction is normalized to strain [31, 37]. Figure 1.6 (a) contains a picture of the shared components between the muscles, and the LDPE bladder as an example. For the LDPE bladder muscle construction, the mesh and bladder are first passed through the spacer and folded back around the spacer before insertion and swaging in the crimp-on end-fitting. A diagram of this construction method is presented in Figure 1.6 (b). To compare the effectiveness of each bladder material, the blocked force and free contraction as a function of pressure, hysteresis, and energy efficiencies are all measured.

1.4.2 Results

A series of pictures of all three muscle bladder variations is presented in Figure 1.7. To exhibit how much more the LDPE bladder contracts for the same operating pressure than the elastomeric bladder variants, Figure 1.7 (a) to (c) show the muscles at 0 bar, 0.69 bar, and 3.4 bar. It is clear that the LDPE bladder is extremely active at lower pressures, and higher pressure are required to

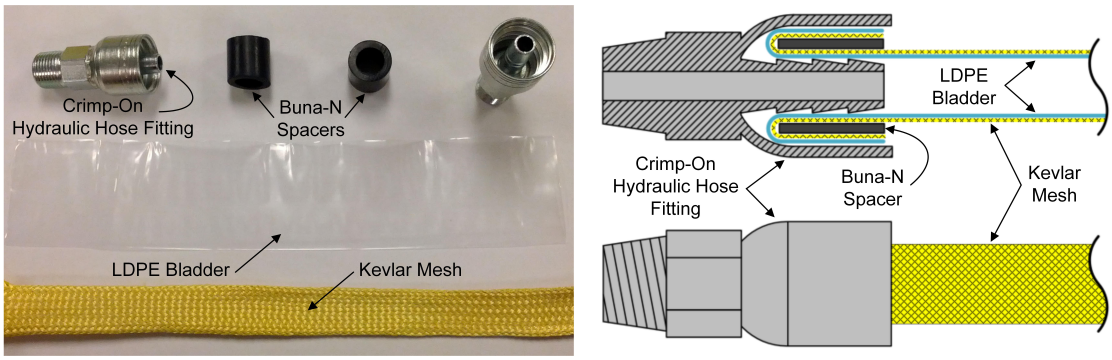

(a) (b)

Figure 1.6: (a) Picture of the components that make up the LDPE bladder muscle, (b) diagram of the construction method of the LDPE bladder muscle.

attain more similar strain values in the elastomeric bladder muscles. Additionally, since the LDPE muscle is slightly shorter than the other bladders and still contracts a larger distance, the strain values are actually more impressive than is evident in Figure 1.7. This fact is clarified in Figure 1.8, where the free contraction ratio of each bladder style is plotted as a function of pressure.

To determine how the bladder material choices affected the muscle's performance, the first set of tests performed were free contraction and blocked force experiments as a function of pressure. The results of these tests are presented in Figure 1.8. It is clear in Figure 1.8 (a) that as pressure is increased, the LDPE bladder muscle becomes active almost immediately, while the elastomeric bladder variants lag behind in their free contraction until higher pressures due to the elastic energy storage in their bladders. For comparison, assume that a free contraction level of 20% strain is desired. To obtain this with the traditional latex McKibben muscle, 2.9 bar is required, for the Viton bladder muscle, 5.3 bar is necessary, and the LDPE inelastic bladder muscle only requires 0.2 bar. In sum-

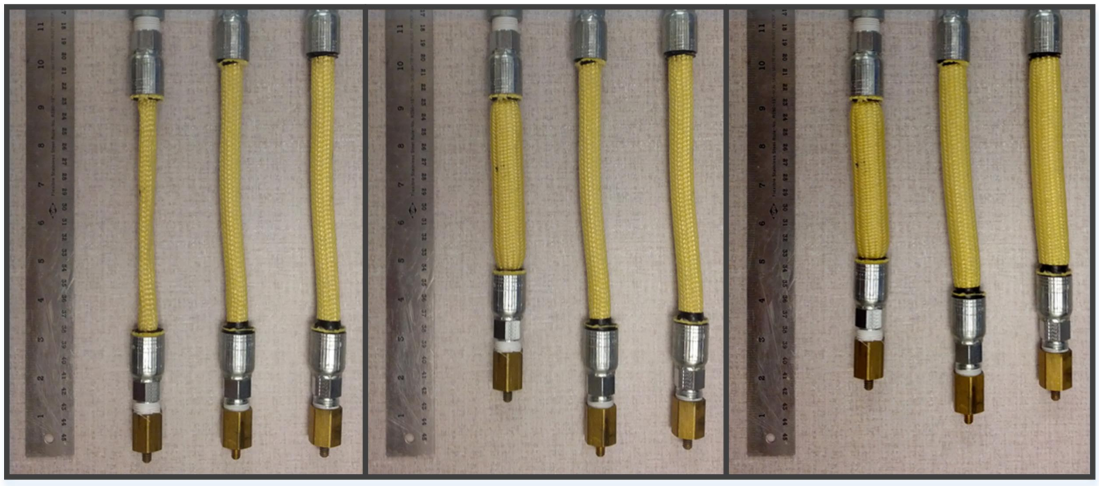

(a) (b) (c)

Figure 1.7: The bladder material of the muscles in each subfigure from left to right is LDPE, Viton, and latex. (a) All muscles at 0 bar; (b) all muscles at 0.69 bar with a very active LDPE bladder muscle and relatively inactive elastomeric bladder muscles; (c) all muscles at 3.4 bar.

mary, the bag muscle achieves the 20% strain mark at 92.9% less pressure than the latex McKibben, and the Viton muscle requires 81.2% more pressure than the latex muscle to attain the 20% contraction level. The blocked force results in Figure 1.8 (b) are similar to the free contraction results but not as exaggerated. The polyethylene inelastic bag bladder has a blocked force that is on average 28% larger than the latex bladder, and the Viton elastomeric bladder muscle has a blocked force that is on average 13% less than the latex bladder muscle. There were slight initial braid angle differences (2 degrees at the largest) in the manufacturing and testing of the different bladder muscles; using the ideal Tondu model in Equation (1.14), it predicts the LDPE bladder muscle to have an 11% larger blocked force than the latex muscle, and the Viton muscle to have a blocked force that is 7.4% less than the latex muscle. While a portion of these re-

sults are due to braid angle differences, these results still clearly demonstrate the inelastic bladder is able to exploit more of the Kevlar mesh's expansion range because no energy is being stored in the bladder. This causes higher contraction and force ranges, and makes it more useable at low pressures where traditional latex muscles would still be inactive due to the operating pressure being lower than its threshold pressure of activation.

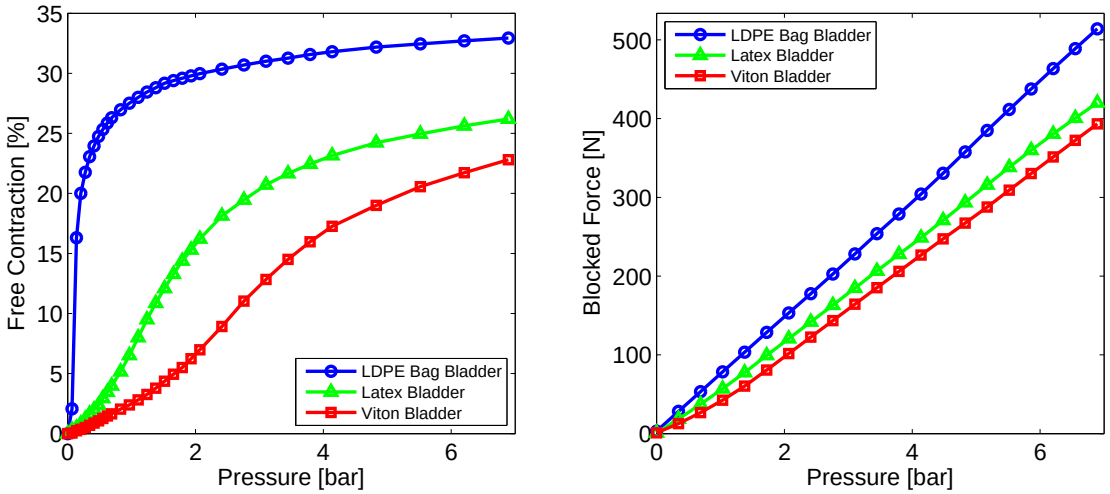

(a) (b)

Figure 1.8: (a) FAM free contraction data, and (b) blocked force data of the three bladder variants as a function of pressure.

It was also desired to determine how the bladder material selection affected the efficiency of the energy transduction as a function of pressure and contraction as presented earlier, and the results are displayed in Figure 1.9. To account for the minor differences in length of the different bladder muscles, the mechanical work output and fluid energy input are normalized by the nominal length of each muscle in Figure 1.9 (a), (b), (d), and (e). The mechanical work capacity of the LDPE bladder muscle exceeds that of the latex and Viton significantly. The fluid energy input is also higher for the LDPE bladder muscle; this is because

the extremely thin walls of the bladder allow more fluid volume to enter to the muscle. This additional fluid energy compared to the elastomeric bladders does not adversely affect the efficiencies, however since the mechanical output work also higher, and this is evident in Figure 1.9 (c). All of the muscle's efficiencies benefit from an increase in operating pressure. Figure 1.9 (d) to (f) all plot the mechanical output work, fluid input energy, and transduction efficiency all as a function of contraction at 4.1 bar respectively. Upon first glance, it is clear that the Viton bladder muscle has a limited range compared to the latex muscle, and the LDPE bladder contracts much further than the latex muscle. Additionally, the elastomeric bladder muscle's efficiencies peak towards the beginning of the stroke, while the inelastic LDPE bladder muscle's efficiency is largest near the middle of its active range, and doesn't diminish as significantly as the other muscles at larger contractions. This evidence supports our assumption that the decrease in efficiency is due to both the elastomeric bladder expanding outwards near the end of the contraction as well as the friction in the weave, since the losses are less in the inelastic bladder muscle but are still existent towards the end of its stroke.

The effect of the bladder on the amount of friction in the actuator is of interest as well. In order to experimentally quantify this, tension-strain tests were performed in the Instron machine for various pressure activation levels in both contraction and extension. This motion history yields differences in force output for a given position and pressure activation level. This hysteretic behavior is most commonly said to be a result of the strand-on-strand friction in the braided mesh because there should be no slippage between the mesh and inner elastomeric tube [78]. Other groups mention that it is a combination of the strand-on-strand friction in addition to the friction between inner tube and mesh [86].

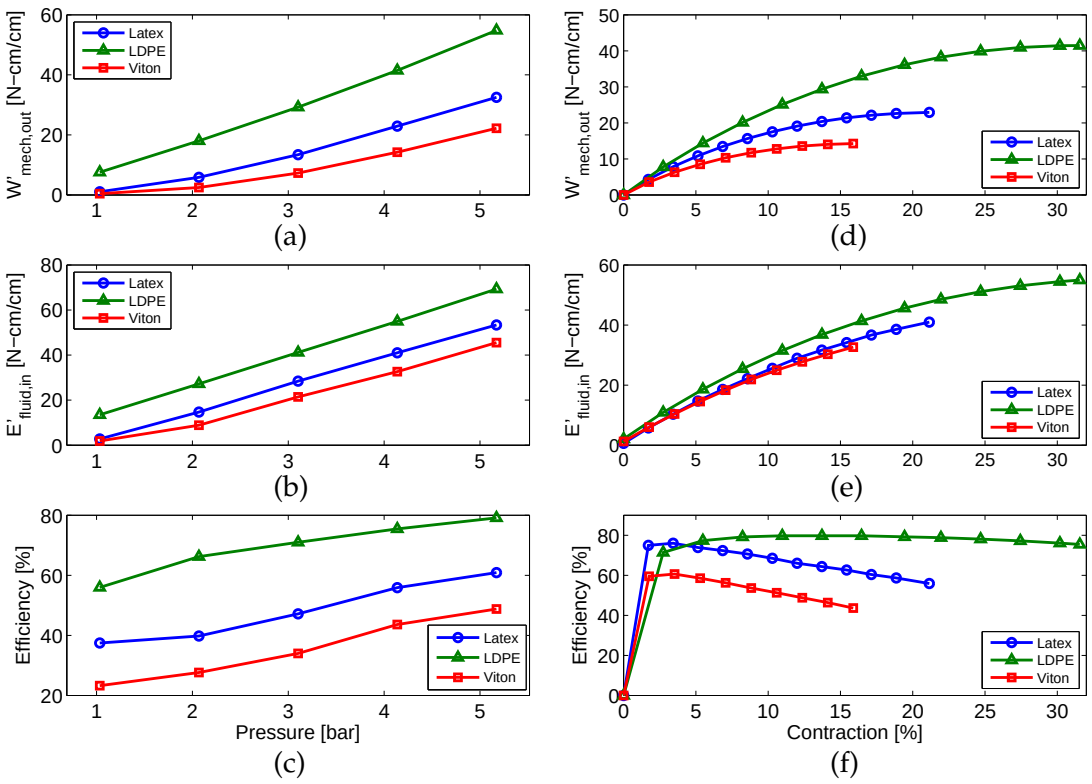

Figure 1.9: (a) Mechanical work output; (b) fluid energy input; and (c) efficiency of all 3 FAM bladder variants as a function of pressure. (d) Mechanical work output; (e) fluid energy input; and (f) efficiency of all 3 FAM bladder variants as a function of contraction at 4.1 bar.

The hysteresis loops in Figure 1.10 occur in a counterclockwise fashion, with the muscle shortening on the lower portion and the muscle lengthening on the upper curve. It is clear from observing Figure 1.10 that the latex muscle experiences the lowest amount of hysteresis, and therefore has the lowest amount of friction. The Viton bladder muscle is next, with the LDPE bladder muscle having the largest hysteresis loops and friction. This increased friction in the LDPE case is largely due to the fact that in order to function, the bladder inside has to unfold and fold as it expands and contracts, causing friction purely from the bladder sliding on itself. Additionally, since the bladder is performing this

action, it has to slide against the mesh. And lastly, the strand-on-strand friction mentioned previously still exists as well. To quantify and compare the friction that occurs in each muscle, a pressure activation level of 5.2 bar chosen, and the max hysteresis was calculated. The latex bladder muscle's maximum hysteresis is 7.0% full-scale output (FSO), the LDPE bladder muscle's maximum hysteresis is 11% FSO, and the Viton bladder muscle's maximum hysteresis is 9.9% FSO.

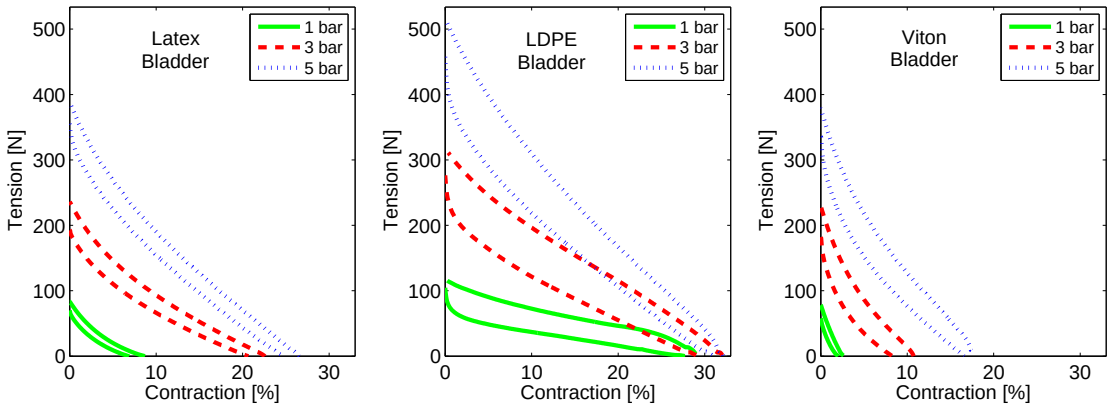

Figure 1.10: Tension-contraction plots for various pressures including hysteresis for the (a) latex bladder muscle, (b) LDPE bladder muscle, and (c) Viton bladder muscle.

1.5 Modeling

1.5.1 Volume measurement and its applications to modeling

The quasi-static force output of FAMs is often modeled using the principle of virtual work, where the force output is a function of both the operating pressure and strain. One of the most common assumptions about the volume of the

FAMs when modeling them is that they maintain a perfectly cylindrical shape throughout the full range of actuation, which is simply given in Equation (1.8) [15]:

$$V = \pi r^2 l. \tag{1.8}$$

Progression of muscle volume as it contracts is determined from the geometry of the woven Kevlar sheath. Using the pantograph opening principle that is often used in the modeling of PAMs, the following relationships are inferred [80]:

$$\frac{l}{l_0} = \frac{\cos\alpha}{\cos\alpha_0}, \qquad \text{and} \qquad \frac{r}{r_0} = \frac{\sin\alpha}{\sin\alpha_0}. \tag{1.9}$$

Substituting, using trigonometry relations, and rearranging for r as a function of initial radius, initial braid angle, and initial and current length of the muscle yields:

$$r = \frac{r_0}{\sin\alpha_0}\sqrt{1 - \left(\frac{l}{l_0}\right)^2 \cos^2\alpha_0}. \tag{1.10}$$

Substituting back into Equation (1.8) with the relation $l = l_0(1 - \varepsilon)$ gives an equation for volume where the only variable is strain:

$$V = \pi r_0^2 l_0 \left[\frac{(1-\varepsilon)}{\sin^2\alpha_0} - \frac{(1-\varepsilon)^3}{\tan^2\alpha_0}\right]. \tag{1.11}$$

The volume of fluid delivered to each muscle, ΔV, is plotted as a function of strain in Figure 1.11; to obtain this, the initial muscle volume is subtracted from Equation (1.11), and the initial small volume of fluid associated with the muscle swelling as it is brought to pressure while fixed at its longest length, V_P, is included as well:

$$\Delta V = \pi r_0^2 l_0 \left[\frac{(1-\varepsilon)}{\sin^2 \alpha_0} - \frac{(1-\varepsilon)^3}{\tan^2 \alpha_0} - 1 \right] + V_P. \tag{1.12}$$

It is clear in Figure 1.11 that assuming the muscle takes on a cylindrical shape throughout its entire contraction range produces an extremely accurate model of the evolution of the volume of the muscle over its stroke for the muscle tested. It is also noted that the trend for actuator volume as a function of stroke is independent of pressure; for higher pressures, the volume travels further along the curve because higher strains are attained. The fact that the volume for a specific contraction ratio is independent of pressure also substantiates that the assumption of inextensible fibers in the mesh is accurate. The initial muscle swelling volume is minute and very similar for the latex and Viton bladders, but much larger for the LDPE bladder. This is because in the unpressurized state for the elastomeric bladder muscles, the braid is in contact with the bladder, but is not extremely tight. When pressure is applied, this small amount of slack is taken out. For the LDPE bladder muscle however, there is much more slack in the braid due to the amorphous nature of the bladder. This is observed as an increased volume of fluid required to take the slack out of the mesh.

The shortest muscle used was the LDPE bladder muscle, and it's slenderness ratio was $l_0/r_0 = 23$. This cylindrical muscle model worked well for this slenderness ratio, and should for slenderness ratios above this. It is expected for a

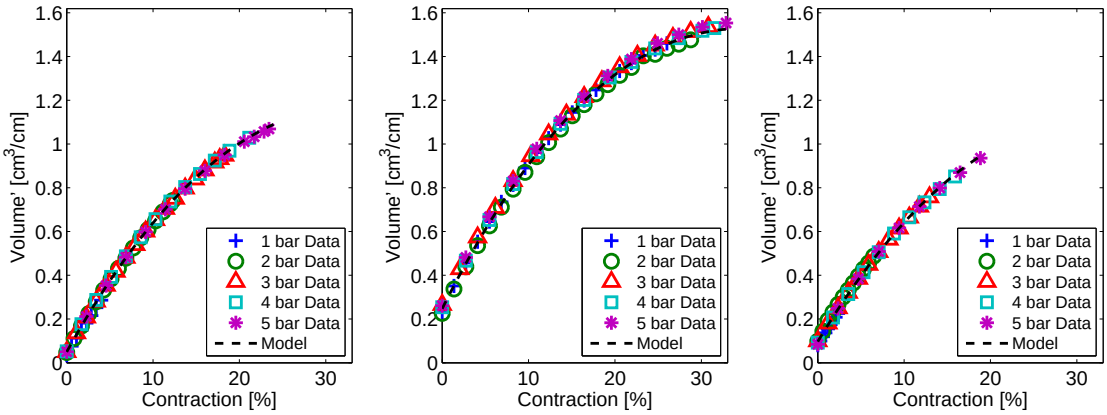

Figure 1.11: Volume as a function of contraction ratio for the (a) latex bladder muscle, (b) LDPE bladder muscle, and (c) Viton bladder muscle.

very low slenderness ratio muscle, the end effects near the fittings will dominate, and more complex modeling of the muscle geometry will be required. The use of such a low aspect ratio muscle would be limited to higher force, shorter stroke applications. Different braided sheaths with very low initial braid angles may have more pronounced conical end effects as well.

The muscle shape not remaining perfectly cylindrical near the end-fittings is often cited as a reason for models over-predicting free contraction [31, 34, 37, 77, 80, 81]. As a result, more complex models have been developed to take into account the shape at the ends of the muscles by including conical segments [77, 78, 81], while others model the actuator ends as circular arcs [31, 37]. The results of these experiments show that modeling the muscles presented in this chapter as cylinders is quite volumetrically accurate. This will likely vary depending on the mesh material used. Consequently, for our specific Kevlar mesh muscle construction with slenderness ratios greater than 23, it seems that blad-

der effects dominate as the reason for the virtual work model errors and the volumetric end effects are comparatively much less significant. Therefore, efforts to improve the modeling of these Kevlar mesh actuators should be focused more on other mechanical phenomena. And groups have done this already in a variety of methods, such as including energy storage effects in the bladder using a Mooney-Rivlin approach [7, 31, 36, 37, 78].

Since the volume predicted and hence force output of the muscles is extremely sensitive to the initial radius and initial braid angle, the volume measurement data was used to determine the appropriate initial braid angle for the model, using an initial radius of 0.635 cm. This was found to be a more accurate method than trying measure or calculate it otherwise. The initial braid angle was found to be 28.7 degrees. These values are used in the principle of virtual work models below.

The force produced by the muscle can be represented as a function of pressure and contraction ratio using the principle of virtual work. This technique presented by Tondu [80] is utilized, beginning by equating the fluid energy input to the mechanical work output:

$$F = -P\frac{dV}{dl}, \tag{1.13}$$

where F is the force produced by the FAM, P is the operating pressure, V is the muscle volume, and l is the muscle length.

Taking the partial derivative of Equation (1.11) with respect to strain, and employing the relationship that $l = l_0(1 - \varepsilon)$, we arrive at:

$$F = \left(\pi r_0^2\right) P\left[a\,(1-\varepsilon)^2 - b\right], \tag{1.14}$$

where a and b are constants associated with the initial mesh geometry: $a = 3/\tan^2\alpha_0$, and $b = 1/\sin^2\alpha_0$.

Since we now know that our model should have the correct initial braid angle and initial radius from the volume model and data, we wanted to determine if inaccuracies of these values caused the models to deviate from the data in other work. Therefore the ideal model in Equation (1.14) with the determined initial braid angle and initial radius from the volume measurement section is plotted in Figure 1.12 with experimental data.

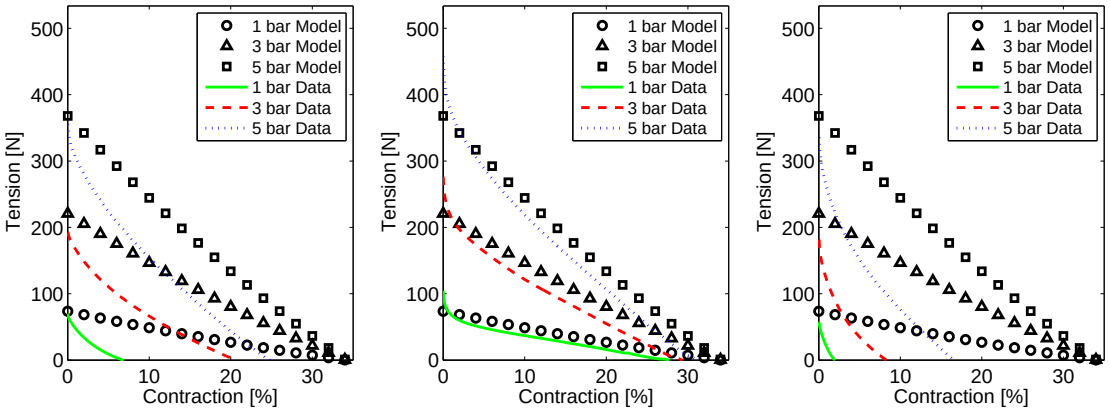

Figure 1.12: Experimental data with ideal virtual model and volumetrically determined initial braid angle for (a) latex bladder muscle, (b) LDPE bladder muscle, and (c) Viton bladder muscle.

The ideal force model resulted in reasonably accurate predictions of the blocked force condition for all the muscles at varying pressures. As stated earlier, the model over-predicts the free contraction condition and this is evident

for the elastomeric bladders in Figure 1.12 (a) and (c). The experimental results for the 0.051 mm (2 mil) LDPE bladder are much closer to this ideal thin-walled cylinder model of the McKibben, with the free strain condition being less dependent on pressure as is predicted in the model. It is observed in Figure 1.12 (b) that the maximum strain is still slightly less than the 34% predicted by the model.

1.5.2 Using free strain and blocked force data to improve the virtual work model

In order to get the model to more closely match the experimental data, one could use more complicated models such as some of the aforementioned methods of including the elastic energy storage in the elastomeric bladders and friction. Tondu and Lopez proposed using a tuning parameter, κ, to reduce the modeled maximum contraction closer to the actual maximum contraction:

$$F = \left(\pi r_0^2\right) P \left[a\left(1 - \kappa\varepsilon\right)^2 - b\right]. \tag{1.15}$$

This tuning parameter was presented as being able to be employed as either a constant or as an exponential function of pressure [80].

Colbrunn *et al.* uses a correction factor called an 'effectiveness' term which is essentially a ratio of the measured force of the actuator to the modeled force. It is multiplied with the theoretical force output since the model tends to over-predict these values. This effectiveness term is a function of pressure. They

emphasize their development of a simple model that is adequate for control and dynamic simulations [17].

$$F_{real} = Eff(P) \cdot F_{theor}, \tag{1.16}$$

where F_{real} is the actual force output, $Eff(P)$ is the effectiveness term as a function of pressure, and F_{theor} is the theoretically predicted force output using Tondu's model in Equation (1.14). Both of the 'tuning parameters' presented by Tondu and Lopez, and Colbrunn et al appear to be determined ad hoc until the results match experimental data. We took an approach that blends both of their methods, but also directly incorporates trends obtained from experimental data rather than adjusting constants until the model and experiment line up. This is an expedient method that results in reasonable models, and avoids using more complex methods such as Mooney-Rivlin that require many constants to be determined empirically [36]. The proposed modified model is given by:

$$F_{mod} = \kappa_F \left(\pi r_0^2\right) P \left[a\left(1 - \kappa_\varepsilon \varepsilon\right)^2 - b\right], \tag{1.17}$$

where the force tuning parameter is the ratio of the measured blocked force function to the model predicted maximum force:

$$\kappa_F = \frac{F_{meas,max}(P)}{\left(\pi r_0^2\right) P\left(a - b\right)}, \tag{1.18}$$

and the strain tuning parameter is the ratio of the model predicted maximum strain to the measured maximum strain trend:

$$\kappa_\varepsilon = \frac{1}{\varepsilon_{meas,max}(P)}\left(1 - \frac{1}{\sqrt{3}\cos\alpha_0}\right). \tag{1.19}$$

All other parameter definitions remain the same as the Tondu and Lopez model in Equation (1.14). It is noted the way the tuning parameters are defined here, κ_F will usually be slightly less than one, and κ_ε will typically be slightly greater than unity.

To employ this technique, the blocked force and free contraction characteristics were obtained experimentally for the three bladder muscle varieties as a function of pressure, presented previously in Figure 1.8, and then curve fitting was applied to generate trends unique to each muscle due to their different bladder materials, which is seen in Figure 1.13. Simple logarithmic or low order polynomial fits were used.

Plotting the trends for the maximum free strain and blocked force with the experimental results shows the degree to which these trends match the data in Figure 1.13.

Using the trends shown in Figure 1.13 in conjunction with Equations (1.17), (1.18), and (1.19) yields the plots in Figure 1.14. The forces and strains predicted show significant improvement compared to the standard model. The intercepts line up due to the free strain and blocked force tuning parameters, however in between these intercepts, the force is slightly over-predicted. This minor difference is due to the fact that the tuning parameters only adjust for the free strain and blocked force, and cannot fully account for the losses associated with the nonlinearities that arise from elastic energy storage in the bladder and friction throughout contraction in between these two points. It is important to point

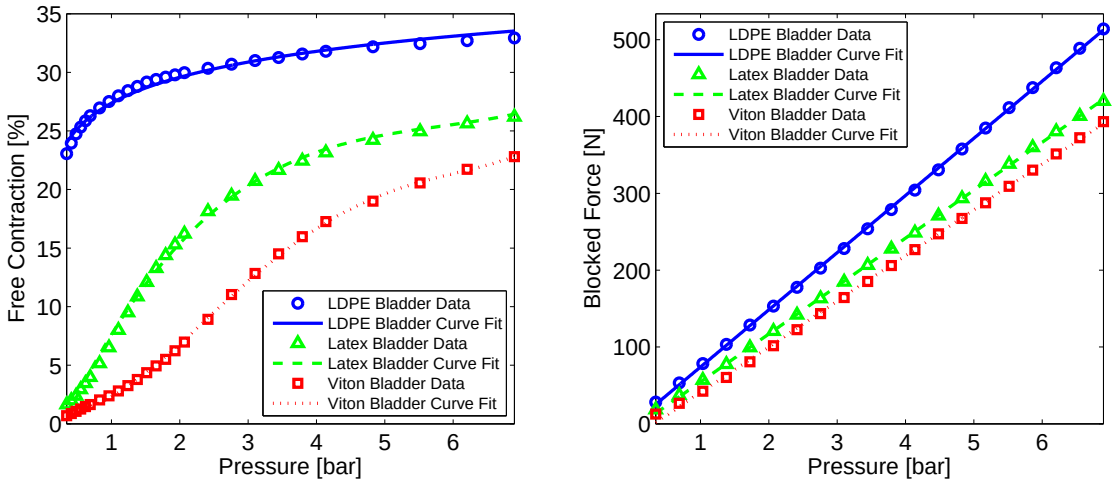

(a) (b)

Figure 1.13: (a) Free contraction trends and (b) blocked force trends plotted with the experimental data for all three muscle variants.

out that the way the free strain and blocked force experiments were performed gives these values for the contraction case, or rather, the lower portion of the hysteretic tension-strain curve. This is because only the contraction case is of interest to us since modeling of the efficiency study conducted only requires this contraction case. Hence, attempting to model the hysteresis is not part of our efforts. However, if including this hysteretic behavior is of concern, we propose using the same method in Equation (1.17), but have separate force and strain tuning parameters, κ_F and κ_ε respectively, for the contraction and extension cases. This of course necessitates additional experiments.

To model the efficiencies of the different muscles, the same efficiency definition is used from Equation (1.3). This time however, the force that is integrated in the mechanical work in Equation (1.2) is the modified force equation proposed in Equation (1.17). And for the fluid input energy, instead of integrating

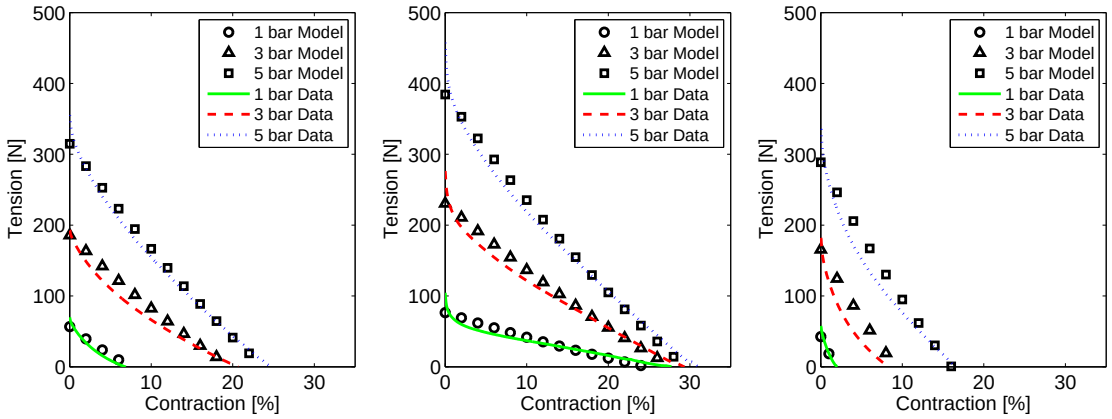

Figure 1.14: Proposed adjusted virtual work model with data for the (a) latex bladder muscle, (b) LDPE bladder muscle, and (c) Viton bladder muscle.

the pressure volume curve as in Equation (1.3), the operating pressure is multiplied by the fluid volume delivered, which is a function of strain, as defined in Equation (1.12) instead. The modeled efficiency is expressed as:

$$\eta_{FAM,mod} = \frac{l_0 \int_0^{\varepsilon_{meas,max}} F_{mod} d\varepsilon}{P\Delta V\left(\varepsilon_{meas,max}\right)}. \tag{1.20}$$

It was desired to assess how well the modeled efficiency matches experimental data both as a function of pressure and strain, and also to use this model to predict efficiencies at pressures above, below, and in between the 5 discrete pressures tested experimentally. This model is appropriate over the range 0.34-6.9 bar because the curve fits of the free contraction and blocked force over these pressures are included in the model. This model is plotted with the data in Figure 1.15. As expected it represents the data reasonably well, but could certainly be improved with more advanced modeling methods. The model predictions

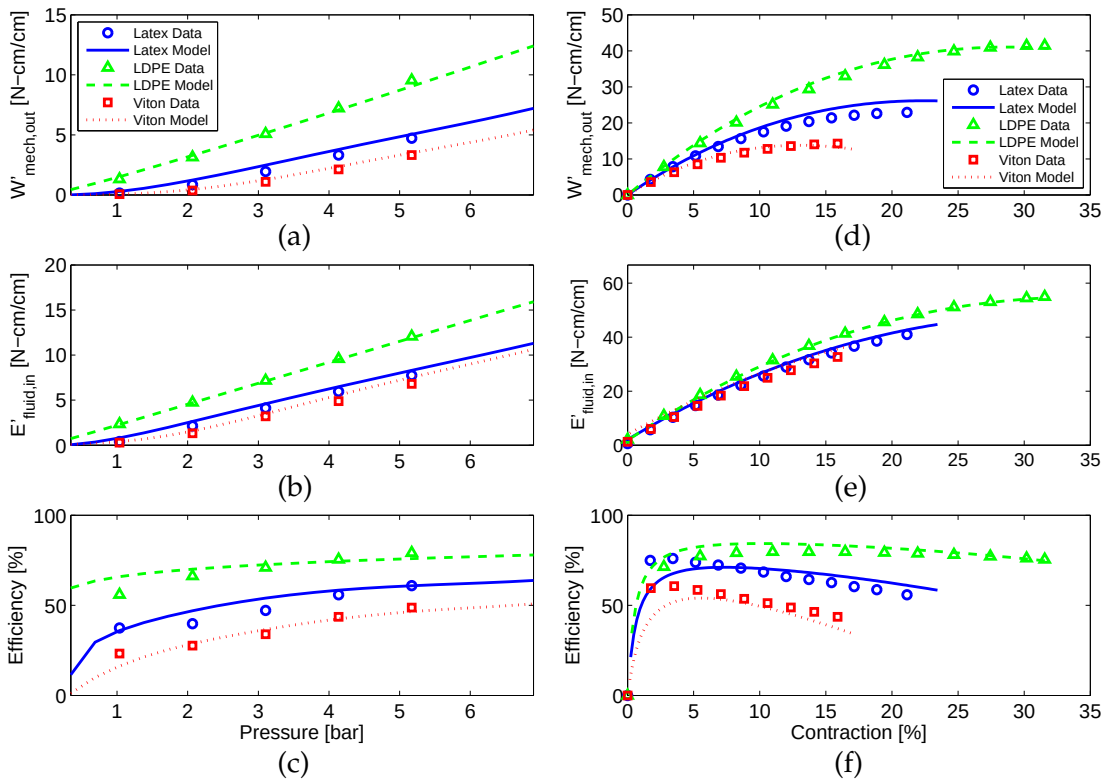

Figure 1.15: Model and experimental data for (a) mechanical output work, (b) fluid input energy, and (c) efficiency all as a function of pressure. Model and experimental data for (d) mechanical output work, (e) fluid input energy, and (f) efficiency all as a function of contraction for all the muscles at an operating pressure of 4.1 bar.

show that the efficiencies are very low at low pressures, due to not fully activating the muscles, and the efficiencies at higher pressures keep increasing but begin to plateau. The efficiency of the LDPE muscle begins to level off around 80%, which is comparable to hydraulic cylinders, which typically exhibit efficiencies in the range of 85% - 95%, and the associated losses are primarily from the piston seal friction [42].

1.6 Conclusions

This chapter first established a method to experimentally characterize the transduction efficiency of FAMs when converting the fluid input energy to mechanical output work. In order to discover where these actuators perform best, these net-work efficiency experiments were performed over a range of operating pressures, in addition to studying the effects of the muscle's contraction state. To achieve the best efficiencies for a traditional latex bladder FAM, it was determined that higher operating pressures and actuating in a stroke range closer to the blocked force was best. The muscle tested achieved over 60% efficiency at 5.2 bar over one full action cycle, and if the stroke range was limited, efficiencies of over 80% were possible.

Once these efficiency metrics were defined, they were utilized to compare traditional pneumatic operation of these actuators to running them hydraulically. We found that maximum efficiencies over the pressure range tested resulted in hydraulic operation being over twice as efficient as the pneumatic case due to its higher bulk modulus. While the hydraulic case performed more efficiently near the beginning of contraction, the pneumatic case efficiency improved until about halfway through the stroke and plateaued for the remainder of the actuation cycle. Since it is desired to utilize McKibben artificial muscles in hydraulic systems, and latex will deteriorate if used with hydraulic oil, a brief investigation of two new synthetic hydraulic fluid resistant bladders was conducted. Viton was the first alternative presented, and is elastomeric as well. The tubing was of the same thickness as the latex, but due to material properties was stiffer. This resulted in inferior contraction abilities in addition to reduced efficiencies. The second hydraulic fluid compatible bladder alternative presented

was an inelastic LDPE bag. The LDPE bladder had to fold and unfold within the mesh as the muscle was activated. This muscle was superior in force output, contraction, and efficiency compared to the other two elastomeric bladder muscles. The LDPE muscle has a maximum efficiency of almost 80%. It activates almost immediately, unlike the elastomeric bladder variants that have a threshold pressure to overcome. Fatigue is a potential concern with this type of bladder construction due to the frequent sliding of the bladder over itself during operation. All of the muscle bladder variants presented were tested on the order of hundreds of cycles and no fatigue issues were experienced by any of them however. The only drawback of the LDPE bladder muscle discovered thus far is its increased hysteresis.

This chapter originally appeared as:

Michael A Meller, Matthew Bryant, and Ephrahim Garcia. Reconsidering the McKibben muscle: energetics, operating fluid, and bladder material. *Journal of Intelligent Material Systems and Structures*, 25(18):2276–2293, 2014.

CHAPTER 2

IMPROVING ACTUATION EFFICIENCY THROUGH VARIABLE RECRUITMENT HYDRAULIC MCKIBBEN MUSCLES: MODELING, ORDERLY RECRUITMENT CONTROL, AND EXPERIMENTS

2.1 Introduction

2.1.1 Fluidic artificial muscles and actuation in robotics

Fluidic artificial muscles (FAMs) are an attractive actuator choice among the robotics community due to their extremely light weight, inherent compliance, cost effectiveness, and high force capacity [78]. FAMs have been employed on humanoid walking robots [13, 85, 76, 54], robotic arms [40, 79, 62, 12], and various lower and upper extremity orthotic devices [82, 25, 56]. Also known as McKibben muscles (named for their inventor), these actuators are comprised of a helically braided mesh that surrounds an inner elastomeric bladder. These parts are fluidically activated through a port on one end of the actuator, while the other end is plugged. Both ends attach mechanically to other structures, much like tendons attach skeletal muscle to bones.

The vast majority of FAMs are operated pneumatically, with just a few other research groups actuating them hydraulically [27, 51, 77, 66, 92]. Pneumatic operation enhances the compliance of the actuators, and also allows venting of the pneumatic artificial muscles (PAMs) directly to the atmosphere. Using compressed air as the fluid medium has drawbacks as well; valve-controlled pneumatic systems are typically less than half as efficient as equivalent hydraulic

systems due to their significantly lower bulk modulus [9].

Hydraulic control systems have become increasingly popular as the means of actuation for human-scale legged robots and assistive devices. Some examples include IIT's quadruped HyQ [68], Boston Dynamics' line of quadrupeds such as BigDog [59], Boston Dynamics' bipeds Petman [53] and Atlas [1], Sarcos' biped Primus [74], Raytheon Sarcos' exoskeleton XOS 2 [6], and Lockheed Martin's lower extremity exoskeleton HULC [4]. Hydraulic actuation was likely chosen for these applications due to its high actuator power-to-weight ratio [47, 32].

One of the most significant limitations of robots like these is their run time when untethered from a power source. The AMBER Lab at the Georgia Institute of Technology recently set the record with over 2.5 hours of walking on one battery charge with their DURUS robot [61]. Several groups have been exploiting the passive dynamics of their robots to reduce their cost of transport, including Collins *et al.* with the Cornell biped [18], Ramezani *et al.* with their ATRIAS robot [60], and Cousineau *et al.* with their DURUS robot [19]. The cost of transport (COT) is a dimensionless energy efficiency metric often used for comparing dissimilar vehicles and even animals; it is defined as the ratio of the input energy to the weight times forward distance traveled [39]. This methodology of working with the robot's dynamics is a proven approach to increase energetic efficiency, but is only part of the solution. The best reported COT for a true humanoid robot is 1.6 for DURUS, while the COT for humans is about 0.2 [61]. This difference of an order of magnitude is thought to be largely due to actuation efficiency [21].

2.1.2 Hydraulic control system limitations

While hydraulics has grown in popularity in robotics, it also has several disadvantages. The precise machining needed in the electrohydraulic servovalves (EHSVs) and ability to withstand high pressures make these systems costly [47]. There is also the risk of oil spillage, and the requirement of a return line to bring fluid back to the reservoir. The inherent rigidity of hydraulics is favorable from a controls and efficiency standpoint, but potentially dangerous when considering human-robot interaction.

Even though valve-controlled hydraulic systems tend to have overall efficiencies more than double that of pneumatic systems, efficiency is still one of its largest drawbacks [9, 41]. Typical mobile hydraulic systems have been reported to have overall efficiencies between 10–20% [41, 24]. Individual component efficiencies (pumps and cylinders) are on the order of 90%, however. Therefore the system design and usage is to blame for these low overall efficiencies. This suggests that with the addition of some hardware and more advanced control techniques, there is great potential to improve the efficiency of these systems.

Fluid power actuators are sized for peak loading conditions, but usually operate far below these design points. If the end effector needs to produce a force less than its sized maximum, the pressure applied to the actuator must be reduced, resulting in large throttling losses across the servovalves. In typical mobile hydraulic applications, 43% of the input power is lost in this manner [41]. If a system is poorly designed, or there is a large discrepancy between the sized maximum and normal operating conditions, then even more power can be expected to be lost.

2.1.3 Variable recruitment in skeletal muscle

Humans and other animals have far lower COTs than today's robots, in part attributed to the efficient actuation performed by the central nervous system and skeletal muscle through a process known as orderly recruitment. The smallest subunit of a muscle that can be recruited is called a *motor unit*. This unit is activated by a separate nerve ending, and commands as few as 3 muscle fibers for fine control in locations such as our eyes or fingers, and as many as 2000 muscle fibers for more granular control of the large muscle groups in our legs [88].

The excitation of each motor unit is done in a binary fashion. To increase the force output, the first active motor unit's firing rate is increased. Once the tension is high enough, a recruitment threshold is reached. At this point, another motor unit is excited at its base activation rate. The first active motor unit's maximum firing rate is achieved *after* the next motor unit is added. This helps ensure smoother transitions between the different recruitment states. As force requirements diminish, motor units become inactive in the opposite order in which they were recruited. This means the first motor units recruited are active the longest, which is why the smaller slow-twitch units are called upon first. These *tonic units* are fatigue resistant due to their high numbers of mitochondria. The *phasic units* are recruited last, according to Henneman's size principle, since these are the larger fast-twitch motor units more prone to fatigue [29].

2.1.4 Variable recruitment FAMs

Recently, for the purpose of increasing the actuation efficiency of FAMs, several research groups have attempted to emulate the orderly recruitment of skele-

tal muscle motor units [10, 62]. Bryant *et al.* proposed using variable recruitment hydraulic artificial muscles (HAMs) to reduce throttling losses in the servovalves, and the associated efficiency gains were shown with a quasi-static model. Their developed muscle bundle had one small motor unit and one large motor unit (both comprised of three McKibben muscles), analogous to tonic and phasic units in skeletal muscle [10]. Robinson *et al.* also developed a variable recruitment muscle bundle, but with six equally sized McKibben muscles. They powered theirs pneumatically, and suggested that fewer active PAMs would also reduce energy lost to elastic energy storage in the bladders. They performed simulations, and showed experimentally that fewer active PAMs consumed less fluid energy from their pneumatic pressure source [62]. Both of these studies showed promise for variable recruitment McKibben muscles (both hydraulically and pneumatically), however neither showed active selective recruitment, or investigated how to handle recruitment level shifts.

In this chapter, we further investigate variable recruitment hydraulic McKibben muscles with the goal of significantly improving actuation efficiency. We perform quasi-static force-stroke experiments on the full muscle bundle, and develop a volume measurement-based method to estimate an effective initial braid angle for each recruitment level. Using these mesh angles, we then take a standard virtual work approach with our semi-empirical model; this model is used to predict the efficiency gains of variable recruitment. Next, we develop the first reported real-time state machine-based variable recruitment FAM controller. This approach is inspired by automatic transmission gearshift controllers, where recruitment level is analogous to gear ratio; we use pressure thresholds in our shift schedule as opposed to throttle percent and engine speed [55, 38]. This state machine determines which gains to use in the classical

proportional-integral (PI) controller, as well as which servovalves are active. To quantify the efficiency gains associated with this actuation scheme, a series of experiments were conducted on our robot arm. With the variable recruitment controller employed, the fluid power consumed was monitored for several load-lifting cases, and compared to a single equivalent muscle (SEM) with throttling control only. The results demonstrated that there is a significant advantage to variable recruitment, however more research is needed to improve its tracking abilities.

2.2 Muscle bundle development

2.2.1 Hydraulic McKibben muscle fabrication

The McKibben muscles used in this chapter must be hydraulic oil compatible and capable of withstanding pressures greater than 1379 kPa (200 psi). The natural latex rubber that is most often employed as the bladder will break down when exposed to any type of hydraulic oil, hence silicone was chosen for its compatibility [2]. The bladder used has an inner diameter of 9.53 mm ($\frac{3}{8}$ inch), and an outer diameter of 12.7 mm ($\frac{1}{2}$ inch). It has a shore hardness of 35 A which is consistent with most other latex and silicone bladder McKibben muscles [62, 45, 58]. We chose Kevlar as the braided mesh due to its high strength fibers and dense weave. This mesh has an expansion range of 12.7 mm ($\frac{1}{2}$ inch) to 22.2 mm ($\frac{7}{8}$ inch) in diameter, which yields a sufficient range of motion. Each FAM was constructed to have a 17.78 cm (7 inch) active length, measured between the end fittings. To bind the mesh and bladder together and allow for

fluidic connection to our hydraulic system, Eaton Weatherhead 06Z-R06 steel o-ring boss (ORB) swivel crimp fittings were used. ORB fittings were chosen over national pipe thread (NPT) since this lends itself better to frequent configuration changes. The swivel functionality of the fittings facilitates the full bundle assembly by preventing each McKibben muscle from twisting during installation.

2.2.2 Custom bundling manifold design and assembly

The muscle bundle developed in this chapter consists of six total parallel McKibben actuators. The HAMs can be activated in separate pairs – two, four, or six at a time. In order to solely produce axial contraction and avoid bending torques, each pair of McKibben muscles is arranged symmetrically about the central mechanical attachment point of the bundling manifold. Since it is desired to control each McKibben pair with one EHSV, each pair is fluidically connected in its own layer in the manifold while remaining isolated from the other pairs. This is shown in the CAD diagram of the manifold in Figure 2.1.

The individual McKibben muscles were then threaded into the custom bundling manifold end caps, and the completed assembled muscle bundle is shown in Figure 2.2. Quick-disconnect hydraulic hose fittings were used to allow for the connection of each McKibben pair to its EHSV, and brake bleeder screws were added to assist with bleeding air out of the system. This is important because as little as 1% entrained air can result in a decrease in the effective bulk modulus by 75% [47].

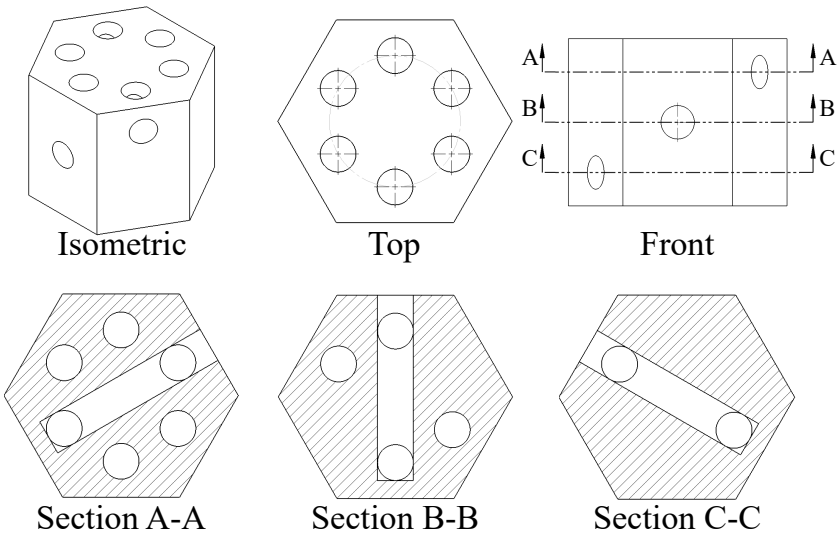

Figure 2.1: Schematic of the custom bundling end cap manifold that both mechanically binds all of the HAMs together and fluidically connects the appropriate pairs.

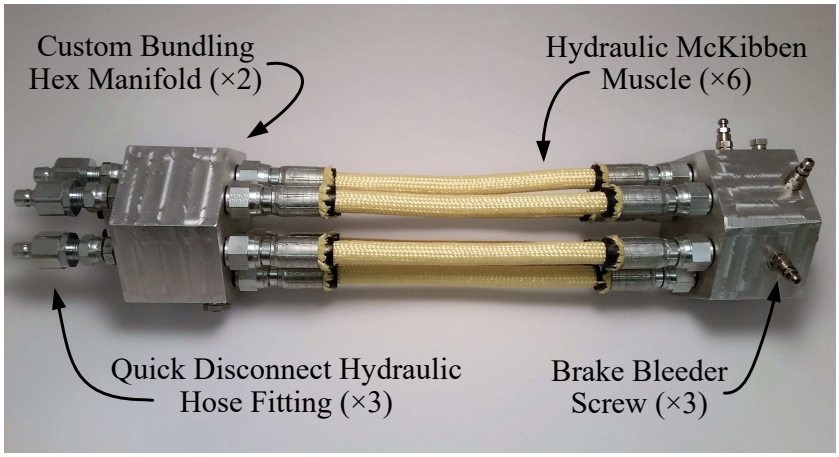

Figure 2.2: Fully assembled muscle bundle, comprised of three McKibben pairs.

2.2.3 Motor unit and recruitment level definitions

Mentioned previously, the smallest subunit of skeletal muscle that can be controlled is called a motor unit [88]. For this reason, we refer to each fluidically

connected pair of McKibben muscles as a *motor unit (MU)*, since this too is the smallest subunit that can be controlled in the proposed actuation scheme. Each hydraulic McKibben muscle serves as a *muscle fiber*. Since all of the McKibben muscle fibers were constructed to be nearly identical, each motor unit produces approximately the same force output with a given pressure. Throughout operation, the bundle will shift between different *recruitment levels (RLs)* comprised of varying numbers of active motor units. The definitions of the motor units and recruitment levels are visualized in Figure 2.3.

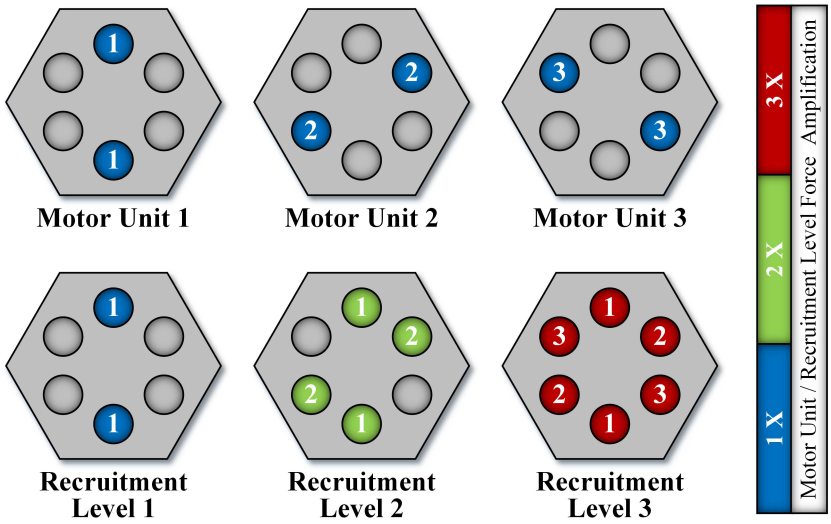

Figure 2.3: Definition and force amplification of motor units and recruitment levels.

2.2.4 Effect of total number of recruitment levels on efficiency

In the development of the variable recruitment muscle bundle, it was desired to estimate the effect of the total number of recruitment levels on the efficiency gains. Since throttling in the servovalves is the dominant reason for the actuation inefficiencies, we only consider throttling when performing this brief

theoretical study. It is somewhat intuitive that higher numbers of motor units will result in higher efficiencies, but the trend it follows is not. Skeletal muscle has a remarkably high number of motor units per muscle bundle – each biceps brachii is estimated to have 774 motor units that control a total of 580 000 muscle fibers [35].

In framing this simulation, we must consider how recruitment will be handled in an ideal sense. We first assume that the McKibben muscle bundle is comprised of equally sized motor units in a parallel arrangement. Each motor unit is comprised of a pair of McKibben muscles with one servovalve controlling them. The bundle starts with one motor unit active (receiving a positive gauge pressure from its EHSV), while the rest are inactive (their EHSVs are set to vent to the reservoir).

As the force requirements increase, the pressure in the active motor unit increases. Once the pressure in this motor unit reaches the supply pressure, it is now saturated and has reached a recruitment threshold. Now one additional motor unit is recruited, with the first motor unit still active. This is called recruitment level 2, because it has motor units 1 and 2 active. Immediately following the recruitment level change from RL1 to RL2, the effective average recruitment level pressure changes from 100% to 50% of supply pressure since one motor unit is at 100% while the other is at 0%. Once RL2 is saturated, it will recruit a third motor unit, at which point the recruitment level pressure will drop to 67% of supply pressure since two motor units will be at 100% while the third will be at 0%.

We can mathematically state that the minimum and maximum pressures of each recruitment level are given by

$$P_{RL,min,i} = \frac{i-1}{i} P_S, \text{ and} \tag{2.1}$$

$$P_{RL,max,i} = P_S, \tag{2.2}$$

respectively, where i is the positive integer representing the current recruitment level (total number of active motor units) and P_S is the supply pressure. The percent operating efficiency is defined as

$$\eta_{op} = \frac{P_{RL}}{P_S} \times 100, \tag{2.3}$$

where P_{RL} is the pressure in the active elements of the bundle. We assume there is no leakage, so the flowrate out of and into the valve is the same; hence the efficiency is simply the ratio of the recruitment level pressure to the supply pressure [47].

Using Equations (2.1), (2.2), and (2.3), we can now define the minimum and maximum percent efficiencies of each recruitment level as

$$\eta_{op,min,i} = \frac{i-1}{i} \times 100, \text{ and} \tag{2.4}$$

$$\eta_{op,max,i} = 100, \tag{2.5}$$

respectively. To consider an average case, we assume that the load requirements are such that the variable recruitment muscle bundle spends equal time spanning its entire mechanical working range. As a result, it will spend equal

time in each recruitment level, and equal time between the minimum and maximum pressures of each recruitment level. With these assumptions, we can now estimate the average operating efficiency as a function of the total number of recruitment levels, given by

$$\eta_{op,avg,tot} = \sum_{i=1}^{n} \frac{2i-1}{2ni} \times 100, \tag{2.6}$$

where n is the positive integer corresponding to the total number of recruitment levels of the muscle bundle. Equation (2.6) is plotted in Figure 2.4, and it can be observed that using solely one recruitment level yields 50% average efficiency; this is the typical single muscle configuration where only throttling is used to attain any force level below maximum. It is noted that if standard practices were used, servovalve operation would only occur below 67% of supply pressure rather than the 100% we are allowing [47]; this would result in lower efficiencies but higher control authority. Using 10 recruitment levels gives over 85%, but 44 are needed to get over 95% efficient. This shows that increasing the total number of recruitment levels causes the theoretical average operating efficiency to increase monotonically, but with diminishing returns. We could have chosen any integer greater than one, but we selected three motor units in this proof of concept muscle bundle simply because it is readily realizable in hardware, and should theoretically produce a 38.8% increase in efficiency (19.4% difference) with only the addition of two motor units compared to the traditional case.

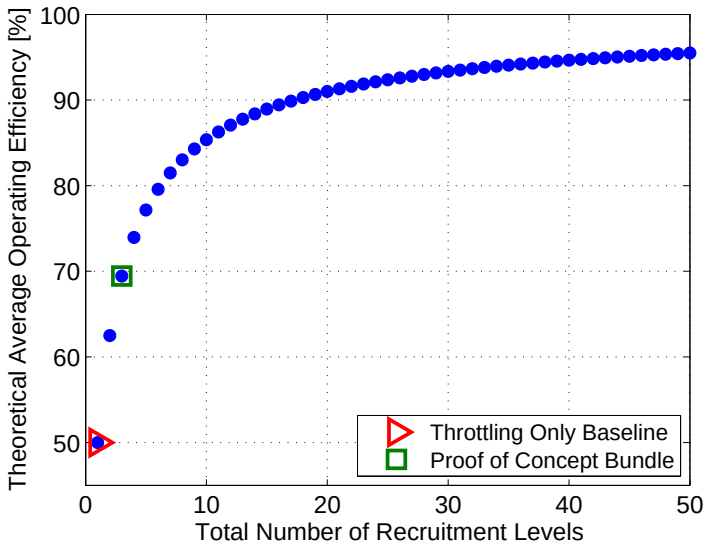

Figure 2.4: Theoretical average operating efficiency versus the total number of recruitment levels (made up of equally sized motor units) comprising a full muscle bundle.

2.3 Muscle bundle characterization

Several force-strain characterization experiments were performed to determine how the full muscle bundle behaves over a variety of operating conditions. All tests were performed on the linear dynamometer developed in the LIMS Lab at Cornell University. This setup is similar to a typical materials tensile-testing machine, but allows for more custom and dynamic configurations. The force output is measured with an Omega LC204-1K 4448 N (1000 lbf) capacity high accuracy miniature universal load cell. The position is measured with an RDP ACT8000C 40.6 cm (16 inch) travel linear variable differential transformer (LVDT) displacement transducer. An Omega FPD2003 0.114–26.5 l/min (0.03–7 gpm) range positive displacement flowmeter is used to measure the volumetric flowrate delivered to the whole muscle bundle. The pressure of each motor

unit is monitored with a Measurement Specialties MSP-300-250-P-4-N-3 1725 kPa (250 psi) pressure transducer.

Moog G761 62.5 l/min (16.5 gpm) rated flow four-way electrohydraulic servovalves were used to control the position of the cylinder and the pressures of the motor units. The B-ports on the motor unit valves were blocked because they are single acting actuators. Delta Computer Systems VC2124 two axis voltage-to-current converters were used to drive the valves. All data collection and control outputs were performed using a Quanser QPIDe board with a sampling rate of 1 kHz, and using the MATLAB/Simulink/GUIDE environments with Quanser QUARC real-time control software.

2.3.1 All recruitment levels at 965 kPa (140 psi)

Isobaric force-strain tests at a pressure of 965 kPa (140 psi) were performed for each recruitment level, and are shown in Figure 2.5. Other pressures were tested, but for brevity they are omitted since they follow the same trends shown in other McKibben muscle papers (i.e. linear dependence of blocking-force with pressure, nonlinear dependence of free-strain on pressure) [78]. The hysteresis increases with recruitment level, which is expected since there is more friction occurring with more active muscle fibers. The blocking-force approximately scales with recruitment level. Lastly, the free-strain remains effectively the same across all recruitment levels; this is also expected if they are fabricated with similar lengths and the inactive muscle fibers minimally impede the bundle's motion by buckling out of the way. This buckling phenomenon can be seen in its most extreme case (at the free-strain condition) for all recruitment levels in

Figure 2.6.

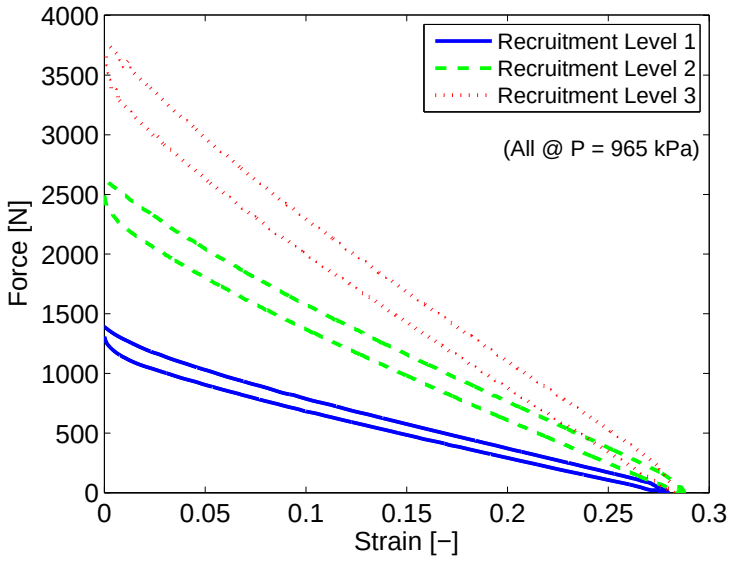

Figure 2.5: Force-strain curves of recruitment levels 1, 2, and 3 all at 965 kPa (140 psi).

Figure 2.6: Recruitment levels 1, 2, and 3 (from left to right) all at the free-strain condition at 965 kPa (140 psi), exhibiting buckling of the inactive motor units.

2.3.2 'Equivalent' force output recruitment level pressures

The ideal virtual work model predicts that force output should be directly proportional to applied pressure and the number of active McKibben muscles. Therefore, to generate the same force output at the same strain level, the pressure required by RL2 should be half that required by RL1, and the pressure required by RL3 should be one third that required by RL1. This was tested for two ideal 'equivalent' cases seen in Figure 2.7.

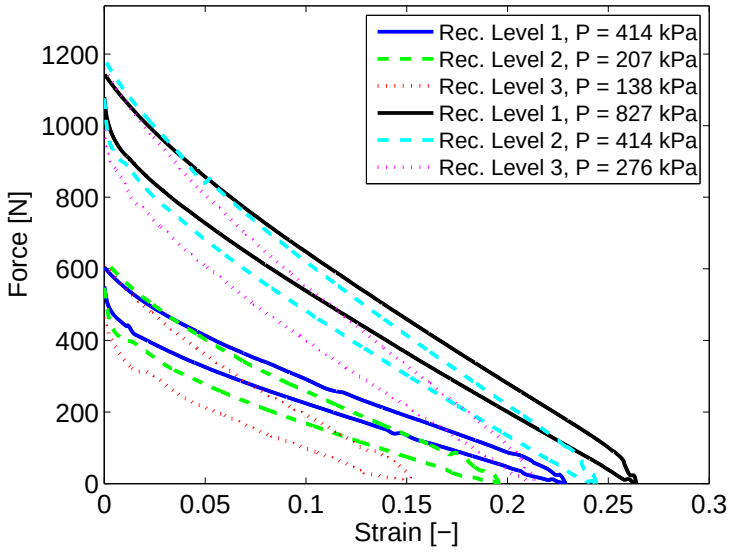

Figure 2.7: Force-strain curves of each recruitment level at pressures predicted by the ideal model to yield equivalent force output.

Close to the blocking-force, this assumption holds reasonably well, however the nonlinear strain dependence on pressure causes the large disagreement near the free-strain condition. This phenomenon is well known [78], but it was desired to determine how significant of an effect it had on recruitment thresholds in our operating pressure ranges. We also note that most friction models state that the friction is proportional to the applied pressure as well as contact area

[80]. In these tests, for each of the two 'equivalent' force output cases, the product of contact area and pressure remains the same, so the hysteresis loop width is expected to be unchanged. However it appears that increasing the contact area by recruiting more motor units has a greater affect on the friction than the pressure because the hysteresis loops appear widest for the RL3 curves. Clearly, more in-depth modeling is needed to give a reasonable representation of the pressures required to produce the same force output across different recruitment levels. This is essential in accurately determining recruitment thresholds and predicting the efficiency gains of variable recruitment, which motivates the models developed in the next section.

2.4 Muscle bundle modeling

2.4.1 Volume-based recruitment level effective initial braid angle

It is often assumed that FAMs sustain a cylindrical shape throughout their full contraction evolution [80, 15]; other groups also account for the slightly conical ends [82, 77, 31]. Previous work in the LIMS Lab at Cornell University experimentally observed the volume delivered over the full contraction range of the muscle, and found that the simple cylindrical model almost perfectly matches the data for the muscles used [45].

Since similarly sized muscles with the same Kevlar braid are utilized in this chapter, the model implemented also assumes the Kevlar fibers are flexi-

ble but inextensible, and the HAM maintains a cylindrical shape. The volume-contraction relationship of the HAM is governed by the mesh's geometry, and it is assumed that it follows the standard pantograph opening principle [78]. Employing these assumptions along with trigonometric identities, we obtain an equation for the volume of the muscle as a function of the current strain and its initial geometry

$$V = \pi r_0^2 l_0 \left[\frac{(1-\varepsilon)}{\sin^2(\alpha_0)} - \frac{(1-\varepsilon)^3}{\tan^2(\alpha_0)} \right], \tag{2.7}$$

where r_0 is the initial radius, l_0 is the initial resting length, α_0 is the initial angle the mesh fibers make with respect to the longitudinal axis of the muscle, and the strain is defined as $\varepsilon = (l_0 - l)/l_0$. We can subtract the initial volume from this to get an expression for the volume delivered to the muscle as it contracts from its initial condition,

$$\Delta V = \pi r_0^2 l_0 \left[\frac{(1-\varepsilon)}{\sin^2(\alpha_0)} - \frac{(1-\varepsilon)^3}{\tan^2(\alpha_0)} - 1 \right]. \tag{2.8}$$

It was desired to determine an effective initial braid angle for each recruitment level from measured volume delivered data as a function of strain. When determining the effective initial braid angle of each recruitment level, we assume that each active McKibben muscle fiber is operating with that initial braid angle, and that all muscle fibers have the same initial radius and length. This is how we account for the slight differences in length of each muscle fiber from the manufacturing process, and is also representative of how the bundle is operated. This recruitment level volume is given mathematically as

$$\Delta V_{RLi} = 2i \cdot \pi r_0^2 l_0 \left[\frac{(1-\varepsilon)}{\sin^2(\alpha_{0,RLi})} - \frac{(1-\varepsilon)^3}{\tan^2(\alpha_{0,RLi})} - 1 \right], \tag{2.9}$$

where i denotes the positive integer value of the current recruitment state, which for the present study is bounded to $i \in [1, 2, 3]$.

The effective initial braid angle for each recruitment level, $\alpha_{0,RLi}$, was determined by a least squares fit to experimentally measured volume evolution data (during contraction) as shown in Figure 2.8. The model seems to almost perfectly fit recruitment levels 1 and 2, and is also a good representation of recruitment level 3 with slight deviation near the free-strain condition. The values for the determined effective initial braid angles are included in this figure.

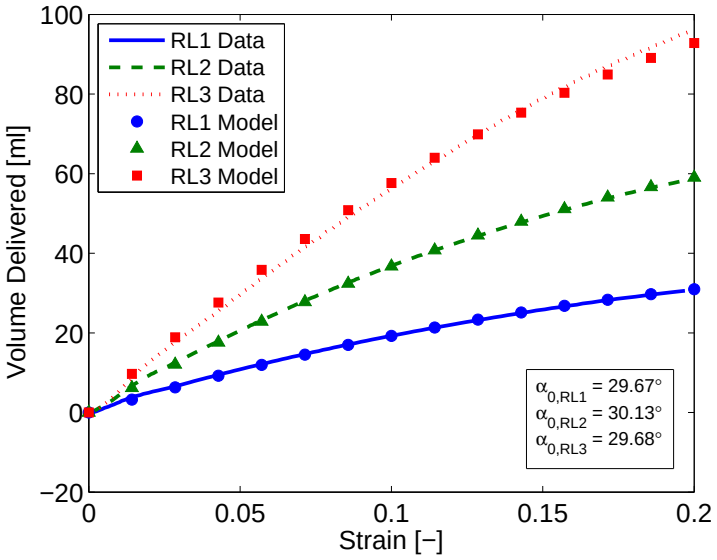

Figure 2.8: Experimental volume delivered versus strain of each recruitment level at 483 kPa (70 psi), and associated model using the fitted effective initial braid angle for each recruitment level.

2.4.2 Semi-empirical virtual work model

The force-strain model of the muscle bundle begins with the principle of virtual work, following the procedure given by Tondu [78]. This first assumes full transmission of the input fluid energy into mechanical output work, which can be written in terms of the force as

$$F = -P\frac{dV}{dl}, \tag{2.10}$$

where F is the force output, P is the pressure, V is the volume, and l is the length of the muscle. We then take the partial derivative of the volume model in Equation (2.7) with respect to strain, take the partial derivative of the length with respect to strain, employ the chain rule, and substitute back into Equation (2.10), which yields

$$F = \pi r_0^2 P\left[a\left(1-\varepsilon\right)^2 - b\right], \tag{2.11}$$

where a and b are geometric constants that are determined from the initial angle the mesh fibers make with the central axis, and are given by

$$a = \frac{3}{\tan^2\left(\alpha_0\right)}, \text{ and } b = \frac{1}{\sin^2\left(\alpha_0\right)}. \tag{2.12}$$

Here, we only consider the contraction portion of the hysteresis loops as this corresponds to when the muscles are performing positive work; this is all that is

needed when predicting the muscle's efficiencies. We account for the friction by simply multiplying the force equation by a force constant. We correct for elastic energy storage in the bladder by multiplying the strain by a pressure-dependent parameter as defined by Tondu [80] and used by other groups [34]. Including these yields the semi-empirical model

$$F = \kappa_F \pi r_0^2 P \left[a \left(1 - \kappa_\varepsilon \varepsilon\right)^2 - b \right], \tag{2.13}$$

where κ_F is the force constant, and κ_ε is the pressure-dependent strain tuning parameter defined as

$$\kappa_F = const., \text{ and } \kappa_\varepsilon = 1 + a_{\kappa\varepsilon} e^{-b_{\kappa\varepsilon} P}, \tag{2.14}$$

respectively, where $a_{\kappa\varepsilon}$ and $b_{\kappa\varepsilon}$ are constants.

Transforming this semi-empirical force model for each recruitment level in conjunction with the experimentally determined effective initial braid angles yields

$$F_{RLi} = 2i \cdot \kappa_{F,RLi} \pi r_0^2 P_{RLi} \left[a_{RLi} \left(1 - \kappa_{\varepsilon,RLi} \varepsilon\right)^2 - b_{RLi} \right]. \tag{2.15}$$

The tuning parameters for adjusting the force and strain were found for each recruitment level using least squares with the contraction data in Figure 2.7. The resulting model with its associated data is shown in Figure 2.9. While there is some deviation near the blocking-force condition, the semi-empirical model fits

reasonably well over all the recruitment levels and pressures, and is therefore acceptable for our purposes.

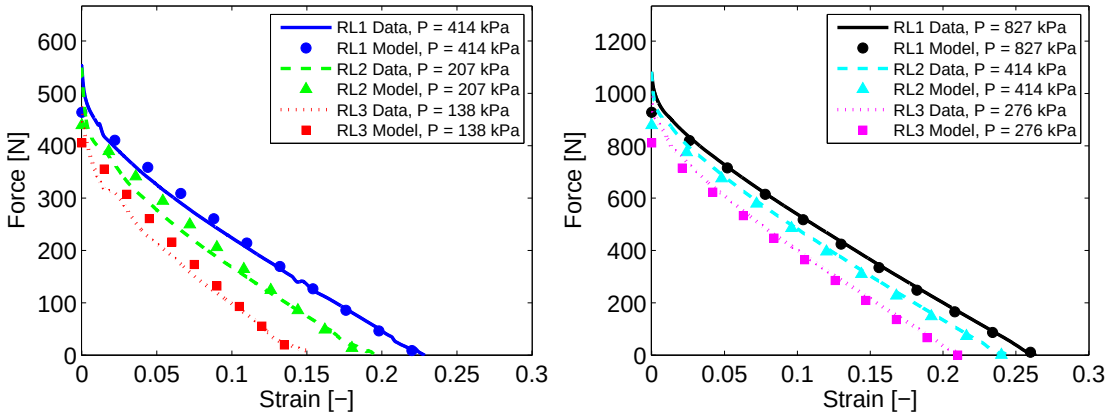

(a) (b)

Figure 2.9: Semi-empirical force-strain model and data for the contraction portion of Figure 2.7 across all recruitment levels and for (a) lower and (b) higher pressures.

2.4.3 Analytic investigation of variable recruitment

Using the developed models, we can predict the efficiency gains associated with the proposed variable recruitment actuation scheme. Two brief case studies are considered with the bundle in a vertical orientation simply lifting weight against gravity. The first case investigates the effect of varying the load on efficiency while lifting to the same strain, and is shown in Figure 2.10 (a). The loads range from 0 to 204 kg (0 to 450 lb), and are lifted from 0 to 5% strain. The second case examines the effect of varying the strain on efficiency while lifting a 102 kg (225 lb) load, and is presented in Figure 2.10 (b). The efficiency is computed by taking the ratio of the mechanical work output to the fluid energy input from the high pressure rail, given by

$$\eta_{total} = \frac{W_{mech,out}}{E_{fluid,in,S}} \times 100. \tag{2.16}$$

The mechanical work output is calculated by

$$W_{mech,out} = F l_0 \Delta\varepsilon, \tag{2.17}$$

where F is the force the muscle bundle is exerting to lift the attached load, l_0 is the initial length of the bundle, and $\Delta\varepsilon$ is the strain over which the muscle bundle produces the force. The fluid energy used is given by

$$E_{fluid,in,S} = P_S \Delta V_{RL,max}, \tag{2.18}$$

where $\Delta V_{RL,max}$ is the volume change corresponding to the maximum recruitment level utilized in reaching the target strain (calculated using Equation 2.9), and P_S is the supply pressure. Using these definitions, the efficiency as a function of load lifted for the variable recruitment bundle is calculated and plotted in Figure 2.10. In this simulation, it is assumed that the supply pressure is constant at 827 kPa (120 psi), and the recruitment thresholds occur when the pressure in the active motor unit(s) reach(es) this pressure. In practice, these thresholds would occur slightly lower than full supply pressure since this is the stalled condition.

The solid lines of Figure 2.10 (a) and (b) denote the path of highest efficiency; following this, the solid blue line corresponds to RL1, and when it's force output saturates (the muscle pressure reaches pump supply pressure), the bundle

upshifts to RL2 (denoted by the green solid line). When the force capacity of RL2 is exceeded, it upshifts to RL3 (indicated by the red solid line). The dotted lines show the efficiency if the bundle is used in RL2 (green) or RL3 (red) below the path of highest efficiency. These dotted lines can be accessed if a lower pressure is used as the recruitment threshold, therefore shifting the vertical portions of this plot to the left; this gives higher potential actuator velocities (due to the larger pressure drop), but yields lower efficiencies. The single equivalent muscle (SEM) with pure throttling control is included as a baseline of comparison. The SEM has the same characteristics as using the muscle bundle in its fully recruited state ($i = 3$) the entire time.

At low load conditions in Figure 2.10 (a), fewer motor units are needed to reach the target strain, therefore much less fluid energy is consumed resulting in higher efficiencies when compared to the SEM. The efficiency of the variable recruitment bundle eventually converges to that of the single equivalent muscle at the highest load conditions. A similar pattern is seen in Figure 2.10 (b) where higher efficiencies occur in the lower strain regions. These variable recruitment simulation results show promise for significant energy efficiency gains, and motivate the experimental implementation and testing of real-time variable recruitment on a robotic arm presented in the next section.

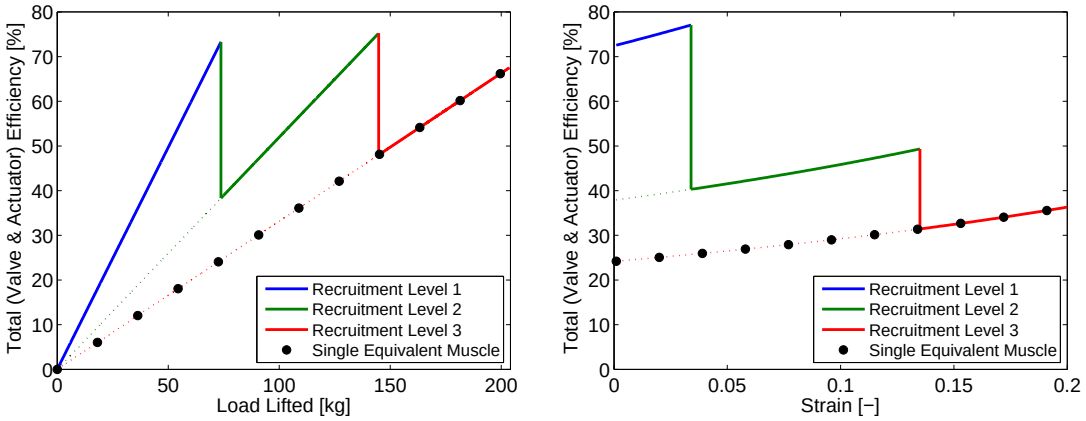

Figure 2.10: Semi-empirical model predicted (a) efficiency versus load lifted while contracting from 0 to 5% strain, and (b) efficiency versus strain while lifting 80 kg, for variable recruitment and a single equivalent muscle.

2.5 Variable recruitment robot arm apparatus and controller implementation

2.5.1 System definition

In order to directly measure the efficiency gains of online variable recruitment, experiments were conducted on a robot arm test rig, pictured in Figure 2.11. The hydraulic circuit and relevant sensors are diagrammed in Figure 2.12. The placement of the load cell and encoder on the arm for mechanical measurements is seen here. The locations where the fluid system is being monitored are also shown; the supply power used by the arm is measured with the supply pressure transducer and the supply flowmeter. The pressure in each motor unit is also measured and used in the controller which is discussed in depth in Chapter 2.5.3. All sensors and valves used on the robot arm setup are identical to the

ones employed on the linear dynamometer mentioned earlier in section 3, with the exception being that a 2500 count per revolution US Digital E6 kit optical encoder was used to measure the angle of the arm.

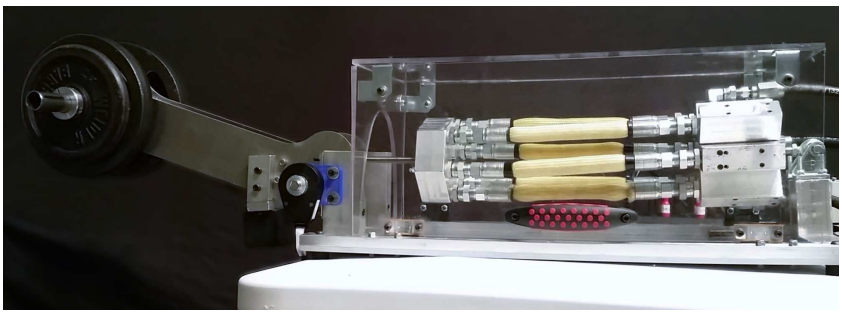

Figure 2.11: The variable recruitment robot arm experiment setup.

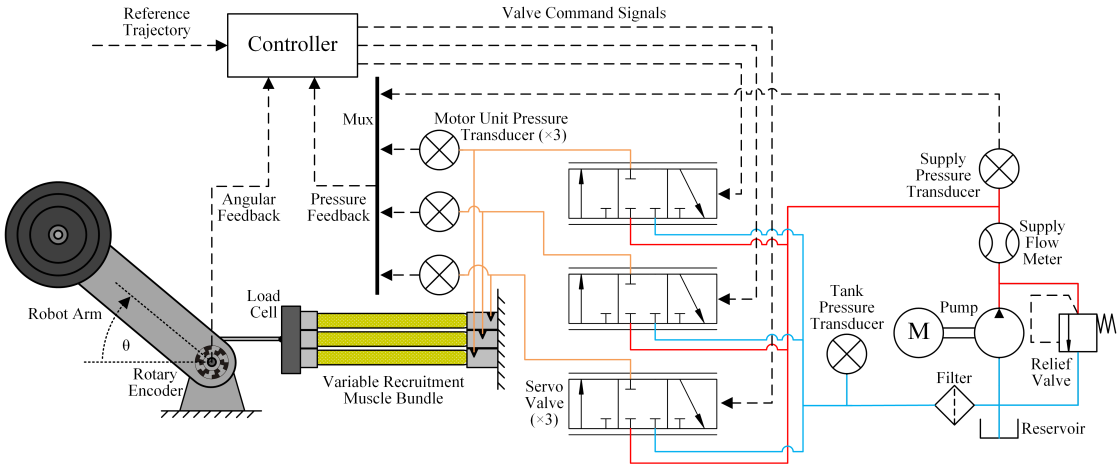

Figure 2.12: Diagram of the robot arm and hydraulic system (solid lines denote hydraulic transmission lines, dashed lines denote electrical signals).

2.5.2 Single equivalent muscle control

The single equivalent muscle was implemented by fluidically connecting all six of the McKibben muscles in the bundle to a single EHSV such that solely valve throttling was used for control. This way, the six HAMs would always remain active, which is equivalent to operating in RL3 at all times. The only difference is that one EHSV is used instead of three; valve flow rate limits did not hinder these tests as they were performed far below the rated maximum.

Closed loop angular position control was attained by using a simple proportional-integral controller. The error between the desired and measured angles was sent into the PI controller, which then output the commanded valve voltage, u_v. This delivers the appropriate pressure and flowrate of oil to track the reference trajectory. A separate set of PI gains were used for each loading scenario. These gains were chosen by following the Tyreus-Luyben tuning rules since the Ziegler-Nichols rules yielded excessive overshoot [83].

2.5.3 Online recruitment control strategy

For the variable recruitment control case, we use the same Tyreus-Luyben tuning rules to determine the PI gains, however the procedure is repeated for each recruitment level for each loading condition. This generates three sets of gains for each loading condition (instead of one set of gains as in the SEM case). The control of each recruitment level in this multiple-input single-output (MISO) system is handled by sending each active valve the same commanded voltage, while the inactive valve(s) are commanded to vent to the reservoir. A high level view of the system and controller is presented in Figure 2.13(a). The controller

uses the error in addition to the measured pressures of each motor unit and the supply line. These pressures are used in the state machine that determines the minimum necessary recruitment level in real-time, which will be discussed in Chapter 2.5.4.

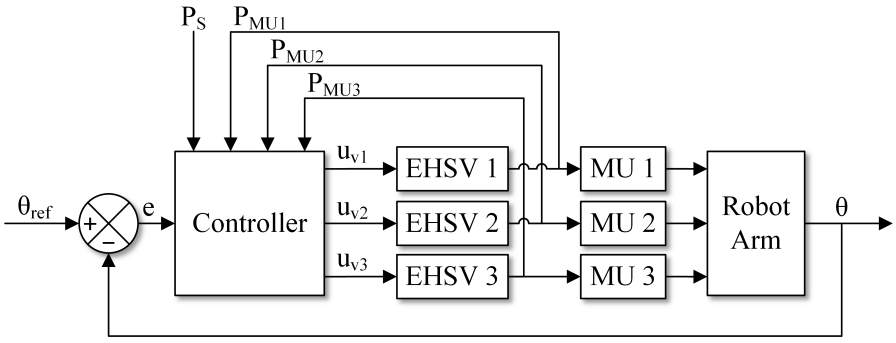

(a)

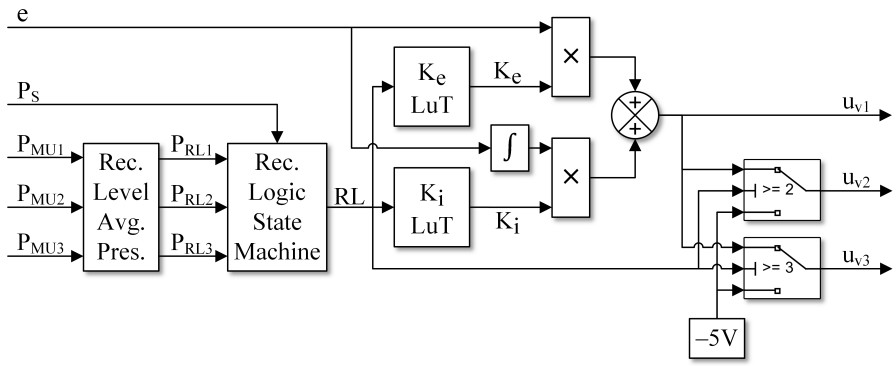

(b)

Figure 2.13: (a) High level block diagram of the MISO controller and plant, and (b) detailed block diagram of the controller.

The subsystem making up the controller block shown in Figure 2.13(a) is presented in more detail in Figure 2.13(b). As shown, the error is multiplied with the proportional gain lookup table (LuT) output, and the integral of the error is multiplied with the integral gain lookup table output. The results are summed to yield the commanded valve voltage output from the PI controller. The LuT blocks contain gains for each recruitment level, and the value used corresponds to the instantaneous output from the recruitment logic state machine. The state

machine determines what recruitment level to output based on an effective current recruitment level pressure and set of thresholds. This effective recruitment level pressure is obtained by simply averaging the measured pressures in the active motor units.

This architecture is a form of gain scheduling, but it is used here for the system's hybrid nature rather than compensating for continuous nonlinearities [63]. The switches on the right determine which servovalves to activate, also based on the current state machine output. Valve 1 is always active since RL1 is the lowest recruitment level (hence there is no switch for u_{v1}). If the system is in RL1, then valves 2 and 3 are inactive and therefore commanded –5V, corresponding to the venting condition. If the system is in RL2, then EHSV1 and EHSV2 are active and receive the same commanded output voltage from the PI controller, while EHSV3 is commanded –5V. Lastly, if the system is in RL3, then all three valves are active and are receiving the same commanded voltage from the PI controller. These switch conditions are summarized in Table 2.1.

Table 2.1: Servovalve commanded voltage with recruitment level.

RL	u_{v1}	u_{v2}	u_{v3}
1	PI_{RL1}	$-5V$	$-5V$
2	PI_{RL2}	PI_{RL2}	$-5V$
3	PI_{RL3}	PI_{RL3}	PI_{RL3}

2.5.4 Recruitment logic state machine

Determining the best way to switch recruitment levels is an important topic as this directly affects the energy savings and system performance. The recruitment logic state machine implementation is diagrammed in Figure 2.14(a). The default state is RL1 upon system startup. The system will be controlled with only EHSV1 and the PI gains associated with RL1. However once the pressure builds to greater than or equal to 90% of the supply pressure, a recruitment threshold is reached, and the recruitment state changes to RL2. At this moment, the PI gains change and valves 1 and 2 are both active. Once the system has reached RL2, two possibilities exist – it can either shift up to RL3 if the pressure becomes greater than or equal to 90% of supply pressure, or, it can shift down to RL1 if the pressure in RL2 drops to less than or equal to 40% of supply pressure. If the system is in RL3, it can only shift down to RL2 if the pressure drops to less than or equal to 53% of the supply pressure. This state machine was implemented in our Simulink-based controller via Stateflow.

These recruitment threshold values were picked for several reasons. Choosing 90% of supply pressure for the upshift thresholds allows for high efficiencies due to operating near full supply pressure, while still maintaining acceptable control authority; at 90% supply pressure, the servovalves still provide 32% of the maximum flow gain. The downshift thresholds were chosen such that the maximum corresponding pressure in the lower (post-shift) recruitment level is 80% of supply pressure. This was selected to introduce hysteresis into the state machine for the purpose of avoiding chatter around a recruitment threshold, hence preventing the system from rapidly switching back and forth between two recruitment levels. This built-in hysteresis technique is commonly used in

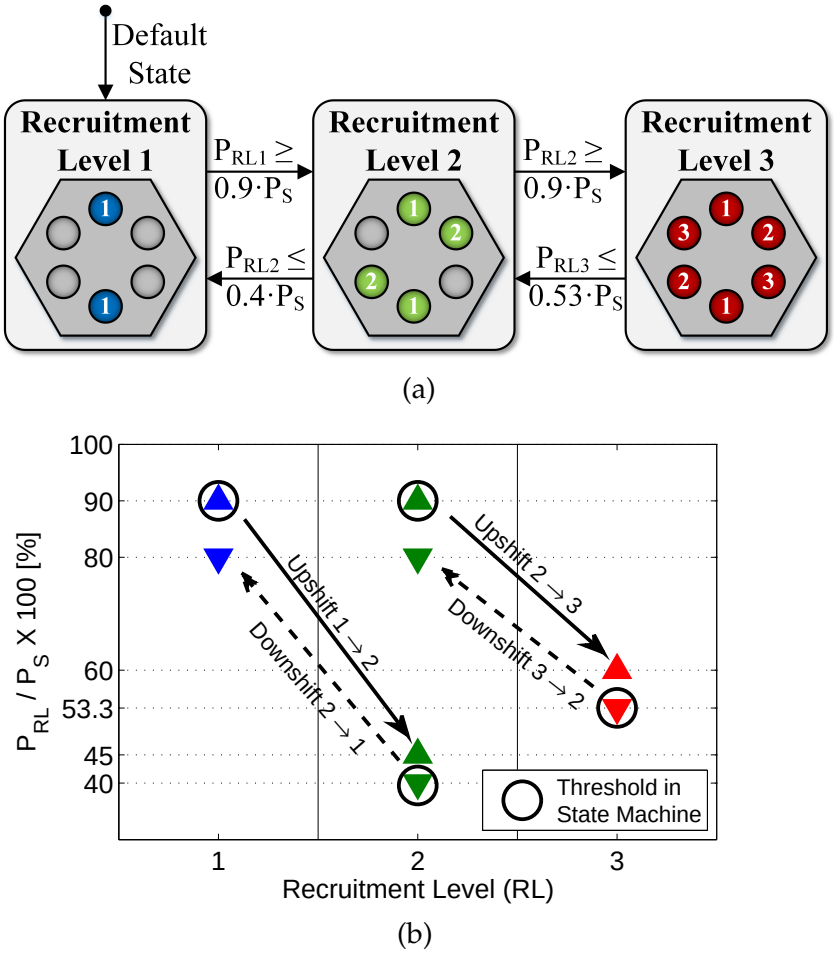

Figure 2.14: (a) Recruitment logic state machine, and (b) the associated pressure thresholds.

automotive automatic transmission controllers, but instead of pressure thresholds, throttle percent and engine speed are typically used [38, 5]. These recruitment threshold pressures are plotted in Figure 2.14(b). Upward pointing triangles and solid black arrows correspond to upshifts, while downward pointing triangles and dashed black arrows correspond to downshifts. The circled points are the thresholds used in the state machine in Figure 2.14(a), while the non-circled points are the ideal pressures that these thresholds map to in the new recruitment level (post-shift).

2.6 Variable recruitment experimental results

2.6.1 SEM and variable recruitment tests with real-time orderly recruitment

To compare variable recruitment to the single equivalent muscle baseline actuator, we first chose a fixed supply pressure of 827 kPa (120 psi) since this was able to lift the largest load to the maximum target angle. Both actuation approaches lifted five different amounts of weight ranging from 0–9.07 kg (0–20 lb) in 2.27 kg (5 lb) increments, from an angle of –25° to +5° with respect to the horizontal. These angles correspond to 4.4% to 14.6% strain in the muscle bundle. Although the arm lifts 9.07 kg (20 lb) at the highest loading condition tested, the muscle bundle experiences about 1157 N (260 lbf) of tension due to the lever arm geometry.

The experimental efficiencies were computed by taking the ratio of the measured mechanical work output to the measured fluid energy input from the high pressure rail. It is important to note that for this *total* efficiency, the fluid energy being measured is what is being taken from the high pressure rail supplied by the pump, therefore it only accounts for losses in the valves and actuators. This is used because this research is aimed at reducing this value. A true total system efficiency would start with the electrical power used by the pump, which is not considered here (the typical mobile hydraulic system efficiency of 10–20% reported in Chapter 2.1.2 uses this definition however). For the $W_{mech,out}$ in these calculations, only the portions when positive work occurs are included. On the other hand, the total fluid consumed is used in this calculation, including por-

tions when the muscle bundle is having work performed on it. Therefore, this efficiency also incorporates the effects of the controller on actuation efficiency. Hence, oscillations of the spool valve result in larger amounts of oil consumed and degraded efficiency.

The single equivalent muscle served as the baseline for comparison, and the five different loading conditions previously mentioned were tested. Once steady cyclic tracking of the $\frac{1}{4}$ Hz sinusoidal reference was attained (usually after about one to two full cycles), five full cycles were then saved. The positive mechanical work was computed and averaged over these five cycles (for $\dot{\theta} > 0$), and all of the fluid energy consumed was computed and averaged over these cycles as well. The calculation of efficiency follows Equation (2.16), with the mechanical work and fluid energy consumed defined as the time integral of the respective powers over the five cycles, given by

$$W_{mech,out} = \int_{t_0}^{t_f} FR\cos(\theta)\,\dot{\theta}dt, \text{ and} \tag{2.19}$$

$$E_{fluid,in,S} = \int_{t_0}^{t_f} P_S\,Q_S\,dt, \tag{2.20}$$

where t_0 is the initial time and t_f is the final time, R is the lever arm of the attachment point of the muscle bundle to the robot arm, F is the total measured force of the bundle, θ and $\dot{\theta}$ are the robot arm's measured joint angle and angular velocity, and P_S and Q_S are the measured supply pressure and flowrate.

The reference and measured arm angles for the SEM's median loading case of 4.54 kg (10 lb) are shown in the top of Figure 2.15(a). With simple PI control, the measured angle follows the reference reasonably well, just with a phase lag

of about 59°. This was sufficient for the purposes of the experiments, as we were primarily interested in studying the efficiency gains of online recruitment. Additionally, the associated mechanical power output and fluid power input are presented in the bottom of Figure 2.15(a); these are integrated with respect to time in Equations (2.19) and (2.20) and substituted into Equation (2.16) to yield the experimental efficiency values.

Implementing the developed variable recruitment controller, the same five load-lifting tasks were performed. At the 0 and 2.27 kg (0 and 5 lb) loads, no recruitment level shifting occurred because RL1 was able to reach +5° while staying below the 90% supply pressure upshift threshold. The 4.54 kg (10 lb) load required an upshift into RL2, and the 6.80 and 9.07 kg (15 and 20 lb) load conditions both needed to recruit RL3. The percent cycle time spent in each recruitment level during steady tracking is given in Table 2.2. It is pointed out that while the bundle begins in RL1 (its default state) at the start of each test, the 6.80 and 9.07 kg (15 and 20 lb) load cases only involve RL2 and RL3 during steady cyclic tracking.

In addition to determining the efficiency gains made by this variable recruitment actuation scheme, it was desired to see the effect of the recruitment level transitions on the controller's tracking abilities. Figure 2.15(b), 2.15(c), and 2.15(d) show the reference trajectory and measured arm angle, as well as the current recruitment level for the 4.54, 6.80, and 9.07 kg (10, 15, and 20 lb) loading cases respectively. These were the only cases that shifting occurred as the 0 and 2.27 kg (0 and 5lb) load cases only needed RL1 to reach the target angle and showed similar tracking to Figure 2.15(a).

Figure 2.15(b) shows reasonable tracking, but the shifts in recruitment level

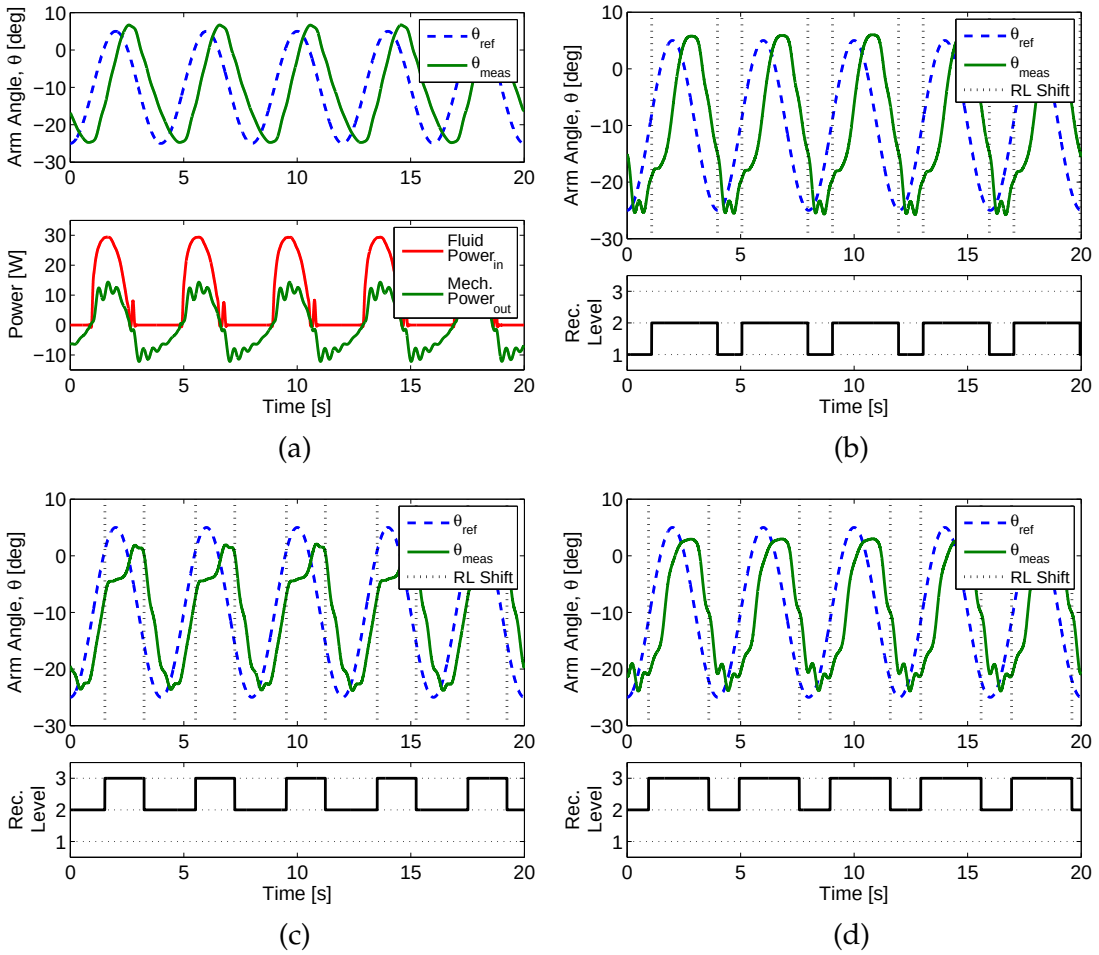

Figure 2.15: (a) Single equivalent muscle (all motor units active) arm angle tracking and the associated mechanical power output and fluid power input versus time lifting the median 4.54 kg (10 lb) load, and real-time variable recruitment arm angle tracking and current recruitment level versus time lifting the (b) 4.54 kg (10 lb) load, (c) 6.80 kg (15 lb) load, and (d) 9.07 kg (20 lb) load.

do have a clear negative impact in terms of error. Around 1 s, there is an upshift from RL1 to RL2. It can be seen that immediately following this upshift, the position of the arm lags even further behind the reference. This is because the previously inactive motor unit 2 needs to fill up with oil before it begins contributing to the overall force output demanded of RL2. At about 2 s MU2 catches

Table 2.2: Cycle time spent in each recruitment level for the five loading conditions.

	Cycle Time Spent In Each RL		
Load Lifted	RL1 (%)	RL2 (%)	RL3 (%)
0 kg (0 lb)	100	0	0
2.27 kg (5 lb)	100	0	0
4.54 kg (10 lb)	27	73	0
6.80 kg (15 lb)	0	57	43
9.07 kg (20 lb)	0	34	66

up and the tracking starts to behave more like Figure 2.15(a) again. At about 4 s, there is a downshift from RL2 to RL1. Immediately following this transition, the rate at which the arm angle falls increases slightly, and then at the bottom of the trajectory around –25° oscillations occur as the controller tries to compensate. This occurs because when switching from RL2 at 40% of supply pressure to RL1, the pressure in RL1 will likely be around this pressure as well (rather than the highest possible pressure of 80% of supply pressure shown in Figure 2.14(b)). However, a higher pressure is needed in RL1 for a smooth transition as discussed previously.

The 6.80 kg (15 lb) load case in Figure 2.15(c) shows the worst tracking out of all the cases with shifting. It shows similar issues with the up and downshifts as mentioned in the 4.54 kg (10 lb) case, but the upshift lag is dramatically worse. The reason for this is that the upshift from RL2 to RL3 occurs at a much higher angle, which corresponds to a much more contracted state of the bundle. This means that as soon as RL3 is entered, MU3 is in a largely buckled state and

requires even more oil volume to be delivered before it starts generating tension.

The 9.07 kg (20 lb) load case in Figure 2.15(d) shows better tracking than the 6.80 kg (15 lb) load even though it too is shifting between RL2 and RL3. This is because due to the higher load, it needs to shift to RL3 at a much lower strain value. The shift points occur at similar angles as the 4.54 kg (10 lb) load case, which is why the tracking looks similar to Figure 2.15(b), even though the shifts are occurring between different recruitment levels.

2.6.2 Efficiency discussion of the two actuation schemes

After performing all the robot arm tracking experiments lifting various loads, it is desired to quantify the efficiency gains for this variable recruitment actuation scheme. We use Equations (2.16), (2.19), and (2.20) to compute the experimental efficiencies for both the single equivalent muscle and variable recruitment configuration. The efficiency versus the load lifted is plotted for both cases in Figure 2.16. It is clear that at low loading conditions, variable recruitment yields much higher efficiencies than the single equivalent muscle case. In RL1 we would expect efficiencies to be three times that of the single equivalent muscle, in RL2, we would expect efficiencies to be 1.5 times that of the SEM, and in RL3 we would expect the efficiencies to be the same; this trend is exhibited by the data.

We can develop a simple model to predict the efficiency of each recruitment level at each loading scenario. First, we look at the mechanical work done by the muscle bundle. Due to the geometry of the robot arm, the force that the muscle bundle must generate to lift the robot arm and load is essentially constant throughout the range of motion. Assuming this, we can write the mechanical

work performed using Equation (2.17) but in terms of the angular displacement of the arm as

$$W_{mech,out} = FR\left(\sin(\theta_2) - \sin(\theta_1)\right), \tag{2.21}$$

where F is the force the muscle bundle is producing based on the geometry of the arm, R is the lever arm of the robot arm, and θ_1 and θ_2 correspond to the initial and final angles the robot arm is swept through (–25° and +5° respectively). The fluid energy used is given by Equation (2.18), where $\Delta V_{RL,max}$ is the volume delivered corresponding to the maximum recruitment level used in a given test, and P_S is the supply pressure assumed to be constant at 827 kPa (120 psi). The volume delivered is computed using Equation (2.9), where the maximum required recruitment level for that test, i, is determined based on the semi-empirical force model in Equation (2.15) in conjunction with the current load lifted, maximum target angle, and 90% supply pressure upshift threshold. Under this definition, for the SEM, $i = 3$. We substitute these work and energy values into the total efficiency expression given in Equation (2.16), and this model along with the aforementioned data is plotted in Figure 2.16. This simple model adequately predicts the efficiency gains of variable recruitment. There are a few points where the efficiency is over-predicted by the model – this can be best explained by poor controller tracking and oscillations. This results in additional expended oil with negligible increase in mechanical work done. For the points where the data exceeds efficiency predictions, the pump supply pressure would drop by about 10% at peak flow conditions, resulting in less fluid energy delivered than our assumed constant supply pressure in the efficiency equation, leading to higher experimental efficiencies.

The solid blue, green, and red lines denote the path of highest efficiency. The vertical portions occur when the bundle can't reach the +5° target angle and must transition to the next recruitment level, resulting in the sawtooth-like pattern from these discrete transitions. These vertical portions are set by the recruitment thresholds in the state machine, and therefore can be moved to the left or right in the plot. If we slide it to the right by increasing the recruitment threshold pressures, then even higher efficiencies can be attained since we stay in lower recruitment levels longer. If we slide it to the left, lower efficiencies result, but since this corresponds to a greater ΔP, the valves can provide more flow resulting in higher possible actuator velocities. This sheds light onto the fact that there is a trade-off between efficiency and performance, which is much like the automatic transmission gear shift analogy.

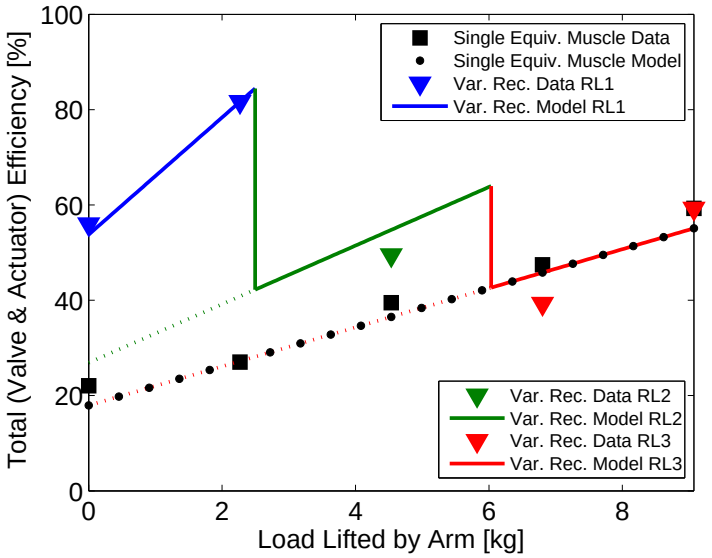

Figure 2.16: Experiment and model of efficiency versus load lifted for variable recruitment and a single equivalent muscle.

2.7 Discussion

Averaging the variable recruitment efficiency over the full range of loads tested yields an average efficiency of 57%, while doing the same calculation for the single equivalent muscle produces an average efficiency of 39%. That's a difference in efficiency of 18% (46% increase) in efficiency. Comparing this to the prediction given in Figure 2.4, one motor unit was expected to yield 50% efficiency, while 3 motor units was expected to give 69.4%, which is a difference of 19.4% (38.8% increase). The experimental efficiencies were lower overall due to the fact that the transduction efficiency was neglected in this theoretical plot, but the theory reasonably predicted the improvement (difference) in efficiency due to variable recruitment.

In developing the controller for these tests, simple hysteretic pressure thresholds were used in a state machine to trigger the discrete recruitment level shifting events. This was effective from an efficiency and chatter standpoint, but this simple strategy resulted in some additional error and lag at high strain shifts due to the buckled state of the newly activated motor unit. While operating near the supply pressure maximizes efficiency, it also marks a reduction in control authority as the flow gain is significantly reduced at higher pressures [47]. More advanced and nonlinear control techniques may need to be employed for the muscle bundle to work well across all operating regimes. Incorporating model-predicted pressures for equivalent force output between recruitment levels into future versions of the controller could also help smooth out the transitions at recruitment thresholds.

Lastly, in the development of a high efficiency untethered robotic system

with variable recruitment, we would select an appropriately sized load-sensing variable displacement pump. This would allow matching of the overall pressure and flow demands of the system, which would greatly reduce the quiescent flow losses of fixed displacement pumps as well.

2.8 Conclusions

This chapter first presented the development of a bioinspired variable recruitment hydraulic McKibben muscle bundle. Design considerations were made in the bundling hex manifold to fluidically connect the appropriate pairs of McKibben muscles to serve as motor units, producing axis-symmetric force about the full bundle's attachment point. The quasi-static force-stroke behavior was then investigated, and a model for each recruitment level was developed. In this model, fluid volume delivered data was used in determining an effective initial braid angle of each recruitment level, where the active muscle fibers were assumed to have identical geometries. Empirical tuning parameters were employed to account for friction and elastic energy storage, and this model predicted significant efficiency gains with a variable recruitment actuation scheme

A real-time selective recruitment controller for a hydraulic artificial muscle bundle was reported and implemented for the first time. This utilized a recruitment logic state machine that selected the current recruitment level based on measured pressures and a pressure threshold schedule. These thresholds were chosen such that high efficiencies would be attained, while retaining sufficient control authority. Additionally, hysteresis was built into the thresholds to prevent rapid switching between recruitment levels. A lookup table was used to

provide different sets of PI gains depending on the selected recruitment level, while this recruitment level also determined which servovalves were active and received the PI controller's commanded voltage.

This real-time recruitment controller was tested on a single degree-of-freedom robot arm, where efficiency was measured over five different loading conditions. This data was compared to a single equivalent muscle case where only throttling was used to control the system. As predicted by our model, variable recruitment was shown to significantly improve efficiency in the low load regions. When the highest recruitment state is required, the efficiency converges to the single equivalent muscle case. Over the load ranges tested, variable recruitment increased the average efficiency by 46% (difference of 18%) compared to the single equivalent muscle case.

More advanced model-predictive and nonlinear control techniques are suggested to better the trajectory tracking during transitions between recruitment levels. Additionally, refinements to the technical design including improvements to mitigate buckling in inactive elements and more compact packaging of the actuators and valves are needed to facilitate applications. Finally, optimization of a variable recruitment actuation system for an application like a mobile robot will need to balance trade-offs between maximizing energy efficiency and ensuring adequate actuator bandwidth, tracking performance, and speed.

This chapter originally appeared as:

Michael Meller, Jordan Chipka, Alexander Volkov, Matthew Bryant, and Ephrahim Garcia. Improving actuation efficiency through variable recruitment hydraulic McKibben muscles: modeling, orderly recruitment control, and experiments. *Bioinspiration & Biomimetics*, 11(6):065004, 2016.

CHAPTER 3

MODEL-BASED FEEDFORWARD AND CASCADE CONTROL OF HYDRAULIC MCKIBBEN MUSCLES

3.1 Introduction

McKibben muscles are most commonly used in anthropomorphic robots [69, 79, 26, 12] and assistive devices [25, 93, 56]. Their high force and power densities, low fabrication cost, skeletal muscle-like performance, and scalability make them appealing for use in such systems [78]. In their original form, McKibben muscles are made up of an elastomeric tube that is inserted into a helically woven mesh [15]. The mesh is typically braided with a bias angle (with respect to the central axis) less than the neutral angle of 54.7°, thereby allowing it to expand radially and contract axially; while it is not nearly as common, extensile operation is also possible if the bias angle of the weave is greater than the neutral angle [28]. One end of the actuator is plugged while the other end connects to the fluid power supply. Pressurization of the McKibben muscle via the fluid port causes contraction and/or tension depending on the load. Since these actuators are single-acting, either an antagonistic pair or a restoring force is required to achieve bi-directional motion.

While nearly all McKibben muscles are operated pneumatically (hence the moniker pneumatic artificial muscle (PAM)), other means of actuation have been explored. Takashima *et al.* impregnated the McKibben mesh with a shape memory polymer so that the muscle can hold a fixed position without the need for continuous control [75]. Sangian *et al.* developed thermally activated, paraffin filled McKibben muscles to eliminate the need for a bulky prime mover [65].

Ball *et al.* replaced the braided mesh of McKibben muscles with a tubular-knit sleeve to attain more skeletal muscle-like force-stroke profiles with free contractions of over 50% [8]. Recently, variable recruitment of parallel McKibben muscles has gained popularity as a way to increase energy efficiency [10, 62, 22, 44]. Several research groups have utilized hydraulic (oil or water) actuation for the higher possible efficiency and stiffness [27, 51, 77, 45, 66, 92].

There has been significant controller development for pneumatically actuated McKibben muscles [93, 56, 14, 80, 16, 67, 40, 30, 11, 48, 20, 89], however there has been very little control system consideration for hydraulic artificial muscles (HAMs) [92, 44]. This chapter investigates the angular position control system development for a robotic arm actuated with hydraulic McKibben muscles lifting a fixed load. The primary objective was to achieve good angular position tracking over a range of frequencies up to 1 Hz, which is similar to what is experienced in anthropomorphic robotic and orthotic applications. Simpler control architectures were emphasized, therefore only augmentations to classical control techniques were employed. All controllers were experimentally assessed by performing angular position frequency and step response experiments.

3.2 System definition

The hydraulic McKibben muscle controllers were developed for the robotic arm testbed pictured in Figure 3.1. The arm can lift a variety of loads, but 4.54 kg (10 lb) was used throughout the experiments presented in this chapter. A 4.54 kg (10 lb) load results in approximately a 578 N (130 lbf) static tension on the

muscles due to the geometry of the arm.

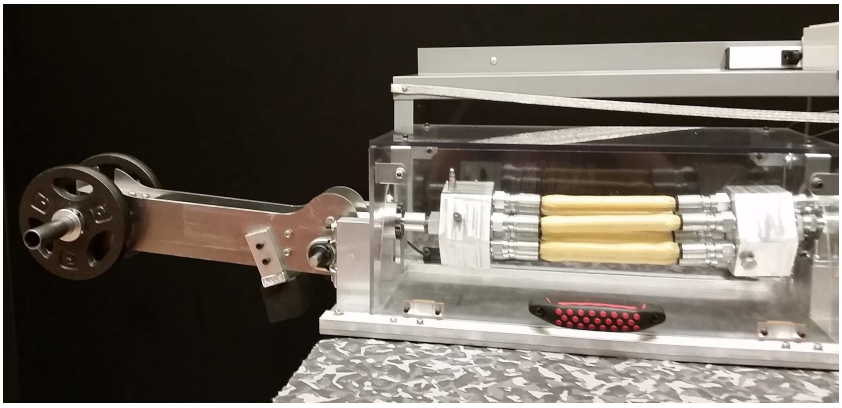

Figure 3.1: The robot arm experimental test rig.

Six parallel hydraulic McKibben muscles actuate the arm. These were fabricated using a silicone bladder with an inner diameter of 9.53 mm (3/8 in), an outer diameter of 12.7 mm (1/2 in), and a shore hardness of 35 A. This bladder was chosen for its hydraulic oil compatibility, as well as its relatively low shore value so as to minimize elastic energy storage. A Kevlar braided mesh with an expansion range of 12.7 mm (1/2 in) to 22.2 mm (7/8 in) in diameter was used; Kevlar was chosen over the more common polyethylene or nylon due to its more durable fibers. These components are held together with Eaton Weatherhead 06Z-R06 steel o-ring boss swivel crimp fittings. Each HAM has a 17.78 cm (7 in) active length, measured between the inside edge of the end fittings.

All six HAMs are fluidically connected to one Moog G761 62.5 Lpm (16.5 gpm) rated flow four-way electrohydraulic servovalve (EHSV). A Delta Computer Systems VC2124 two axis voltage-to-current converter powered the valve. Since the HAMs are single-acting and used in a gravity-return configuration, the servovalve B-port was plugged. The pressure of all six HAMs is monitored with one Measurement Specialties MSP-300-250-P-4-N-3 17.24 bar (250 psi) pressure

transducer. A 2500 count per revolution US Digital E6 kit optical encoder measured the angle of the arm. Data acquisition and control commands were carried out on a Quanser QPIDe I/O board with a sampling rate of 1 kHz, using the MATLAB/Simulink environments and Quanser QUARC real-time control software. A diagram of the robot arm, McKibben muscles, hydraulic circuit, and sensing and control elements are shown in Figure 3.2.

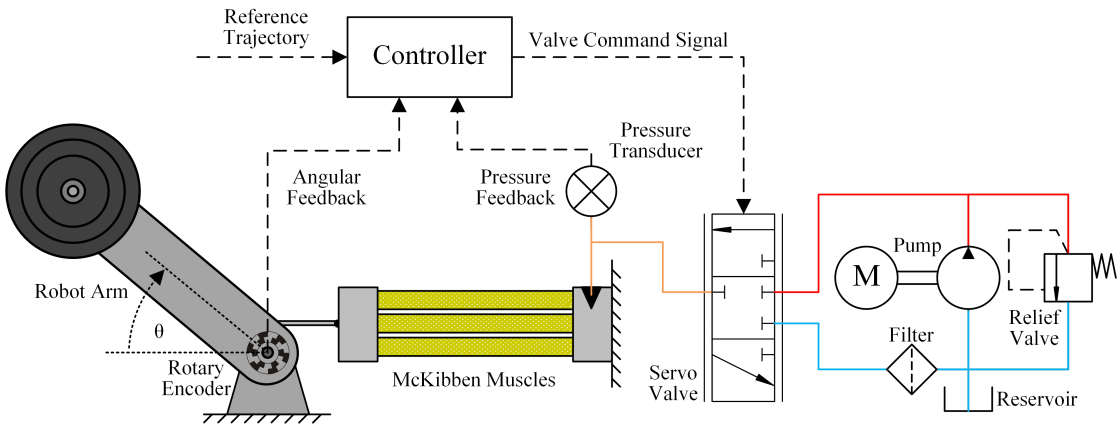

Figure 3.2: Schematic of the whole system including the robot arm, McKibben muscles, hydraulic system, and sensing and control.

3.3 Controller development

Many research groups have investigated control system development for pneumatic artificial muscles, however very few performed feedback control with HAMs. Before beginning our controller development, a brief survey of existing controllers for McKibben muscles and traditional hydraulics was carried out, and is presented in Table 3.1. PAM control system development ranges from simple classical control techniques such as PI and PID [20, 92], to adding dead

time compensation [89] and cascaded loops [67, 48, 62], to adaptive [14] and nonlinear control [80]. Xiang *et al.* used PID to control their water and air valves supplying their combined hydraulic/pneumatic McKibben muscle. While variable recruitment was the focus of the work, Meller *et al.* used PI-control for their oil-filled McKibben muscles. Traditional hydraulic cylinder control usually stems from classical control schemes [70, 33, 42, 52], often augmented with feedforward (ff) [33, 52].

Table 3.1: Survey of existing controllers for McKibben muscles and traditional hydraulics.

Author(s)	Actuator	Fluid	Sensing Req'd	Controller
This work	McKibben	Oil	Angle, pressure	Cascaded PI-P w/ ff
Meller *et al.* [44]	McKibben	Oil	Angle	PI
Xiang *et al.* [92]	McKibben	Water/air	Angle	PID
Woods *et al.* [89]	McKibben	Air	Angle	P w/ dead time comp.
Tondu *et al.* [80]	McKibben	Air	Angle	Sliding mode
Robinson *et al.* [62]	McKibben	Air	Angle, pressure	Cascaded PI-PI
Vo Minh *et al.* [48]	McKibben	Air	Position, pressure	Cascaded PI-PI w/ hysteresis ff
Caldwell *et al.* [14]	McKibben	Air	Angle	Adaptive linear
Schröder *et al.* [67]	McKibben	Air	Angle, torque	Cascaded PI-PI
De Volder *et al.* [20]	McKibben	Air	Position	PI
Manring [42]	Cylinder	Oil	Position	PI
Vickers [70]	Cylinder	Oil	Position	PID
Nachtwey [52]	Cylinder	Oil	Position	PID w/ vel. (and accel.) ff
Johnson [33]	Cylinder	Oil	Position	PIV w/ vel. (and accel.) ff
Sohl *et al.* [72]	Cylinder	Oil	Position, pressure	Feedback linearization

We consider three different controllers for our hydraulic McKibben muscle-actuated robotic arm. These angular position tracking control laws determine the commanded voltage to the electrohydraulic servovalve throttling the fluid power to and from the McKibben muscles. It was desired to attain acceptable

tracking over a range of frequencies up to 1 Hz since this is a common frequency range in human motion [50], and therefore anthropomorphic robots and assistive devices. Another goal was to keep the control architectures reasonably simple by only making improvements to classical control techniques.

3.3.1 PI-control

The first closed loop angular position controller tested, serving as the baseline of comparison, is a classical proportional-integral (PI) controller. The error between the desired (θ_d) and measured (θ) angles was sent into the PI-controller, which then output the commanded valve voltage, u_v. A block diagram representation of this is given in Figure 3.3. This attempts to deliver the pressure and flowrate of oil required to track the reference trajectory. PI-control was chosen as the baseline because it has shown to be the simplest useful control technique spanning both PAMs and hydraulics [20, 44, 33, 42]. Additionally, including a derivative term typically adds little to no performance enhancement in electro-hydraulic servo-systems [33]. The gains were chosen in hardware by following the Tyreus-Luyben tuning rules [83].

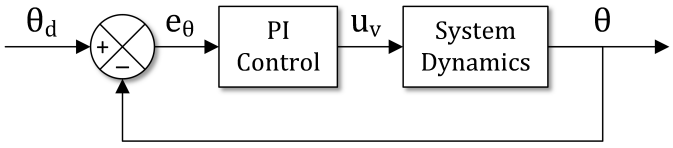

Figure 3.3: Block diagram for PI-control.

3.3.2 PI-control with model-based feedforward

The second control architecture developed adds a feedforward term to the baseline PI-controller. While feedforward can be utilized to minimize the effects of known disturbances, it can also provide anticipative actions in tracking applications, which is how it is used it in this work [71].

In the traditional hydraulic control methods that use feedforward in Table 3.1, the most commonly implemented form consists of a gain multiplied with the time derivative of the position reference signal [33, 52]. This method is used primarily for reducing following error, and is often presented as an additional gain to tune where the user blindly increases the gain while performing ramp commands until this error is minimized. Fortunately this gain is a forgiving parameter to tune and it does not affect loop stability [33].

Upon further investigation, a simple feedforward gain multiplied with the time derivative of the position reference signal likely works so well in hydraulic cylinder control because in steady conditions, the flowrate out of the valve is directly proportional to the commanded voltage, and the flowrate demands are directly proportional to the velocity of the cylinder; hence all of this information can be lumped into one gain. It was desired to use a similar feedforward methodology to reduce the following error in this work. Since McKibben muscles are highly nonlinear and their flowrate is dependent on both position and velocity (whereas cylinder flowrate is only a function of velocity), we decoupled the typical feedforward gain into a nonlinear predicted volumetric flowrate model of the McKibben muscles and a linear flow gain of the EHSV.

The volumetric flowrate demands of the McKibben muscles were modeled

following common assumptions that the HAMs maintain a cylindrical shape throughout contraction, the Kevlar fibers are inextensible but flexible, and the Kevlar mesh follows the pantograph opening principle [78]. For simplicity, we also assume that all six parallel McKibben muscles are manufactured identically so the volume equation is multiplied by a factor of six. Taking all this into account yields an equation for the volume of the HAMs as a function of the current stroke and initial geometry

$$V_m = 6 \cdot \pi r_0^2 \left[\frac{(l_0 - x)}{\sin^2(\alpha_0)} - \frac{(l_0 - x)^3}{l_0^2 \tan^2(\alpha_0)} \right], \tag{3.1}$$

where r_0 is the initial radius, l_0 is the initial resting length, α_0 is the initial angle the mesh fibers make with respect to the longitudinal axis of the muscle, and the stroke is defined as

$$x = l_0 - l = R\left(\sin(\theta) - \sin(\theta_0)\right), \tag{3.2}$$

where l is the current length of the HAMs, R is the distance between the attachment point of the McKibbens and the robot arm "elbow" joint, θ is the angle the robot arm makes with respect to the horizontal, and θ_0 is the initial arm angle when the HAMs are at their initial longest length. Taking the time derivatives of Equations (3.1) and (3.2) and substituting yields the volumetric flowrate model of the McKibben muscles

$$Q_m = 6 \cdot \pi r_0^2 \dot{x} \left[\frac{3\,(l_0 - x)^2}{l_0^2 \tan^2(\alpha_0)} - \frac{1}{\sin^2(\alpha_0)} \right]. \tag{3.3}$$

In developing a model of the EHSV, we first assume that the dynamics of the torque motor and flapper are fast enough to be negligible, hence the commanded valve voltage is directly proportional to the spool position. Others have made this assumption as well [42, 72]. This is a reasonable assumption since the maximum closed-loop frequency tested is 1 Hz and previous testing of this EHSV when piloted at 17.24 bar (250 psi) yielded a bandwidth of 10 Hz (normally 40 Hz when piloted at 207 bar (3000 psi) [49]). While the pilot pressure is 17.24 bar (250 psi), the supply pressure to the main stage of the valve (to the McKibben muscles) is 7.6 bar (110 psi); this allows for improved valve performance while minimizing the risk of the McKibben muscles bursting. We also assume that the valve has a critically centered lap condition with square port geometry (based on the valve datasheet [49], and validated in Figure 3.7 (a) of Chapter 3.4.2), and that the flow obeys the orifice equation, which gives

$$Q_v = \begin{cases} c_v u_v \sqrt{P_S - P_m} & \text{for } u_v > 0 \\ 0 & \text{for } u_v = 0, \\ -c_v u_v \sqrt{P_m - P_T} & \text{for } u_v < 0 \end{cases} \tag{3.4}$$

where c_v is the valve orifice coefficient, P_S is the pump supply pressure, P_m is the pressure in the McKibben muscles, and P_T is the tank pressure [47, 42, 72].

In order to estimate the flowrate through the valve at a given voltage applied, without the need for updating estimates or measurements of the system pressures, a linearization about the null conditions was used; this is when the valve spool is centered, there is no flow, the tank pressure is assumed to be zero for simplicity, and the actuator pressure is assumed to be one half the supply pressure. In taking the Taylor series expansion for the linearization, we must

take the partial derivatives of Equation (3.4) with respect to the valve voltage and muscle pressure. For critically centered valves, we know that the partial derivative of Equation (3.4) with respect to the muscle pressure evaluated at the null condition is zero, hence we only need to consider the partial derivative of Equation (3.4) with respect to the valve voltage, which is also known as the flow gain [47, 42]

$$K_{q0} = \left.\frac{\partial Q_v}{\partial u_v}\right|_0 = c_v \sqrt{\frac{1}{2} P_S}. \tag{3.5}$$

Hence, the linearized flow equation is given by

$$Q_{v,lin} \approx K_{q0} u_v. \tag{3.6}$$

If we assume that the compressibility and pressure dynamics of the fluid are negligible, then we can state that the linearized valve flow in Equation (3.6) must equal the volumetric flowrate into the muscle given in Equation (3.3). Rearranging this equation for the commanded valve voltage yields the feedforward term in our control law

$$u_{ff} = Q_m(\theta_d, \dot{\theta}_d)/K_{q0}. \tag{3.7}$$

Assuming negligible pressure dynamics is reasonable since our load dynamics are on the order of one second while the pressure dynamics are typically on the order of milliseconds [42]. This feedforward term in Equation (3.7) is shown

in the block diagram representing the overall combined feedforward/feedback control law in Figure 3.4.

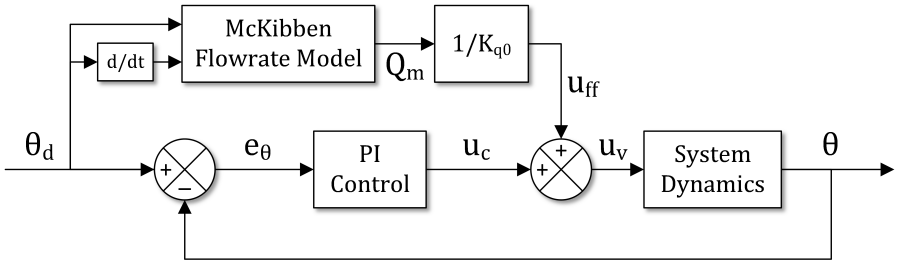

Figure 3.4: Block diagram for PI-control with model-based feedforward.

3.3.3 Cascaded PI-P-control with model-based feedforward

Several groups have implemented a cascaded PI-PI architecture when controlling PAMs [67, 48, 62]. Cascade control has the added benefit of improved disturbance rejection to the primary controlled variable; however, it requires the addition of a sensor to measure another variable, and that the inner loop dynamics are much faster than the outer loop dynamics [43]. The last scheme implemented in this chapter adds an inner control loop with pressure feedback to the second developed architecture from Figure 3.4. The outer PI-control loop is for angular positioning; instead of its output being the feedback controller portion of the commanded valve voltage as in Chapter 3.3.2, its output is now the pressure reference for the inner secondary loop. The inner proportional (P) control loop tracks the desired pressure set by the outer loop. P-control was chosen over PI-control to avoid potential competing dynamics of the cascaded loops, and the integral action of the outer loop is sufficient for eliminating steady-state error of the arm angle. The gain tuning process began with the inner loop as

suggested in Marlin's book [43]. The proportional gain was chosen to be the inverse of the valve's pressure sensitivity. Then the inner loop was fixed and treated as if it were part of the plant, and the outer loop was tuned as described in Chapter 3.3.1. The block diagram representing this control scheme is shown in Figure 3.5.

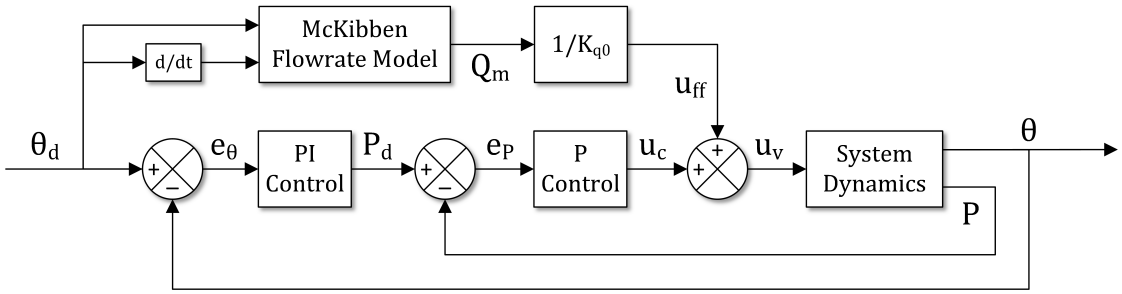

Figure 3.5: Block diagram for cascaded PI-P-control with model-based feedforward.

3.4 Parameter identification for feedforward compensation

3.4.1 Effective initial braid angle of the parallel McKibben muscles

In Chapter 3.3.2, the developed feedforward term is heavily dependent on the initial braid angle of the six parallel McKibben muscles. Hence, it was desired to obtain an accurate estimate of the effective initial braid angle from experimental data. The procedure for determining this involved measuring the volume of oil delivered to the McKibben muscles as a function of robot arm angle. An Omega FPD2003 0.114-26.5 Lpm (0.03-7 gpm) range positive displacement flowmeter

measured the volume delivered, while the aforementioned encoder measured the arm angle. As stated previously, we assume that each McKibben muscle is fabricated identically and therefore all six HAMs are operating with the same effective initial braid angle. We can subtract the initial volume from Equation (3.1) to get an expression for the volume delivered to the muscles as the arm contracts from its initial condition, given as

$$\Delta V_m = 6 \cdot \pi r_0^2 \left[\frac{(l_0 - x)}{\sin^2(\alpha_0)} - \frac{(l_0 - x)^3}{l_0^2 \tan^2(\alpha_0)} - l_0 \right]. \tag{3.8}$$

To get Equation (3.8) in terms of robot arm angle, Equation (3.2) is substituted; using this result and experimental data, a least squares fit was performed to obtain the effective initial braid angle of 29.7°. The model and experimental data is plotted in Figure 3.6 showing good agreement.

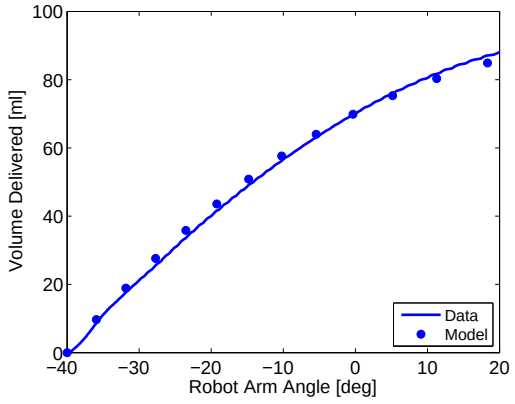

Figure 3.6: Volume of oil delivered as a function of robot arm angle for the six parallel McKibben muscles and the associated model for identification of the effective initial braid angle.

3.4.2 Electrohydraulic servovalve flow gain

In most applications, a reasonable estimate of the flow gain can be made from an EHSV's datasheet and using Equation (3.5). However, we are running the valves at pressures about 3.7% of normal operating conditions, and our EHSV can allow more flowrate than our pump can supply. Therefore in order to obtain a more accurate representation of the flow gain of our combined valve-pump system, several tests were performed. First, the A and B ports of the valve were connected directly. The same Omega FPD2003 flowmeter measured the volumetric flowrate supplied to the valve. The commanded valve voltage was sinusoidally cycled from -10 to 10 V at 0.25 Hz for five different supply pressures, ranging from 3.45 bar (50 psi) to 17.24 bar (250 psi) in 3.45 bar (50 psi) increments.

Figure 3.7 (a) shows the EHSV no-load flowrate as a function of the commanded valve voltage for a supply pressure of 17.24 bar (250 psi). This plot is included for two reasons: 1) to show that the assumption of a critically centered lap condition in the valve spool is reasonable, marked by the minimal deadband exhibited around the null condition, and 2) to demonstrate how the flow gain at a given pressure is determined by taking the average voltage at ± 40% of the saturation flowrate and finding the slope between these two points, shown as the red dots and red dashed line respectively [3]. The flow gain found from Figure 3.7 (a) yields the far right data point in Figure 3.7 (b). Figure 3.7 (b) shows the other pressures tested as well as the model of the flow gain as a function of supply pressure using Equation (3.5). A least squares fit was used to determine an estimate of c_v in this equation; a value of 1.34 Lpm$\cdot$V$^{-1}\cdot$bar$^{-1/2}$ was identified, whereas 1.07 Lpm$\cdot$V$^{-1}\cdot$bar$^{-1/2}$ was calculated from the datasheet. Expressing the

model of the flow gain over a range of pressures is convenient for allowing the selection of different system supply pressures. The supply pressure of our system averaged 7.6 bar (110 psi), hence the flow gain at this pressure was used throughout.

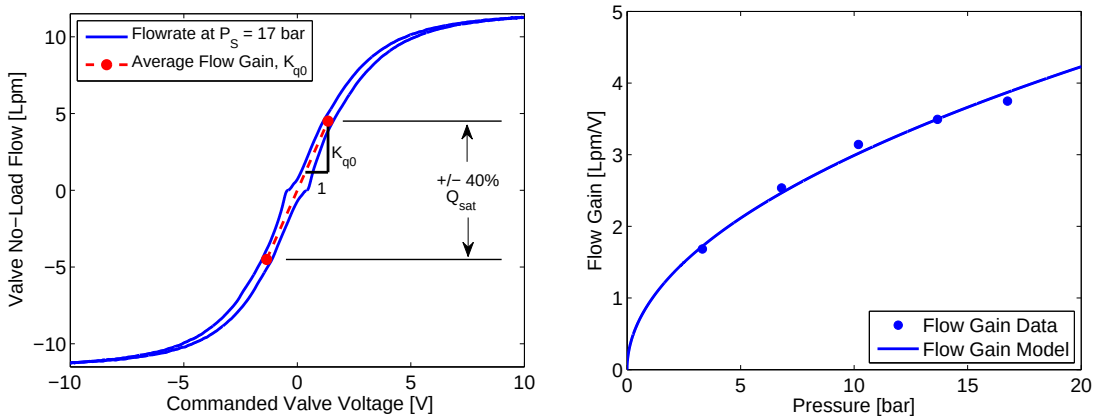

(a) (b)

Figure 3.7: (a) Experimentally determined average null flow gain at 17 bar (250 psi), and (b) null flow gain as a function of pressure and associated model.

3.5 Angular position tracking experiments for developed controllers

In order to evaluate the performance of the developed controllers, a series of experiments was conducted on the robot arm. First, we consider the angular position tracking abilities following a sinusoidal reference trajectory. Then, we do this over a range of frequencies from 1/8 to 1 Hz in 1/8 Hz increments to obtain a frequency response. Lastly, a smooth approximation of a step response test is conducted.

3.5.1 Sinusoidal angular position tracking

In observing the sinusoidal angular position tracking of each controller in detail, we consider 1/4 Hz as the lower frequency and 1 Hz as the higher frequency tested in our range of interest. Experiments at these two frequencies with a 10 degree peak-to-peak amplitude are shown for each of the developed controllers. In addition to the reference and measured angles, the instantaneous error is plotted.

Beginning with the baseline of comparison, the PI-controller tracking of the 1/4 Hz sine wave is shown in Figure 3.8 (a), and its tracking of the 1 Hz sine wave is shown in Figure 3.8 (b). At 1/4 Hz, the peak-to-peak tracking is reasonable, however there is a significant phase lag of approximately 67 degrees, resulting in the large instantaneous error. At 1 Hz, the attenuation is so severe that it is only reaching about 28% of the reference amplitude, and the phase lag is even worse than in Figure 3.8 (a).

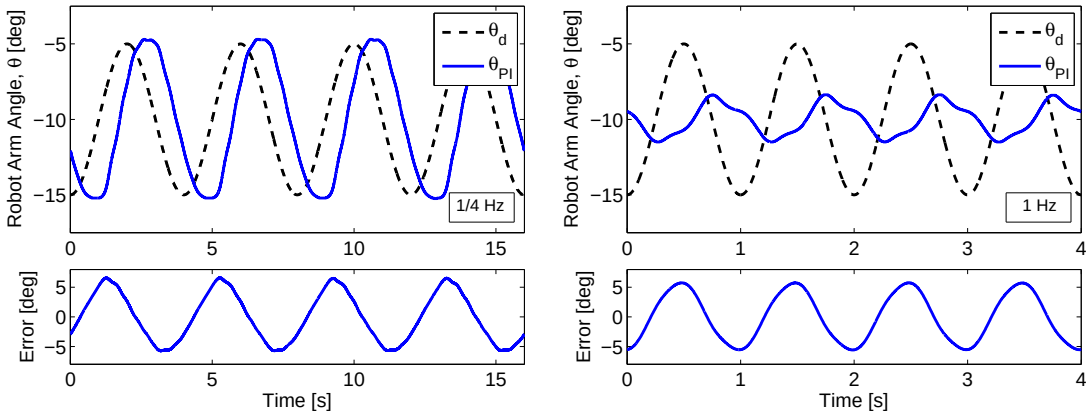

Figure 3.8: Sinusoidal angular position tracking for PI-control at (a) 1/4 Hz, and (b) 1 Hz.

Next, the same two tracking tasks were tested using the feedforward term

added to the PI-controller as shown in Figure 3.4. In Figure 3.9 (a), it is clear that the 1/4 Hz sine wave tracking reaches the desired 10 degree peak-to-peak amplitude, like with the PI-controller in Figure 3.8 (a), however the phase lag has been entirely removed. At 1 Hz, the tracking shown in Figure 3.9 (b) is drastically improved over Figure 3.8 (b) as both the attenuation and phase lag have been almost completely eliminated. There is a slight lag, especially at the bottom of the trajectory, but overall the shape of the reference is mostly preserved in the response.

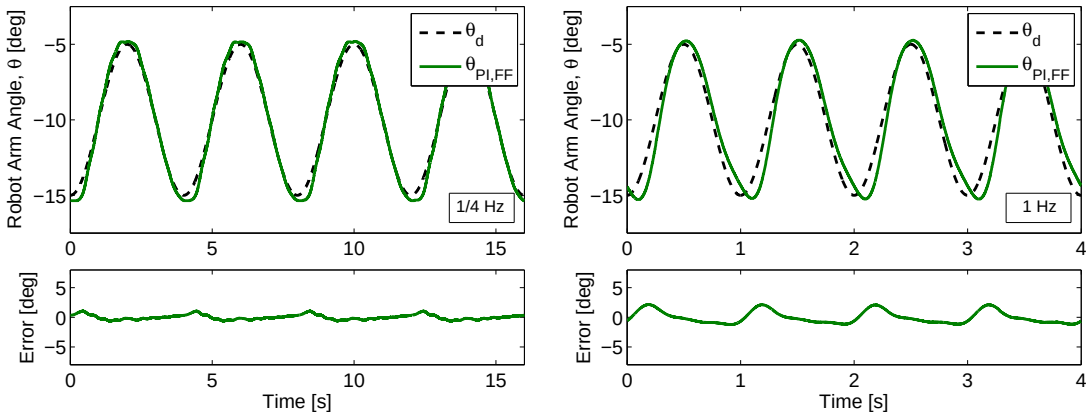

Figure 3.9: Sinusoidal angular position tracking for PI-control with a model-based feedforward term at (a) 1/4 Hz, and (b) 1 Hz.

Testing the last developed controller, with the addition of the inner pressure feedback loop to the second architecture as shown in Figure 3.5, the same tracking tasks were once again performed. This is shown in Figure 3.10, and tracking in both (a) and (b) is quite similar to that seen in Figure 3.9 (a) and (b). The main difference being that the shape of the reference trajectory appears to be slightly better preserved with a little less overshoot. Therefore the addition of the cascaded architecture seems to have minimally changed the tracking of Figure 3.9, but is significantly better than Figure 3.8. The benefits of the this nested

pressure loop will become more clear in Chapter 3.5.3.

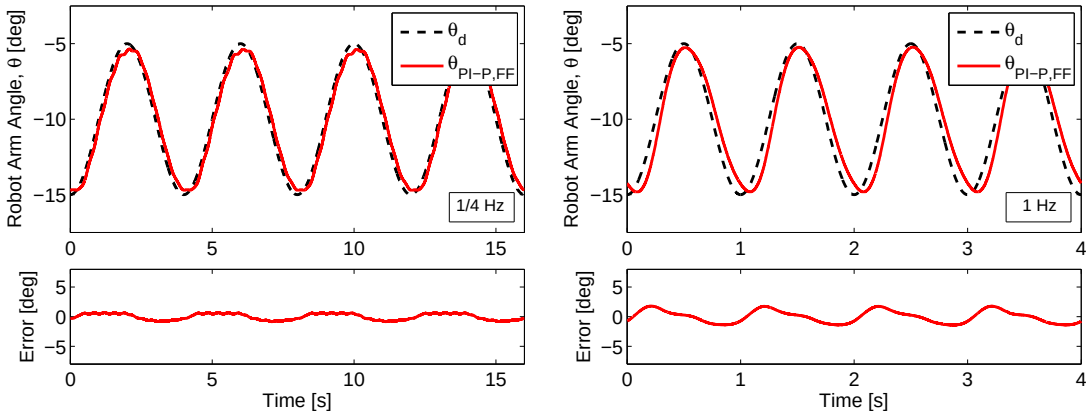

Figure 3.10: Sinusoidal angular position tracking for cascaded PI-P-control with a model-based feedforward term at (a) 1/4 Hz, and (b) 1 Hz.

3.5.2 Frequency response

For the frequency response experiments, the previous tests in Chapter 3.5.1 were repeated to span the frequency range from 1/8 Hz to 1 Hz in 1/8 Hz increments. To quantify the performance differences between the three control architectures, a Bode plot and root mean square (RMS) error plot are included in Figure 3.11 (a) and (b) respectively.

It is clear in the Bode magnitude plot that solely PI-control is insufficient since the −3 dB bandwidth occurs at about 3/8 Hz. Additionally, there is significant overshoot at 1/8 Hz, and as frequency is increased, the attenuation quickly becomes unacceptable (up to −11 dB at 1 Hz). The phase lag is quite large over the full frequency range tested as well. Both the PI-control with feedforward and cascaded PI-P control with feedforward show similar improved Bode char-

acteristics, with the exception that the former shows slightly more overshoot in the mid-range of frequencies tested, and the latter remains slightly closer to 0 dB throughout. Similar results are seen in the RMS error plot, where the PI-controller quickly jumps to over 4 degrees of error, while both the PI-control with feedforward and cascaded PI-P-control with feedforward stay below 1 degree of error for the majority of frequencies tested.

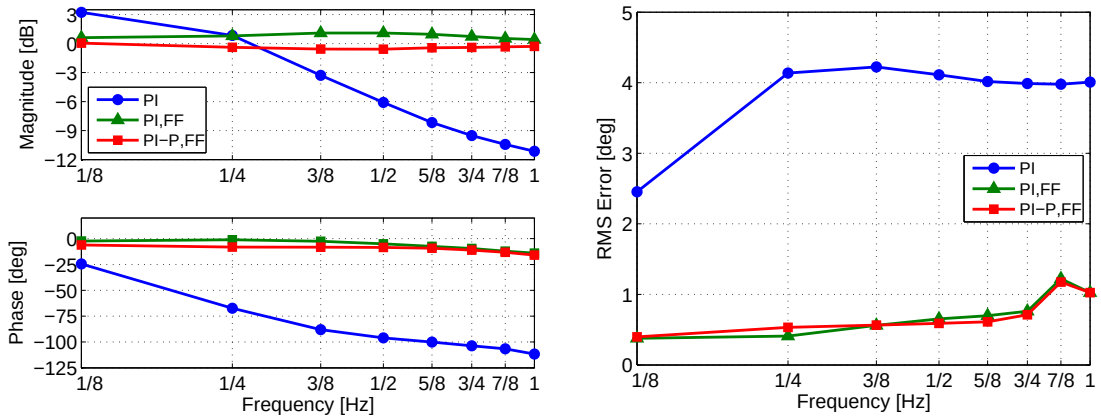

Figure 3.11: (a) Bode plot, and (b) RMS error plot of all controllers tested tracking a 10 degree peak-to-peak amplitude reference.

3.5.3 Step response

The last test used to evaluate the different controllers was a step response. Since a true step function would demand infinite flowrate from the feedforward term, a 'smooth' step approximation was used. Sohl *et al.* utilized a 7th order polynomial step approximation [72], and Weisstein presented various ways including exponentials or a hyperbolic tangent function [87]. We chose to employ a hyperbolic tangent approximation of a 10 degree step with a 10 to 90% rise time of 0.088 s. This represents a rapid command, but does not saturate the valve com-

mand signal (although it is in the highly nonlinear region); this approximation is given by

$$\theta_d(t) = \frac{1}{2}\left[10 \cdot \tanh\left(\frac{t-5}{0.04} - 10\right)\right]. \tag{3.9}$$

Using Equation (3.9) as the reference, the smooth step response of the three controllers is shown in Figure 3.12 (a). Visually comparing these, the PI-controller, in the top portion of this plot, has the slowest response in terms of both rise and settling times, and has the most overshoot. This makes sense since it has the lowest commanded valve voltage initially, seen in Figure 3.12 (b). The PI-controller with feedforward compensation, whose response is given in the middle of Figure 3.12 (a), has a faster rise time due to the anticipative action of the feedforward term, noted by the large spike in control effort initially in Figure 3.12 (b), but has a similar settling time. The overshoot is also smaller, due to the integrator not winding up as much because the feedforward term reduces the initial error. Lastly, the cascaded PI-P-controller with feedforward is presented in the bottom of this figure. This controller clearly has the fastest rise time and settling time when looking at both Figure 3.12 (a) and (b), but has some additional oscillation near the step event.

3.6 Discussion

While the feedforward implemented in this work provides anticipative action in response to changing command profiles, it has zero robustness in terms of changing loads, different operating conditions (such as temperature), or servo-

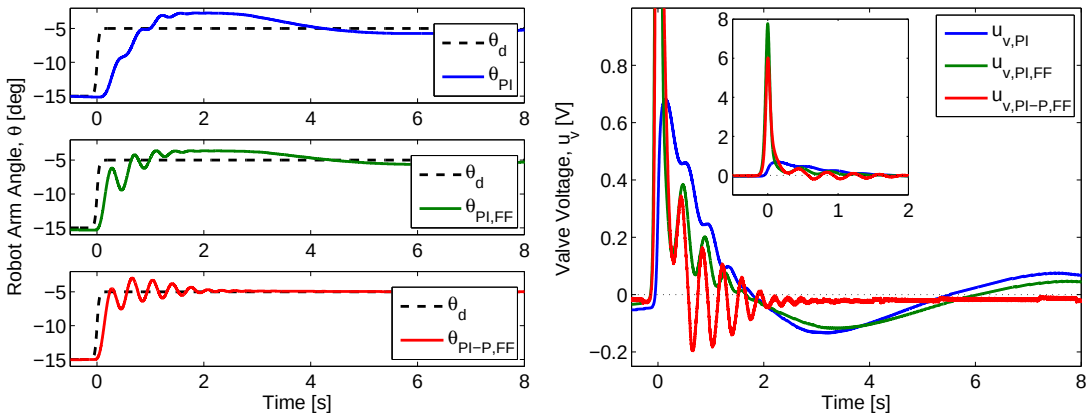

Figure 3.12: (a) Step response of all controllers tested (from top to bottom: PI, PI with feedforward, and cascaded PI-P with feedforward), and (b) associated control inputs.

loop degradation [33]. The feedforward is intended to provide most of the control effort, while the feedback control portion handles the remaining errors and unpredictable system changes.

One concern of using this feedforward term is its inability to manage changing loads. Varying loads correspond to varying pressures, which in turn affects the flowrates out of the valve and degrades tracking. Therefore it was desired to observe the pressure ranges experienced in the most demanding tracking tests above. Even though we considered a fixed load, since we are using McKibben muscles, the pressure must change to achieve different robot arm angles.

The ratio of the measured actuator pressure to the measured supply pressure for the 1 Hz tracking tasks with all controllers tested is given in Figure 3.13 (a). This ratio is presented instead of the raw actuator pressure since it better represents the operating range and proximity to saturation. It is clear that a large pressure range was spanned while the tracking with the feedforward term

was still acceptable. The pressure range experienced was wider than the recommended range by Merritt for control authority purposes [47], showing that the feedforward is still helpful even though the pressure largely deviates from the $\frac{1}{2}P_S$ linearization point.

The commanded valve voltages for all tested controllers during the 1 Hz sinusoidal tracking task are presented in Figure 3.13 (b). The calculated feedforward portion is given as well. The fact that the magnitude of the commanded voltages do not exceed 1.5 V demonstrates that the voltages stayed within the linear region of the valve flow-voltage relationship; hence from this perspective, the null flow gain used is an accurate representation of this relationship. It is also noted how closely the feedforward voltage matches the ultimately commanded valve voltages for the PI with feedforward, and cascaded PI-P with feedforward. This shows that the feedforward term is a good approximation of the demands of the system, and the feedback components are making relatively small contributions to compensate for the small errors mainly due to unmodeled dynamics such as acceleration.

A summary of some key performance metrics comparing the three controllers is presented in Table 3.2. The PI-controller is the simplest and cheapest to implement, but also has the worst dynamic performance of the controllers tested. With the addition of the model-based feedforward term, the tracking performance was significantly improved. It is important to note that this controller has the same disturbance rejection as the PI-only controller. The last control scheme, which added the nested pressure feedback loop within the second architecture, showed overall the best dynamic performance due to improved settling time, however this controller has the most gains to tune and requires an

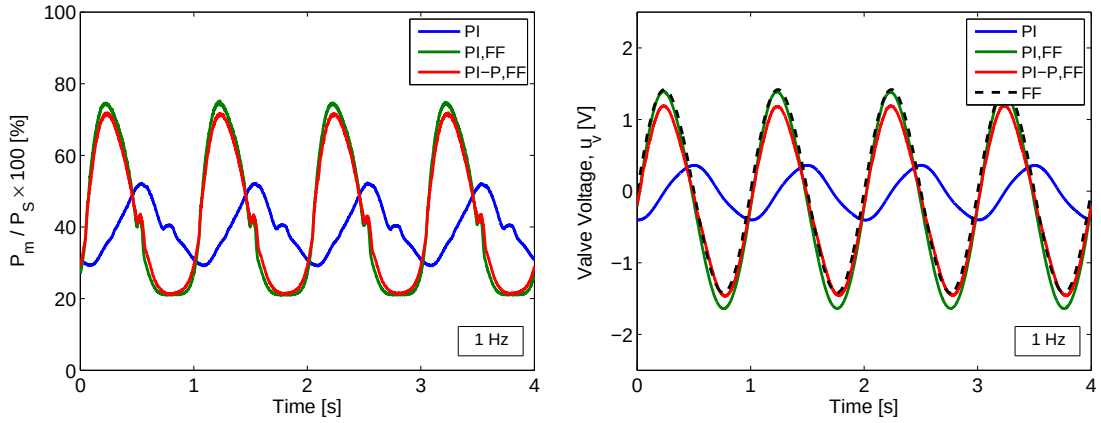

(a) (b)

Figure 3.13: (a) The ratio of actuator pressure to supply pressure, and (b) the commanded valve voltages of all controllers tested at 1 Hz.

additional sensor (pressure transducer).

Table 3.2: Comparison of controllers tested.

	PI	PI,FF	PI-P,FF
Rise Time (0→100%) [s]	0.88	0.61	0.27
Delay Time [s]	0.26	0.13	0.16
Settling Time (5%) [s]	7.52	7.38	1.81
Max Overshoot [%]	22.8	13.8	20.3
−3 dB Bandwidth	3/8 Hz	> 1 Hz	> 1 Hz
Phase Lag	poor	good	good
Disturbance Rejection	fair	fair	good
No. of Gains to Tune	2	3	4
No. of Sensors	1	1	2

3.7 Conclusions

This study experimentally investigated the control of HAMs, demonstrating that hydraulic actuation and control of McKibben muscles at pressures much lower than what is used in traditional hydraulics is feasible. We first showed that using solely PI-control results in poor tracking, marked by a large phase lag at low frequencies and severe attenuation at higher frequencies. Next, we added to the PI-controller a model-based feedforward term that takes into account the predicted nonlinear volumetric flowrate demands of the hydraulic McKibben muscles, as well as the linearized flow gain of the electrohydraulic servovalve; the phase lag and attenuation exhibited by the PI-controller were almost completely eliminated over the frequency range tested. Lastly, an inner pressure feedback loop was included in the previous scheme to create a cascaded PI-P-controller with the feedforward term; this architecture decreased the rise and settling times in addition to allowing for improved disturbance rejection.

These augmentations of classical control techniques were satisfactory for our tracking purposes. Extensions of this work to further enhance performance could pursue several approaches. If performance is limited by system force capability, including an antagonistic pair, additional McKibben muscles, or increasing operating pressure will yield faster response times. If an asymmetric load is experienced, the valve flow gain in the feedforward branch could be split into two values: one for raising the arm, and one for lowering. Improved tracking is also possible with the addition of an acceleration feedforward, which is a relatively common next step in hydraulic cylinder control, however it would need to be adjusted for the nonlinear behavior of the McKibben muscles. Further performance improvements may also be possible by taking into account the

pressure dynamics and using feedback linearization with full state feedback.

This chapter originally appeared as:

> Michael Meller, Boris Kogan, Matthew Bryant, and Ephrahim Garcia. Model-based feedforward and cascade control of hydraulic McKibben muscles. *Sensors and Actuators A: Physical*, 2016.
>
> *In review.*

CONCLUSIONS

Chapter 1 experimentally characterized the transduction efficiency of FAMs when converting the fluid input energy to mechanical output work. In order to discover where these actuators perform best, net-work efficiency experiments were performed over a range of pressures, in addition to studying the effects of the muscle's contraction state. To attain the highest efficiencies for a traditional latex bladder FAM, it was determined that higher operating pressures and actuating in a stroke range closer to the blocked force was best. We found that over the pressure range tested, hydraulic operation resulted in over twice the efficiency of the pneumatic case due to its higher bulk modulus. Two new hydraulic fluid resistant bladders were investigated. Viton, an elastomeric tube with the same thickness as the latex bladder, was the first alternative presented. Due to it's higher Shore hardness, Viton had inferior contraction abilities in addition to reduced efficiencies. An LDPE bag served as the second hydraulic fluid compatible bladder alternative, which had to fold and unfold within the mesh as the muscle was activated. This muscle had superior force output, contraction, and efficiency compared to the other two elastomeric bladder muscles, however it also had the largest hysteresis. The LDPE muscle has a maximum efficiency of almost 80% over its full actuation cycle when run hydraulically, compared to 60% when using a latex bladder muscle, and 27% when the latex muscle is run pneumatically.

Chapter 2 first presented the development of a bioinspired variable recruitment hydraulic McKibben muscle bundle. The quasi-static force-stroke behavior was investigated, and a model for each recruitment level was formulated. This model predicted significant efficiency gains with a variable recruitment ac-

tuation scheme. A real-time selective recruitment controller for the developed hydraulic artificial muscle bundle was implemented. This utilized a recruitment logic state machine that selected the current recruitment level based on measured pressures and a pressure threshold schedule. These thresholds were chosen such that high efficiencies would be attained, while retaining sufficient control authority. Additionally, hysteresis was built into the thresholds to prevent rapid switching between recruitment levels. The current recruitment level determined what gains to use in the controller and which servovalves to activate. This live recruitment controller was tested on a single degree-of-freedom robot arm, where efficiency was measured over a range of loading conditions. This data was compared to a single equivalent muscle case where only throttling was used to control the system. As predicted by our model, variable recruitment was shown to significantly improve efficiency in the low load regions. Over the load ranges tested, variable recruitment increased the average efficiency by 46% (difference of 18%) compared to the single equivalent muscle case.

Chapter 3 experimentally investigated improved control of HAMs (without variable recruitment). Using solely PI-control resulted in poor tracking, marked by a large phase lag at low frequencies and severe attenuation at higher frequencies. A model-based feedforward term that takes into account the predicted nonlinear volumetric flowrate demands of the hydraulic McKibben muscles, as well as the linearized flow gain of the electrohydraulic servovalve was added to the PI-controller; the phase lag and attenuation exhibited by PI-control were almost completely eliminated over the frequency range tested. Lastly, an inner pressure feedback loop was included in the previous scheme to create a cascaded PI-P-controller with the feedforward term; this architecture further improved tracking by decreasing the rise and settling times.

In summary, this thesis presents the following novel contributions:

- Chapter 1 Contributions:

  (Reconsidering the McKibben muscle: energetics, operating fluid, and bladder material)

  - The energetic efficiency of McKibben muscles was experimentally characterized over a range of pressures and contraction levels
  - It was demonstrated that actuating McKibben muscles hydraulically rather than pneumatically can result in over double the efficiency
  - Using an LDPE bag bladder allowed the McKibben muscle to contract almost immediately, while more pressure is required to achieve the same strain in elastomeric bladders
  - Modeling the McKibben mesh as a cylinder over its full contraction range was experimentally validated to be extremely accurate
  - Using McKibben muscles hydraulically at higher pressures with an inelastic bladder was shown to yield the best efficiencies: at 75psi, the pneumatic latex bladder McKibben has an efficiency of 27% while a hydraulic LDPE bladder muscle attained 80%

- Chapter 2 Contributions:

  (Improving actuation efficiency through variable recruitment hydraulic McKibben muscles: modeling, orderly recruitment control, and experiments)

  - A proof-of-concept variable recruitment hydraulic McKibben muscle bundle was developed for reducing servovalve throttling losses
  - A volume-based effective initial braid angle was used for a more accurate semi-empirical model of each recruitment level of the bundle

- The developed model was used to predict the efficiency gains of variable recruitment compared to a throttling-only approach
- The effect of the total number of recruitment levels was considered, showing that higher numbers of recruitment levels yield higher efficiencies, however with diminishing returns
- A real-time, hysteretic pressure threshold-based orderly recruitment controller was implemented to minimize the number of active McKibben pairs, hence reducing fluid power consumption
- Over the range of loads tested, variable recruitment yielded an 18% higher (1.46 ×) average efficiency compared to the throttling-only approach, and agreed well with the theoretical predictions

- Chapter 3 Contributions:

  (Model-based feedforward and cascade control of hydraulic McKibben muscles)

  - One of the first hydraulic McKibben controllers was developed
  - Angular position tracking was improved through simple augmentations to classical control techniques
  - A feedforward term comprised of the model-based volumetric flowrate demands of the McKibben muscles in conjunction with the electrohydraulic servovalve flow gain was formulated
  - This feedforward successfully removed the phase lag and attenuation seen with solely PI-control over the frequency range tested
  - A nested pressure feedback loop was added to create a cascaded PI-P-controller (still with feedforward) that yielded faster setting times
  - These improvements lend themselves well to more advanced variable recruitment control techniques

Future directions:

To further improve the effectiveness and efficiency of variable recruitment, several considerations should be made: 1. muscle fiber construction, 2. number and arrangement of motor units, 3. valving, 4. control strategy, and 5. system integration.

1. Since higher pressure operation yields higher efficiency, the construction of the muscles should be modified to allow for this. The LDPE muscle from Chapter 1 works well at low pressures, but consistent use over 100 psi led to bladder rupture. Currently, the silicone bladder McKibben muscles used in Chapters 2 and 3 can only withstand up to 150 psi for extended periods of time (tens of thousands of cycles). The McKibben muscles ideally should be able to withstand high pressures (on the order of 1000-3000 psi) to millions of cycles without impeding contraction. A shift in construction towards a braided sheath embedded in an oil-resistant elastomer (similar to FESTO Fluidic Muscles, but rated for $> 10\times$ the pressure) to help prevent braid separation and bladder rupture could help enable this.
2. The proof-of-concept muscle bundle in Chapter 2 had three levels of recruitment, but it was shown that higher numbers of recruitment levels will yield higher efficiencies. Therefore, future iterations should strive to have more motor units. The current arrangement has opposite pairs of muscle fibers fluidically connected to allow for purely axial tension generation – this method could still be used, but doesn't necessarily require the number of muscle fibers per motor unit to be two. The hexagonal bundling manifold end caps were developed to mechanically attach the muscles in parallel and fluidcally connect the opposite pairs of muscle fibers. More

consideration of how to densely achieve this with more motor units, as well as better handle the buckling of inactive muscle fibers (from a mechanical standpoint of fatigue and potentially getting caught on items in the surrounding environment) is required. Additionally, the muscle fibers used here are identically sized – it may be beneficial to include different sized muscle fibers in the muscle bundle.

3. Once more muscle fibers have been included in the muscle bundle, the next challenge is how to allow the flow of pressurized fluid to the appropriate motor units in a compact manner. The configuration in Chapter 2 uses three total EHSVs – one EHSV to control each opposite pair of McKibben muscle fibers (making up a motor unit). With small numbers of motor units this approach might be acceptable, but with higher numbers, this would prove too bulky and new valving configurations should be considered. If the number of motor units gets high enough, then operation might be able to be performed smoothly in a more binary fashion without large jumps in force output.

4. Chapter 3 presented some simple augmentations to classical control that resulted in far better trajectory tracking for a throttling-only control approach. These techniques could be applied to variable recruitment to help remove the phase lag seen in the tracking in Chapter 2. Additionally, more thought should be given to allow for smooth transitions when shifting up or down between recruitment levels. This could be assisted by enforcing pressure requirements on each motor unit using inner control loops within an outer position control loop. Pre-filling the next inactive motor unit just prior to an upshift in recruitment level could mitigate the lag observed in Chapter 2 when this occurred – which was especially apparent

in high strain upshifts. If even more advanced control is required, then model-predictive and nonlinear control techniques are suggested to better the trajectory tracking during transitions between recruitment levels.

5. The work of Chapter 2 focused on improving hydraulic actuation efficiency through reducing servovalve throttling losses as these are currently the largest inefficiencies system wide. However, once these losses have been decreased through variable recruitment, system integration must be considered to ensure efficient operation remains. The valves and actuators receive pressurized fluid from a pump, which has been treated as an ideal pressure source thus far. A fixed displacement pump would constantly run and bleed off excess fluid power over a relief valve, which is highly inefficient. Therefore a load-sensing variable displacement pump should be used to help match the pressure and flow demands of all the actuators. Since a load-sensing pump can only lower its supply pressure to the highest demanding actuator, a semi-distributed pump layout (the design space between one pump per actuator, and one pump for the whole system) could also prove beneficial. If the overall system efficiency is high enough, then the heat generation may be low enough to eliminate the need for a cooling system. Lastly, in utilizing a variable recruitment actuation scheme, the designer will need to weigh trade-offs between energy efficiency and ensuring sufficient control authority.

BIBLIOGRAPHY

[1] Atlas – the agile anthropomorphic robot. http://www.bostondynamics.com/robot_Atlas.html. Accessed: 2016-02-07.

[2] Chemical compatibility database. http://www.coleparmer.com/Chemical-Resistance. Accessed: 2016-02-07.

[3] Electrohydraulic valves... a technical look. Technical report, Moog, Inc.

[4] HULC. http://www.lockheedmartin.com/us/products/exoskeleton/hulc.html. Accessed: 2016-02-07.

[5] Modeling an automatic transmission controller. http://www.mathworks.com/examples/simulink/mw/simulink_product-sldemo_autotrans-modeling-an-automatic-transmission-controller. Accessed: 2016-02-07.

[6] Raytheon XOS 2 exoskeleton, second-generation robotics suit, united states of america. http://www.army-technology.com/projects/raytheon-xos-2-exoskeleton-us/. Accessed: 2016-02-07.

[7] Erick Ball, Yong Lin, and Ephrahim Garcia. Characterization and modeling of geometric variations in McKibben pneumatic artificial muscles. In *SPIE Smart Structures and Materials+ Nondestructive Evaluation and Health Monitoring*, pages 868605–868605. International Society for Optics and Photonics, 2013.

[8] Erick J Ball, Michael A Meller, Jordan B Chipka, and Ephrahim Garcia. Modeling and testing of a knitted-sleeve fluidic artificial muscle. *Smart Materials and Structures*, 25(11):115024, 2016.

[9] John Francis Blackburn, Gerhard Reethof, and J Lowen Shearer. *Fluid Power Control*. The Technology Press of M.I.T., 1960.

[10] Matthew Bryant, Michael A Meller, and Ephrahim Garcia. Variable recruitment fluidic artificial muscles: modeling and experiments. *Smart Materials and Structures*, 23(7):074009, 2014.

[11] Edward A Bubert. *Highly extensible skin for a variable wing-span morphing aircraft utilizing pneumatic artificial muscle actuation*. ProQuest, 2009.

[12] Dieter Büchler, Heiko Ott, and Jan Peters. A lightweight robotic arm with pneumatic muscles for robot learning. In *2016 IEEE International Conference on Robotics and Automation (ICRA)*, pages 4086–4092. IEEE, 2016.

[13] Darwin G Caldwell, Gustavo A Medrano-Cerda, and Colin J Bowler. Investigation of bipedal robot locomotion using pneumatic muscle actuators. In *Robotics and Automation, 1997. Proceedings., 1997 IEEE International Conference on*, volume 1, pages 799–804. IEEE, 1997.

[14] Darwin G Caldwell, Gustavo A Medrano-Cerda, and Mike Goodwin. Control of pneumatic muscle actuators. *IEEE control systems*, 15(1):40–48, 1995.

[15] Ching-Ping Chou and Blake Hannaford. Measurement and modeling of McKibben pneumatic artificial muscles. *Robotics and Automation, IEEE Transactions on*, 12(1):90–102, 1996.

[16] Robb W Colbrunn, Gabriel M Nelson, and Roger D Quinn. Design and control of a robotic leg with braided pneumatic actuators. In *Intelligent Robots and Systems, 2001. Proceedings. 2001 IEEE/RSJ International Conference on*, volume 2, pages 992–998. IEEE, 2001.

[17] Robb W Colbrunn, Gabriel M Nelson, and Roger D Quinn. Modeling of braided pneumatic actuators for robotic control. In *Intelligent Robots and Systems, 2001. Proceedings. 2001 IEEE/RSJ International Conference on*, volume 4, pages 1964–1970. IEEE, 2001.

[18] Steve Collins, Andy Ruina, Russ Tedrake, and Martijn Wisse. Efficient bipedal robots based on passive-dynamic walkers. *Science*, 307(5712):1082–1085, 2005.

[19] Eric Cousineau and Aaron D Ames. Realizing underactuated bipedal walking with torque controllers via the ideal model resolved motion method. In *Robotics and Automation (ICRA), 2015 IEEE International Conference on*, pages 5747–5753. IEEE, 2015.

[20] Michaël De Volder, AJM Moers, and Dominiek Reynaerts. Fabrication and control of miniature McKibben actuators. *Sensors and Actuators A: Physical*, 166(1):111–116, 2011.

[21] DARPA Defense Sciences Office (DSO). Broad agency announcement: Maximum mobility and manipulation (M3), actuation. pages DARPA–BAA–12–52, 2012.

[22] Sylvie A DeLaHunt, Thomas E Pillsbury, and Norman M Wereley. Variable recruitment in bundles of miniature pneumatic artificial muscles. *Bioinspiration & Biomimetics*, 11(5):056014, 2016.

[23] Dupont. Viton fluoroelastomer. `http://www.dupont.com/products-and-services/plastics-polymers-resins/elastomers/`. Accessed: 2014-04-02.

[24] Björn Eriksson. Control strategy for energy efficient fluid power actuators: Utilizing individual metering. 2007.

[25] Daniel P Ferris, Joseph M Czerniecki, Blake Hannaford, and University of Washington. An ankle-foot orthosis powered by artificial pneumatic muscles. *Journal of applied biomechanics*, 21(2):189, 2005.

[26] FESTO. Airic's arm: Robot arm with fluidic muscles. `https://www.festo.com/net/SupportPortal/Files/42058/Airics_arm_en.pdf`. Accessed: 2016-09-07.

[27] Michele Focchi, Emanuele Guglielmino, Claudio Semini, Alberto Parmiggiani, Nikos Tsagarakis, Bram Vanderborght, and Darwin G Caldwell. Water/air performance analysis of a fluidic muscle. In *Intelligent Robots and Systems (IROS), 2010 IEEE/RSJ International Conference on*, pages 2194–2199. IEEE, 2010.

[28] Michael F Gentry and Norman M Wereley. Effects of braid angle on pneumatic artificial muscle actuator performance. In *ASME 2008 Conference on Smart Materials, Adaptive Structures and Intelligent Systems*, pages 617–623. American Society of Mechanical Engineers, 2008.

[29] Elwood Henneman, George Somjen, and David O Carpenter. Functional significance of cell size in spinal motoneurons. *Journal of neurophysiology*, 28(3):560–580, 1965.

[30] A Hildebrandt, O Sawodny, R Neumann, and A Hartmann. Cascaded control concept of a robot with two degrees of freedom driven by four artificial pneumatic muscle actuators. In *Proceedings of the 2005, American Control Conference, 2005.*, pages 680–685. IEEE, 2005.

[31] Erica G Hocking and Norman M Wereley. Analysis of nonlinear elastic behavior in miniature pneumatic artificial muscles. *Smart Materials and Structures*, 22(1):014016, 2012.

[32] JE Huber, NA Fleck, and MF Ashby. The selection of mechanical actuators based on performance indices. In *Proceedings of the Royal Society of London A: Mathematical, Physical and Engineering Sciences*, volume 453, pages 2185–2205. The Royal Society, 1997.

[33] Jack L Johnson. *Designer's handbook for electrohydraulic servo and proportional systems*. IDAS Engineering, 2000.

[34] Bong-Soo Kang, Curt S Kothera, Benjamin KS Woods, and Norman M Wereley. Dynamic modeling of Mckibben pneumatic artificial muscles for antagonistic actuation. In *Robotics and Automation, 2009. ICRA'09. IEEE International Conference on*, pages 182–187. IEEE, 2009.

[35] George Karpati, David Hilton-Jones, and Robert C Griggs. *Disorders of voluntary muscle*. Cambridge University Press, 2001.

[36] Glenn K Klute and Blake Hannaford. Accounting for elastic energy storage in McKibben artificial muscle actuators. *Journal of dynamic systems, measurement, and control*, 122(2):386–388, 2000.

[37] Curt S Kothera, Mamta Jangid, Jayant Sirohi, and Norman M Wereley. Experimental characterization and static modeling of McKibben actuators. *Journal of Mechanical Design*, 131(9):091010, 2009.

[38] Manish Kulkarni, Taehyun Shim, and Yi Zhang. Shift dynamics and control of dual-clutch transmissions. *Mechanism and Machine Theory*, 42(2):168–182, 2007.

[39] Arthur D Kuo. Choosing your steps carefully. *IEEE Robotics & Automation Magazine*, 14(2):18–29, 2007.

[40] John H Lilly and Peter M Quesada. A two-input sliding-mode controller for a planar arm actuated by four pneumatic muscle groups. *Neural Systems and Rehabilitation Engineering, IEEE Transactions on*, 12(3):349–359, 2004.

[41] Lonnie J Love, Eric Lanke, and Pete Alles. Estimating the impact (energy, emissions and economics) of the U.S. fluid power industry. Technical report, Oak Ridge National Laboratory, 12 2012.

[42] Noah Manring. *Hydraulic control systems*. John Wiley & Sons Incorporated, 2005.

[43] Thomas E Marlin. *Process control*. McGraw-Hill New York, 2000.

[44] Michael Meller, Jordan Chipka, Alexander Volkov, Matthew Bryant, and Ephrahim Garcia. Improving actuation efficiency through variable recruitment hydraulic McKibben muscles: modeling, orderly recruitment control, and experiments. *Bioinspiration & Biomimetics*, 11(6):065004, 2016.

[45] Michael A Meller, Matthew Bryant, and Ephrahim Garcia. Reconsidering the McKibben muscle: energetics, operating fluid, and bladder material. *Journal of Intelligent Material Systems and Structures*, 25(18):2276–2293, 2014.

[46] Michael A Meller, Matthew J Bryant, and Ephrahim Garcia. Energetic and dynamic effects of operating fluid on fluidic artificial muscle actuators. In *ASME 2013 Conference on Smart Materials, Adaptive Structures and Intelligent Systems*, pages V002T06A019–V002T06A019. American Society of Mechanical Engineers, 2013.

[47] Herbert E Merritt. *Hydraulic Control Systems*. John Wiley & Sons, Inc., 1967.

[48] Tri Vo Minh, Tegoeh Tjahjowidodo, Herman Ramon, and Hendrik Van Brussel. Cascade position control of a single pneumatic artificial muscle–mass system with hysteresis compensation. *Mechatronics*, 20(3):402–414, 2010.

[49] Moog. Moog G761/761 series flow control servo valves. `http://www.moog.com/literature/ICD/Moog-ServoValves-G761_761Series-Catalog-en.pdf`, 2014. Accessed: 2016-02-02.

[50] Jason K Moore, Sandra K Hnat, and Antonie J van den Bogert. An elaborate data set on human gait and the effect of mechanical perturbations. *PeerJ*, 3:e918, 2015.

[51] Mayuko Mori, Koichi Suzumori, Masayuki Takahashi, and Takashi Hosoya. Very high force hydraulic McKibben artificial muscle with a p-phenylene-2, 6-benzobisoxazole cord sleeve. *Advanced Robotics*, 24(1-2):233–254, 2010.

[52] Peter E Nachtwey. *Practical design for fluid power motion control*. Delta Computer Systems, Inc., Battle Groung, WA, 2013.

[53] Gabe Nelson, Aaron Saunders, Neil Neville, Ben Swilling, Joe Bondaryk, Devin Billings, Chris Lee, Robert Playter, and Marc Raibert. Petman: A humanoid robot for testing chemical protective clothing. *Journal of the Robotics Society of Japan*, 30(4):372–377, 2012.

[54] Ryuma Niiyama, Akihiko Nagakubo, and Yasuo Kuniyoshi. Mowgli: A bipedal jumping and landing robot with an artificial musculoskeletal system. In *Robotics and Automation, 2007 IEEE International Conference on*, pages 2546–2551. IEEE, 2007.

[55] Munetaka Noda, Yukio Tobe, Yutaka Taga, Shinya Nakamura, Kazumasa Nakamura, Takafumi Inagaki, and Hiroshi Ito. Automatic transmission controller for automobiles, June 11 1985. US Patent 4,523,281.

[56] Yong-Lae Park, Bor-rong Chen, Diana Young, Leia Stirling, Robert J Wood, Eugene C Goldfield, Radhika Nagpal, et al. Design and control of a bio-inspired soft wearable robotic device for ankle-foot rehabilitation. *Bioinspiration & Biomimetics*, 9(1):016007, 2014.

[57] Larry D Peel, James Mejia, Ben Narvaez, Kyle Thompson, and Madhuri Lingala. Development of a simple morphing wing using elastomeric composites as skins and actuators. *Journal of Mechanical Design*, 131(9):091003, 2009.

[58] Thomas E Pillsbury, Curt S Kothera, and Norman M Wereley. Effect of bladder wall thickness on miniature pneumatic artificial muscle performance. *Bioinspiration & Biomimetics*, 10(5):055006, 2015.

[59] Marc Raibert, Kevin Blankespoor, Gabriel Nelson, Rob Playter, and TB Team. BigDog, the rough-terrain quadruped robot. In *Proceedings of the 17th World Congress*, volume 17, pages 10822–10825, 2008.

[60] Alireza Ramezani, Jonathan W Hurst, Kaveh Akbari Hamed, and JW Grizzle. Performance analysis and feedback control of ATRIAS, a three-dimensional bipedal robot. *Journal of Dynamic Systems, Measurement, and Control*, 136(2):021012, 2014.

[61] Jacob Reher, Eric A Cousineau, Ayonga Hereid, Christian M Hubicki, and Aaron D Ames. Realizing dynamic and efficient bipedal locomotion on

the humanoid robot DURUS. In *Robotics and Automation (ICRA), 2016 IEEE International Conference on*, pages 1794–1801. IEEE, 2016.

[62] Ryan M Robinson, Curt S Kothera, and Norman M Wereley. Variable recruitment testing of pneumatic artificial muscles for robotic manipulators. *IEEE/ASME Transactions on Mechatronics*, 20(4):1642–1652, 2015.

[63] Wilson J Rugh and Jeff S Shamma. Research on gain scheduling. *Automatica*, 36(10):1401–1425, 2000.

[64] Naoki Saito, Takanori Sato, Takanori Ogasawara, Ryo Takahashi, and Toshiyuki Sato. Mechanical equilibrium model of rubberless artificial muscle and application to position control of antagonistic drive system. *Industrial Robot: An International Journal*, 40(4):347–354, 2013.

[65] Danial Sangian, Sina Naficy, and Geoffrey M Spinks. Thermally activated paraffin-filled McKibben muscles. *Journal of Intelligent Material Systems and Structures*, page 1045389X16633766, 2016.

[66] Danial Sangian, Sina Naficy, Geoffrey M Spinks, and Bertrand Tondu. The effect of geometry and material properties on the performance of a small hydraulic McKibben muscle system. *Sensors and Actuators A: Physical*, 234:150–157, 2015.

[67] Joachim Schröder, Duygun Erol, Kazuhiko Kawamura, and Riidiger Dillman. Dynamic pneumatic actuator model for a model-based torque controller. In *Computational Intelligence in Robotics and Automation, 2003. Proceedings. 2003 IEEE International Symposium on*, volume 1, pages 342–347. IEEE, 2003.

[68] Claudio Semini, Nikos G Tsagarakis, Emanuele Guglielmino, Michele Focchi, Ferdinando Cannella, and Darwin G Caldwell. Design of HyQ – a hydraulically and electrically actuated quadruped robot. *Proceedings of the Institution of Mechanical Engineers, Part I: Journal of Systems and Control Engineering*, page 0959651811402275, 2011.

[69] Shadow Robot Company. The Shadow Biped. `http://www.shadow.org.uk/projects/biped.shtml`. Accessed: 2016-09-07.

[70] SC Skinner and RJ Long. *Closed loop electrohydraulic systems manual*. Rochester Hills, MI: Vickers Incorporated Training Center, 1998.

[71] Jean-Jacques E Slotine, Weiping Li, et al. *Applied nonlinear control*, volume 199. prentice-Hall Englewood Cliffs, NJ, 1991.

[72] Garett A Sohl and James E Bobrow. Experiments and simulations on the nonlinear control of a hydraulic servosystem. *IEEE transactions on control systems technology*, 7(2):238–247, 1999.

[73] Belen Solano and Christine Rotinat-Libersa. Compact and lightweight hydraulic actuation system for high performance millimeter scale robotic applications: Modeling and experiments. *Journal of Intelligent Material Systems and Structures*, page 1045389X11418860, 2011.

[74] Benjamin J Stephens and Christopher G Atkeson. Push recovery by stepping for humanoid robots with force controlled joints. In *Humanoid Robots (Humanoids), 2010 10th IEEE-RAS International Conference on*, pages 52–59. IEEE, 2010.

[75] Kazuto Takashima, Jonathan Rossiter, and Toshiharu Mukai. McKibben

artificial muscle using shape-memory polymer. *Sensors and Actuators A: Physical*, 164(1):116–124, 2010.

[76] Takashi Takuma and Koh Hosoda. Controlling the walking period of a pneumatic muscle walker. *The International Journal of Robotics Research*, 25(9):861–866, 2006.

[77] Rashi Tiwari, Michael A Meller, Karl B Wajcs, Caris Moses, Ismael Reveles, and Ephrahim Garcia. Hydraulic artificial muscles. *Journal of Intelligent Material Systems and Structures*, 23(3):301–312, 2012.

[78] Bertrand Tondu. Modelling of the McKibben artificial muscle: A review. *Journal of Intelligent Material Systems and Structures*, 23(3):225–253, 2012.

[79] Bertrand Tondu, Serge Ippolito, Jérémie Guiochet, and A Daidie. A seven-degrees-of-freedom robot-arm driven by pneumatic artificial muscles for humanoid robots. *The International Journal of Robotics Research*, 24(4):257–274, 2005.

[80] Bertrand Tondu and Pierre Lopez. Modeling and control of McKibben artificial muscle robot actuators. *IEEE control systems*, 20(2):15–38, 2000.

[81] N Tsagarakis and Darwin G Caldwell. Improved modelling and assessment of pneumatic muscle actuators. In *Robotics and Automation, 2000. Proceedings. ICRA'00. IEEE International Conference on*, volume 4, pages 3641–3646. IEEE, 2000.

[82] N Tsagarakis, DG Caldwell, and GA Medrano-Cerda. A 7 DOF pneumatic muscle actuator (pMA) powered exoskeleton. In *Robot and Human Interaction, 1999. RO-MAN'99. 8th IEEE International Workshop on*, pages 327–333. IEEE, 1999.

[83] Bjorn D Tyreus and William L Luyben. Tuning PI controllers for integrator/dead time processes. *Industrial & Engineering Chemistry Research*, 31(11):2625–2628, 1992.

[84] U.S Plastic Corporation. Tubing, hose & fittings. `http://www.usplastic.com/catalog/default.aspx?catid=856&;clickid=popcorn`. Accessed: 2014-07-01.

[85] Björn Verrelst, Ronald Van Ham, Bram Vanderborght, Frank Daerden, Dirk Lefeber, and Jimmy Vermeulen. The pneumatic biped Lucy actuated with pleated pneumatic artificial muscles. *Autonomous Robots*, 18(2):201–213, 2005.

[86] Tri Vo-Minh, Tegoeh Tjahjowidodo, Herman Ramon, and Hendrik Van Brussel. A new approach to modeling hysteresis in a pneumatic artificial muscle using the Maxwell-slip model. *IEEE/ASME Transactions on Mechatronics*, 16(1):177–186, 2011.

[87] Eric W Weisstein. Heaviside step function, from MathWorld–a Wolfram web resource. `http://mathworld.wolfram.com/HeavisideStepFunction.html`. Accessed: 2016-09-07.

[88] David A Winter. *Biomechanics and motor control of human movement*. John Wiley & Sons, 2009.

[89] Benjamin KS Woods, Young-Tai Choi, Curt S Kothera, and Norman M Wereley. Control system development for pneumatic artificial muscle-driven active rotor systems. *Journal of Guidance, Control, and Dynamics*, 36(4):1177–1185, 2013.

[90] Benjamin KS Woods, Curt Kothera, and Norman M Wereley. Fluidic artificial muscle actuator and swaging process therefor, November 13 2012. US Patent 8,307,753.

[91] Benjamin KS Woods, Curt S Kothera, and Norman M Wereley. Wind tunnel testing of a helicopter rotor trailing edge flap actuated via pneumatic artificial muscles. *Journal of Intelligent Material Systems and Structures*, 22(13):1513–1528, 2011.

[92] Chaoqun Xiang, Maria Elena Giannaccini, Theo Theodoridis, Lina Hao, Samia Nefti-Meziani, and Steven Davis. Variable stiffness McKibben muscles with hydraulic and pneumatic operating modes. *Advanced Robotics*, 30(13):889–899, 2016.

[93] T-J Yeh, Meng-Je Wu, Ting-Jiang Lu, Feng-Kuang Wu, and Chih-Ren Huang. Control of McKibben pneumatic muscles for a power-assist, lower-limb orthosis. *Mechatronics*, 20(6):686–697, 2010.